8-2009

Studies on a Polarized Proton Target for Reactions with Radioactive Ion Beams

Juan Pablo Urrego-Blanco
University of Tennessee - Knoxville

To the Graduate Council:

I am submitting herewith a dissertation written by Juan Pablo Urrego-Blanco entitled "Studies on a Polarized Proton Target for Reactions with Radioactive Ion Beams." I have examined the final electronic copy of this dissertation for form and content and recommend that it be accepted in partial fulfillment of the requirements for the degree of Doctor of Philosophy, with a major in Physics.

Carroll R. Bingham, Major Professor

We have read this dissertation and recommend its acceptance:

Alfredo Galindo-Uribarri, Yuri Efremenko, Witold Nazarewicz, Lawrence W. Townsend

Accepted for the Council:

Carolyn R. Hodges

Vice Provost and Dean of the Graduate School

(Original signatures are on file with official student records.)

To the Graduate Council:
I am submitting herewith a dissertation written by Juan Pablo Urrego-Blanco entitled "Studies on a Polarized Proton Target for Reactions with Radioactive Ion Beams." I have examined the final electronic copy of this dissertation for form and content and recommend that it be accepted in partial fulfillment of the requirements for the degree of Doctor of Philosophy, with a major in Physics.

Carrol R. Bingham
Major Professor

We have read this dissertation
and recommend its acceptance:

Alfredo Galindo-Uribarri

Yuri Efremenko

Witold Nazarewicz

Lawrence W. Townsend

Accepted for the Council:

Carolyn R. Hodges
Vice Provost and Dean of the Graduate School

(Original signatures are on file with official student records)

Studies on a Polarized Proton Target for Reactions with Radioactive Ion Beams

A Dissertation
Presented for the
Doctor of Philosophy Degree
The University of Tennessee, Knoxville

Juan Pablo Urrego Blanco
August 2009

A mis Padres,
a Rolando y Diana,
y a Pilar, por supuesto.

Acknowledgements

It is often said that it takes a village to raise a PhD. In my case, that is certainly true. The number of people involved in one way or another with this project is so large that I could not mention everybody here. It is an honor and a pleasure to express my deepest gratitude to all them. However, for the sake of brevity, I will mention here only the people who were involved in a very direct way.

I am indebted to Dr. Alfredo Galindo-Uribarri for his close guidance and help throughout these years of graduate school. His passion for Physics and his commitment to the education and well being of his students are an inspiration. His teachings extend far beyond Nuclear Physics and will always accompany me.

I am grateful to Professor Carrol Bingham for his continuous support and encouragement. I also acknowledge his help in the analysis of the cross section excitation functions measured at the Holifield Radioactive Ion Beam Facility (HRIBF) in Oak Ridge. I also want to thank the members of my PhD committee for their concern about the development of the project and the valuable comments to this dissertation.

The success of this project largely rests upon the contributions and expertise from the Low Temperature Group from the Paul Scherrer Institute (PSI) led by Dr. Ben van den Brandt. Ben and his colleagues Patrick Hautle, and Ton Konter spent many hours training me in the subtleties of low temperature physics and dynamic nuclear polarization. The time spent at PSI with the Group at PSI will remain as one of the richest educational, professional, and personal experiences of my life.

I am very thankful to Mr. Paul Schurter, Willi Arrigoni, and Michael Schmutz for their numerous technical contributions to this project, the good times spent in the workshop, and their patience for coping with my poor German. My respect and admiration goes to these gentlemen who demonstrate with their fine work that Swiss precision is no cliché.

The in-beam tests of the polarized target were performed with the Phillips Cyclotron at PSI thanks to the willingness and diligent work of Dr. Pierre Schmelzbach and Peter Meyer. Many thanks for that.

My sincere thanks to Dr. Elizabeth Padilla-Rodal, who played a critical role during the in-beam tests at PSI and HRIBF. She was always there when she was needed, either to discuss Physics, to help in all sort of technical matters, or simply to cheer me in the difficult moments.

I am also indebted to Drs. Kamil Sedlak and Toni Shiroka, from the μSR group at PSI, for providing me with the basic GEANT4 routines to simulate the trajectories of charged particles in the magnetic field of the polarized target.

The preparation and characterization of thin target foils was possible thanks to the help of Drs Jens Gobrecht, Harald Sehr, and Stela Canulescu from PSI, and Dr. Stefan Blunier from the Institute of Mechanical Systems in ETH-Zurich.

Many thanks to Drs. Kurt Klausen, Peter Allenspach, and Michelle Kenzelmann from PSI and to Dr. James Beene, from HRIBF. The support they gave to this project through the leadership of their respective institutions was fundamental for the completion of this work.

I am also very grateful to the operations and technical staff from PSI and HRIBF for their collaboration during beam time.

It is a pleasure to acknowledge the support of the US Department of Energy through contracts at the University of Tennessee and ORNL, and PSI for the financial support of the research reported in this thesis.

Of course, the completion of this project was only possible with a little help from my friends. And I was fortunate enough to get help from both sides of the Ocean. Very special thanks to Perla, Oscar, and Martin for the good times and the many memories we have in Knoxville. Thanks also to Eun Ju for her moral support during the final part of the dissertation. To Ruggero, Loic, Marian, and Nikolai, I can only say *Yach'mat!* Thanks to you, Switzerland felt like home. I also wish to thank to the friends and family who were cheering for me back at home.

Pilar, thanks for helping me with the analysis of the thick target spectra. But of course, your help was much more significant than that. You were my greatest motivation for finishing this work. It was you who always showed me the North, even in the darkest moments. Thanks for being by my side albeit the distance and the long wait. The rest of my life is now yours.

I also want to thank my siblings, Rolando and Diana, for thrusting me along the way. Thanks for the advices, the enthusiasm, and the examples you set. I am very proud of being your brother and I am certain that soon you will accomplish far greater things than I have.

Finally, I thank the root of everything I have accomplished. Obtaining this degree is, above all, a triumph I owe to my parents. In adverse circumstances you made us believe in the power of education and science, in the value of hard work and honesty, and that if we try hard enough it is possible to reach our dreams. This one is to you, mom and dad.

Abstract

Over the last few years, much progress has been made towards the understanding of basic properties of nuclei with extreme neutron to proton ratios. However, the study of phenomena involving spin polarized nuclei near the drip lines remains practically unexplored. The importance of such studies lies in the fact that the most complete knowledge of the scattering matrix is obtained in reactions with polarized particles. The purpose of this dissertation was to explore the feasibility of using polarized probes in reactions with exotic nuclei. We identified areas where reactions between Radioactive Ion Beams (RIBs) and light polarized targets open a new window of opportunity to study the behavior of those nuclei. These include nuclear structure studies using elastic scattering, the investigation of isolated resonances in nuclei of interest for astrophysics, the study of weakly bound nuclei, one nucleon transfer reactions, and reaction mechanisms. Motivated by these potential applications, we developed a polarized proton target with unique capabilities to operate in reactions with heavy ions at low and intermediate energies. Protons in a plastic foil are polarized using the dynamic nuclear polarization method, which requires low temperature operation (~200 mK) and intense magnetic fields (2.5 T). The foils can be prepared using the spin coating technique, resulting in thicknesses between 100 $\mu g/cm^2$ and 20 mg/cm^2. We have demonstrated operation of the target in frozen spin mode (low magnetic field, e.g., 0.8 T), required for experiments at low energies. For experiments with fast beams the target can be operated in dynamic mode reaching polarizations of up to 30% (B=2.5 T, continuous microwave irradiation). The operational limits of the target have been explored at the Paul Scherrer Institute and at the Holifield Radioactive Ion Beam Facility using the thick target technique with ^{12}C beams at 38 MeV and intensities up to 10^7 pps, corresponding to the most intense RIBs available. The dissertation concludes with a series of recommendations for future improvements on the target systems and suggesting the use of the target to further investigate weakly bound systems.

Table of Contents

List of Tables

List of Figures

CHAPTER 1

Introduction

It has been a century since the existence of atomic nuclei was established on firm grounds. Yet a unified description of these systems, that comprise most of the ordinary matter in the Universe and fuel the stars, remains one of the fundamental problems in science. In all fairness, physicists never thought that achieving this goal was a simple task. In a fascinating account of the early days of quantum mechanics, Sin-itiro Tomonaga narrates the difficulties encountered by the pioneers of the field and how the "walls of the sanctuary", the interior of the nucleus, were gradually removed by the work of Heisenberg, Fermi, Yukawa, and others who helped develop the sibling concepts of spin and isospin and realized their importance in the description of the nucleon-nucleon interaction [Tom 97].

The timely development of particle accelerators in the thirties brought the possibility to explore observables as a function of the energy of nuclear reactions. Obviously, those initial studies had to be done using nuclei naturally present on Earth, which restricted them to regions of isospin close to the line of β-stability. By the end of the forties, nuclear physics was a well established field that saw in the shell model its highest achievement, as it was able to explain basic features of nuclei across most known isotopes at that time. The breakthrough of the shell model consisted in incorporating the spin-orbit interaction into the description of the nucleus as a many body system in which independent nucleons move in an average potential. The fact that the spin degree of freedom had such importance not only in few body systems but also in complex nuclei probably led Teller to suggest to Lincoln Wolfenstein, his doctoral student, to explore theoretically the use of spin polarized protons in nuclear reactions[1] [Wol 49]. Over the next few years, Wolfenstein proposed mechanisms to produce polarized protons and to measure their polarization, and developed the formalism to analyze potential scattering experiments with them. Shortly after, the first experiment with polarized protons was performed at Minnesota [Heu 52],

[1] As was acknowledged by Maria Goeppert-Mayer, Teller was engaged in discussions with her during the development of the shell model in Chicago [Goe 63].

effectively opening the possibility of controlling the spin of the particles in nuclear reactions. A summary of those results and of the early work with polarized probes can be found in [Wol 56].

The ability to control the spin of atomic and subatomic particles has had a profound impact in virtually every branch of physics, from the spectacular demonstration of parity violation in Madame Wu's experiment in the fifties, to the technological possibilities offered by the incipient field of spintronics in our days. The spin of an ensemble of particles can be manipulated by orienting them along a particular axis. If in addition, there is a direction for which the possible spin states are not equally populated, the ensemble is said to be polarized. Figure 1.1 illustrates these scenarios for spin ½ particles. The interest in ensembles of polarized particles lies in the fact that the investigation of a physical system requires one to define as exactly as possible its initial and final states. Thus, by using polarized particles, experimenters are able to investigate spin-dependent processes without being forced to average over all the possibilities that might arise from different spin directions, therefore losing valuable information.

Ensembles of polarized particles have been used in nuclear reactions in the form of beams and targets. Their relevance for nuclear structure studies arises as a consequence of the preponderant role played by the spin-orbit interaction in nuclei. In his last public lecture, Fermi illustrated this point by considering the scattering of high energy polarized protons from a complex square well potential with a spin-orbit interaction of the type introduced in the shell model [Fer 54]. Assuming that the first Born approximation

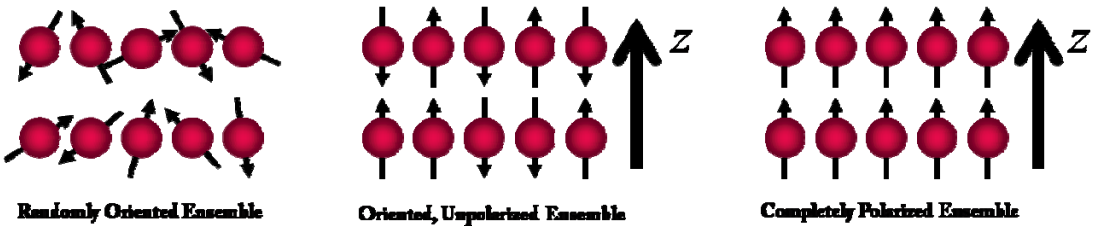

Figure 1.1. Schematics of ensembles of spin ½ particles, where the arrows attached to the particles represent their spin vector. For the system on the left, no quantization axis is specified, leaving the spin of the particles in random orientations. In the center of the figure, the symmetry of the ensemble is broken by defining a preferential axis *z*, along which the spin of the particles is oriented. The ensemble on the right hand side of the figure shows a completely polarized ensemble, in which all spins have identical z component.

holds, Fermi showed that the cross section for elastic scattering is given by:

$$\frac{d\sigma}{d\Omega} = \left|f(\theta, p)\right|^2 \left[1 + \left(\frac{B_\alpha}{B} + Cp^2 \sin\theta\right)\right], \tag{1.1}$$

where θ is the scattering angle, p is the momentum of the incident proton, f is the scattering amplitude for the reaction with unpolarized particles, B and B_α are the real and imaginary depths of the square potential, and C is a constant. Since the scattering depends on the sign of θ, scattering by the same angle to the left and to the right will be different. Evidently, such an asymmetry provides information on the potential that would be washed out in experiments with unpolarized particles. For the case of completely polarized spin ½ particles, the asymmetry is customarily expressed in terms of the scattering intensities to the right (I_{Right}) and to the left (I_{Left}):

$$A_y(\theta, p) = \frac{I_{Right} - I_{Left}}{I_{Right} + I_{Left}}. \tag{1.2}$$

The quantity A_y receives the name of analyzing power of the reaction and it is an observable that can only be measured in nuclear reactions involving polarized probes.

Motivated by the power of polarization observables, polarization studies started to attract significant interest with the development of atomic sources of polarized particles and polarized targets (those pioneered by the Saclay group in France [Abr 62] and by the Berkeley group in the United States [Jef 64] deserve special mention). In 1960, the specialists in polarization studies organized for the first time a conference on this subject under the name of the International Symposium on Polarization Phenomena in Nuclear Physics, in Basel [Hub 61]. The success of the conference was such, that it gave rise to a series of conferences that were held every five years. Much of the polarization formalism, the physics of polarized systems, and the fundamentals of technical developments in the field can be found in the proceedings of the first three symposia [Hub 61], [Pol 66], [Bar 71]. In 1994, the last of those meetings took place in Bloomington. In 2000, the Symposium on Polarization Phenomena was fused with the International Symposium on High Energy Spin Physics, resulting in a new series of conferences: The International Spin Physics Symposia, which are now held biannually. Alternating years with these meetings, the technical aspects of polarization are commonly discussed in the series of conferences known as Polarized Sources and Targets, which celebrated its last edition in 2007 in Kyoto [Ues 07a]. The proceedings from all these conferences constitute a premier source of information for anybody interested in polarization in nuclear and high energy physics.

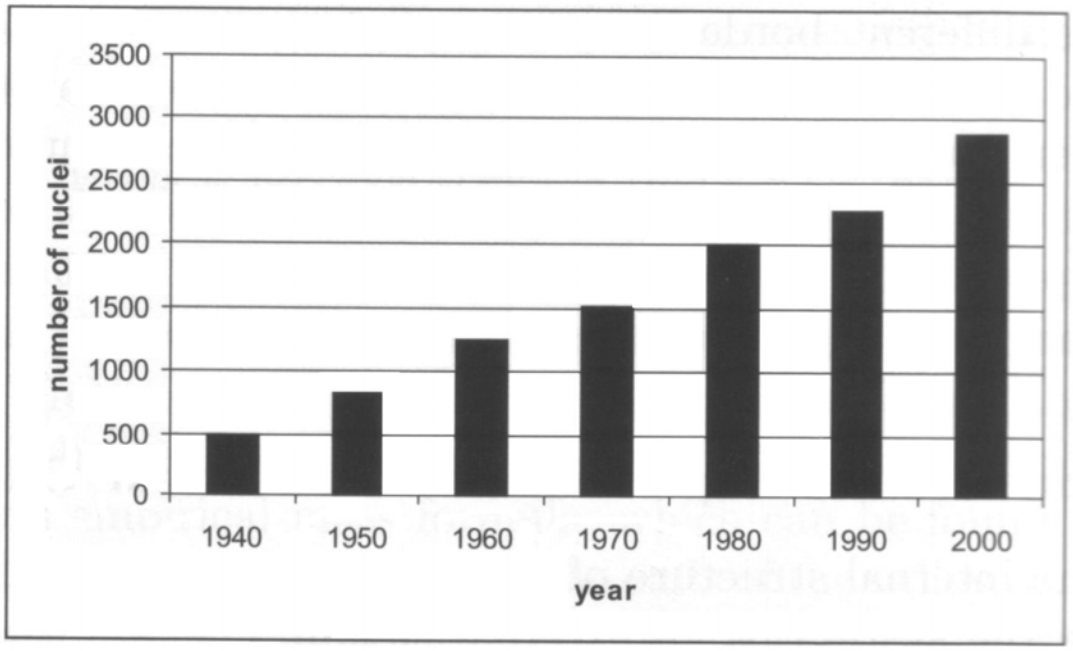

Figure 1.2. Number of known nuclei as a function of time. The columns account for all known nuclei until the year indicated in the graph. The figure has been adapted from [Alk 04].

Aside from polarization studies, nuclear physics has evolved tremendously over the years. An indication of this is given by figure 1.2, where the number of known nuclei is plotted as a function of the year, from the thirties until the decade of 1991-2000. The steady increase in the discovery of isotopes due to developments in accelerator technology has been complemented by the discovery of new methods for studying nuclei. Up to this day, more than 3000 isotopes are known, but only a fraction of these are well studied. A thorough assessment of their properties is not possible based solely on existing nuclear models, it also demands our ability to control one degree of freedom mentioned before: the isospin.

Thanks to the possibility of accelerating nuclear species with exotic N/Z ratios, the old dream of studying nuclei as function of isospin is now being fulfilled. Over the last two decades, the production of Radioactive Ion Beams (RIBs) has become a reality, to the point that the physics of nuclei far from stability constitutes nowadays the most rapidly growing field in nuclear physics. At present, studies with RIBs include measurements of nuclear masses at the limits of stability, decay of very exotic nuclei,

spectroscopic observables of low lying levels, measurements of cross sections and level properties of relevance for astrophysics, and reaction studies at low and intermediate energies.

Until very recently, little or no mention of polarization studies had been done in the context of RIBs [Gal 00a]. In 2003, an exploratory workshop on "Polarized Radioactive Beams and Polarized Targets" held in Strasbourg brought this topic to the attention of the nuclear physics community [Pol 03]. Shortly after that workshop, two efforts aimed to develop polarized targets to be used in reactions with RIBs were consolidated: The CNS-RIKEN project [Wak 05], [Hat 05], and the UTK-ORNL-PSI project [Urr 05], [Urr 07], [Gal 07]. In the last few years, theorists have also become interested in this endeavor. P. Navratil, from Livermore, is now able to calculate polarization observables for low energy reactions involving light nuclei using no-core shell model *ab initio* calculations coupled to resonating group method techniques [Nav 09].

This dissertation has been written with the ultimate goal of bringing attention on spin dependent effects in reactions with RIBs, particularly those performed with reaccelerated beams. To this end, we developed a polarized proton target based on the Dynamic Nuclear Polarization (DNP) method. We demonstrated the operation of the polarized target in a beam of heavy ions in tests performed at the Paul Scherrer Institute (PSI), in Switzerland, while some complementary tests with unpolarized targets were done in the Holifield Radioactive Beam Facility (HRIBF), in the United States. The dissertation has been divided into six chapters. Chapter 2 contains fundamental aspects of the scattering formalism with polarized probes, with special emphasis on the case of elastic scattering of spin ½ particles by spinless nuclei. Chapter 3 introduces the reader into the challenges of experiments with RIBs and explores some of the physics that can be addressed by polarized probes in the context of nuclear structure and nuclear astrophysics. Chapter 4 starts with a brief survey of existing polarized targets technologies and subsequently describes the principles of the DNP method, the construction, and the operation of the polarized target, as well as tests aimed to characterize its cryogenic performance. Chapter 5 describes the tests and performance of the target under experimental conditions similar to those expected in future experiments with RIBs. In particular, it deals with the issues associated with the operation of a cryogenic target under beam irradiation and the challenges encountered in the detection and interpretation of recoil spectra obtained in the presence of the magnetic field required for the operation of the target. Finally, in chapter 6, a summary of the parameters of operation of the target is given along with a discussion on the limitations of the setup and possible improvements. The chapter concludes with an outlook of a possible application of the target.

CHAPTER 2

Scattering of Polarized Particles

2.1 Introduction

Polarization phenomena are susceptible to be observed in any nuclear reaction involving nuclei with non-zero spin. If the reactions are studied in the CM system, where no distinction is made between target and projectile, then the following experiments can, in principle, be done [Ohl 72]:

1) $\vec{a}(b,c)d$: Analyzing power measurements.
2) $\vec{a}(\vec{b},c)d$: Spin correlation measurements (entrance channel).
3) $\vec{a}(b,\vec{c})d$: Polarization transfer measurements.
4) $a(b,\vec{c})d$: Polarization measurements (exit channel).
5) $a(b,\vec{c})\vec{d}$: Spin correlation measurements (exit channel).

The combination of the observables obtained from this set of experiments provides the maximum information attainable from the scattering process [Wol 56], [Ohl 72], [Sat 83]. No mention is done here of experiments requiring the measurement of polarization of three or more particles at a time. This is due to a general result, demonstrated by Simonius [Sim 67], that states that it is always possible to determine all scattering amplitudes at a given energy and angle by considering only two polarized particles at a time.

In the context of RIBs, type 1) experiments are technically the simplest. They require the use of a polarized beam or a polarized target, the latter being a universal probe that can be potentially used with any kind of RIB. The spin observable obtained from these experiments is the analyzing power, which was defined in chapter 1 for the case of spin ½ particles. Experiments of the type 2) correlate spin effects of projectile and target in the scattering process. These are technologically more complex to realize because they require both polarized beams and targets. Type 3) experiments determine coefficients of spin transfer, which have been used in nuclear structure studies to provide information on M1 transition strengths [Nan 87], [Saw 88]. These experiments also involve a polarized target or beam and in addition it is required to measure the polarization of one of the outgoing particles. In practical terms, this implies the use of a

secondary reaction from which that polarization can be established. With current RIBs intensities, this possibility is at best restricted to the most intense species available at major facilities. Type 4) and 5) experiments require the determination of the polarization of one and two of the outgoing particles, respectively. Although no polarized beam or target is required, the weak RIBs intensities might be the main impediment for these types of experiments.

With the development of a polarized proton target, we expect to pioneer experiments 1) to 3) with RIBs. However, due to the information that can be obtained from each type of experiment, to the associated technical challenges, and to the rather weak RIB intensities available, the emphasis of this project is on the use of a polarized target for analyzing power measurements.

This chapter deals with the theoretical description of spin observables and their inclusion into the scattering formalism. Section 2.2 contains a general mathematical description of single particle spin operators and observables based on [Sit 91] and [Sim 74][2]. Then, the concept of density matrix is introduced in order to extend those definitions to ensembles of particles (such as targets and beams). Section 2.3 contains a very condensed description of the scattering formalism in terms of the *S*-matrix and its relation with the partial wave expansion. An effort has been made to include the spin degree of freedom in the formulation while keeping the amount of mathematical expressions as short as possible. The chapter closes with the discussion of elastic scattering of spin ½ particles on spin 0 nuclei, which is relevant for future work with the polarized proton target. Detailed discussions on other cases of interest, such as scattering of spin ½ on spin ½, spin ½ on spin 1, and spin 1 on spin 0 particles can be found in [Mac 60], [Ski 95], and [Ohl 72a] respectively.

2.2 Mathematical Description of Spin Observables

2.2.1 Polarization of a Single Particle

The quantum mechanical state of any particle depends on its spatial coordinates and on the spin variable σ. For a particle with definite spin s, the state $|\psi(\vec{r},\sigma)\rangle$ can be specified as a vector column whose $(2s+1)$-components correspond to different values of σ ($-s \leq \sigma \leq s$). Consequently, spin operators for such a particle are described by $(2s+1)$ row matrices.

[2] For a comprehensive description of polarization observables, see also [Sim 53], [Wol 56], [Ohl 72], [Bar 71], or [Sat 83].

Since the spatial and spin coordinates are independent of each other, the wave function can be written as the products of spatial and spin wave functions. Throughout this chapter, $\chi_{\sigma\mu}$ will denote the eigenfunction of the operators of spin squared $\hat{s}^2$ and spin projection $\hat{s}_z$ on the given direction z:

$$\begin{aligned} \hat{s}^2 \chi_{s\mu} &= s(s+1)\chi_{s\mu} \\ \hat{s}_z \chi_{s\mu} &= \mu \chi_{s\mu} \end{aligned} . \tag{2.1}$$

Since the simultaneous eigenstates of these operators form a complete basis, any spin state χ can be written as a linear superposition of them:

$$\chi = \sum_{\mu=-s}^{s} a_\mu \chi_{s\mu} , \tag{2.2}$$

where the expansion coefficients a_μ can be treated as components of the spin state vector χ.

The polarization vector $\vec{P}$ is defined as the ratio of the expectation value of the spin $\vec{s}$ in the given state χ to the spin value s:

$$\vec{P} = \frac{\langle \chi | \vec{s} | \chi \rangle}{s} . \tag{2.3}$$

The direction of the polarization vector determines the particle spin orientation, whereas its magnitude determines the degree of polarization, that is, the relative probability of spin orientation along a given direction. Using equations (2.1), (2.2), and the commutation rules for the spin operators, one finds from (2.3) that for an arbitrary spin state, the polarization vector is given by :

$$\begin{aligned} \vec{P} = & \frac{1}{2s} \sum_{\mu=-s+1}^{s} \sqrt{(s+\mu)(s-\mu+1)} \left(a_\mu^* a_{\mu-1} + a_\mu a_{\mu-1}^* \right) \hat{x} \\ & - \frac{i}{2s} \sum_{\mu=-s+1}^{s} \sqrt{(s+\mu)(s-\mu+1)} \left(a_\mu^* a_{\mu-1} - a_\mu a_{\mu-1}^* \right) \hat{y} \\ & + \frac{1}{s} \sum_{\mu=-s}^{s} \mu \left| a_\mu \right|^2 \hat{z} \end{aligned} , \tag{2.4}$$

while its magnitude is determined by:

$$\left| \vec{P} \right|^2 = \frac{1}{s^2} \left\{ \left| \sum_{\mu=-s+1}^{s} \sqrt{(s+\mu)(s-\mu+1)} a_\mu^* a_{\mu-1} \right|^2 + \left| \sum_{\mu=-s}^{s} \mu \left| a_\mu \right|^2 \right|^2 \right\} \le 1 . \tag{2.5}$$

If the particle spin is equal to ½, then the expression for the polarization vector is simplified to:

$$\vec{P} = \left(a^*_{1/2}a_{-1/2} + a_{1/2}a^*_{-1/2}\right)\hat{x} - i\left(a^*_{1/2}a_{-1/2} - a_{1/2}a^*_{-1/2}\right)\hat{y} + \left(\left|a_{1/2}\right|^2 - \left|a_{-1/2}\right|^2\right)\hat{z}\,, \quad (2.6)$$

whereas the square of its magnitude is always equal to 1. Hence, the polarization vector of a spin ½ particle completely determines its spin state. However, if the particle spin is greater than ½, a quadratic polarization tensor should be introduced (since $\left|\vec{P}\right|^2 \le 1$). Thus, the polarization tensor, P_{ij} is introduced as defined by the relation:

$$2P_{ij} = \langle \chi | s_{ij} | \chi \rangle\,, \quad (2.7)$$

where

$$s_{ij} \equiv \frac{1}{2}\left(s_i s_j + s_j s_i\right) - \frac{2}{3}\delta_{ij} \quad (2.8)$$

is a symmetric tensor whose trace is equal to zero.

In the general case of a particle with an arbitrary spin *s*, the spin state can be shown to be determined by the polarization tensor of the rank 2*s*. In laboratory measurements, one usually deals with a large amount of particles rather than with individual particle scattering events. Therefore, in order to describe particle scattering under realistic conditions, the definitions given above should be extended to ensembles of particles through the formalism of the density matrix.

2.2.2 Density Matrix

In this section I present a number of results that are relevant to introduce polarization observables in a general context. A detailed and didactic discussion on the density matrix and its properties can be found in [Coh 77]. An incoherent mixture of *N* particles can be described in terms of their wave functions $\psi^{(n)}$(n=1,2,…,N) with statistical weights $w(n)$. Thus, the expectation value of an operator Q in such collective state is determined by:

$$\left\langle \hat{Q} \right\rangle = \frac{\sum_{n=1}^{N} w(n) \left\langle \psi^{(n)} \left| \hat{Q} \right| \psi^{(n)} \right\rangle}{\sum_{n=1}^{N} w(n) \left\langle \psi^{(n)} \middle| \psi^{(n)} \right\rangle}\,. \quad (2.9)$$

The state of the system in which the average values of the physical quantities are determined by (2.9) is referred to as a mixed state.

In general, the wave functions $\psi^{(n)}$ can be expanded in terms of a complete orthonormalized set of eigenfunctions ψ_α of some operator set associated with the system, i.e.,

$$\left|\psi^{(n)}\right\rangle = \sum_{\alpha} a_{\alpha}^{(n)} \left|\psi_{\alpha}\right\rangle . \tag{2.10}$$

Using (2.10), (2.9) can be expressed as:

$$\left\langle \hat{Q} \right\rangle = \frac{\sum_{\alpha,\beta} Q_{\alpha\beta}\rho_{\beta\alpha}}{\sum_{\alpha} \rho_{\alpha\alpha}} , \tag{2.11}$$

where ρ is the density matrix in the α-representation and it is given by:

$$\rho_{\alpha\beta} = \sum_{n=1}^{N} w(n) a_{\alpha}^{(n)} a_{\beta}^{(n)*} . \tag{2.12}$$

Notice that equation (2.11) can be written in a simpler form in terms of the trace of the matrices appearing in that equation:

$$\left\langle \hat{Q} \right\rangle = \frac{Tr\{Q\rho\}}{Tr\{\rho\}} . \tag{2.13}$$

Once the density matrix is known, it is possible to calculate the expectation value of any quantity associated with the system using equation (2.13).

The density matrix possesses interesting properties. Since it is Hermitian and positive definite, it can always be diagonalized by means of a unitary transformation. In addition, if the wave functions $\psi^{(n)}$ are normalized to one and the sum of the statistical weights $w(n)$ is equal to one, then the density matrix satisfies the normalization condition:

$$Tr\{\rho\} = 1 . \tag{2.14}$$

Moreover, under such a condition, it can be shown that:

$$Tr\{\rho^2\} \leq \left(Tr\{\rho\}\right)^2 = 1 . \tag{2.15}$$

Since we are interested in describing the spin properties of an ensemble of particles, it is necessary to introduce here the spin density matrix:

$$\rho = \left\langle \chi\chi^{+} \right\rangle . \tag{2.16}$$

According to (2.3), the polarization of the ensemble of particles can then be defined as

$$\vec{P} = \frac{1}{s} \frac{Tr\{\vec{s}\rho\}}{Tr\{\rho\}} . \tag{2.17}$$

In contrast to pure states for which $|P|=1$, polarization of mixed states described by the density matrix can take any value from -1 to 1. The ensemble of particles (target or beam) is said to be completely polarized if $|P|=1$ and unpolarized if $P=0$.

Similarly, for particles with spin greater than ½, the quadratic polarization tensor is given by:

$$P_{ij} = \frac{1}{s^2}\frac{Tr\{s_{ij}\rho\}}{Tr\{\rho\}}, \tag{2.18}$$

where s_{ij} is the symmetric tensor defined by (2.8).

2.2.3 Spin-Tensor Expansion of the Density Matrix

Although the relationships between the density matrix and the polarization vector and tensor are defined by (2.17) and (2.18), the practical calculation of these quantities could be more cumbersome in some representations than others. Because of this, it is convenient to express the spin dependent operators in terms of irreducible operators, which have the simplest transformation properties [Sil 76].

An irreducible operator of rank I is the set of quantities T_{IM} ($-I \le M \le I$), which are transformed under coordinate rotations as a $(2I+1)$-dimensional irreducible representation of the three-dimensional rotation group, i.e.,

$$T_{IM} = \sum_{M'} D^{I}_{M'M} T'_{IM'}, \tag{2.19}$$

where $D^{I}_{M'M}$ is a finite rotation matrix defined by Euler angles. In addition, any operator can be written as a linear superposition of irreducible tensor operators.

Since spin states are transformed under coordinate system rotations according to [Sak 85]:

$$\left|\chi_{s\mu}\right\rangle = \left|s\mu\right\rangle = \sum_{\mu'} D^{s}_{\mu'\mu}\left|s\mu'\right\rangle, \tag{2.20}$$

and since the hermitian conjugate states are transformed as:

$$\left\langle\chi_{s\mu}\right| = \left\langle s\mu\right| = \sum_{\mu'} (-1)^{s-\mu} D^{s}_{\mu'\mu}\left\langle s-\mu'\right|, \tag{2.21}$$

then the irreducible tensor operator T_{IM} can be constructed by making use of the rules for addition of angular momenta to obtain:

$$T_{IM} = \alpha \sum_{\mu\mu'} (-1)^{s-\mu}\left\langle s'\mu' s-\mu\middle| IM\right\rangle\left\langle s'\mu'\middle| s\mu\right\rangle, \tag{2.22}$$

where α is an arbitrary constant usually determined from the normalization condition imposed on T_{IM}.

According to (2.22), the irreducible tensor operator T_{IM} in the representation determined by the spin squared and the spin projection $|s\mu\rangle$ is described by a matrix whose elements reproduce the Clebsch-Gordan coefficients (with the exception of the phase factors):

$$\begin{aligned} &\langle s'\,\mu'|T_{IM}\,|\,s\mu\rangle = \alpha(-1)^{s-\mu}\langle s'\,\mu'\,s-\mu\,|\,IM\rangle \\ &|s-s'|\le I\le s+s' \end{aligned}. \tag{2.23}$$

The matrices (2.23) with different I and M form an orthogonal set and are called spin tensors. Evidently, if $s=s'$, then these are square matrices. In that case, for a given s, the orthogonal set of spin tensors defined by:

$$\begin{aligned} &\langle s\mu'|T_{IM}\,|\,s\mu\rangle = (-1)^{s-\mu}\sqrt{2s+1}\langle s\mu'\,s-\mu\,|\,IM\rangle \\ &I=0,1,...,2s;\quad -I\le M\le I \end{aligned}, \tag{2.24}$$

forms a complete set that serves as an expansion basis for any operator acting on the system with fixed s. Moreover, such a set of operators satisfies the normalization condition:

$$Tr\left\{T_{IM}T^{+}_{I'M'}\right\} = (2s+1)\delta_{II'}\delta_{MM'}\,. \tag{2.25}$$

Using this normalization the zero-rank spin tensor coincides with the unit matrix, while the first-rank tensors are expressed in terms of the spin matrices by linear relations:

$$\begin{aligned} T_{00} &= 1 \\ T_{10} &= \sqrt{\frac{3}{s(s+1)}}s_z \\ T_{1\pm1} &= \mp\sqrt{\frac{3}{2s(s+1)}}(s_x \pm is_y) \end{aligned}\,. \tag{2.26}$$

Expressions for the second-rank tensors T_{2M} are important for spin 1 particle scattering (e.g., d scattering) and involve quadratic combinations of spin matrices and can be explicitly found elsewhere [Bar 71], [Ohl 72], [Sim 74], [Sat 83], [Sit 91].

Spin states of a system of particles with spin s are generally described by a $(2s+1)$-row density matrix. Since the density matrix is Hermitian, it contains only $(2s+1)^2$ independent parameters. If in addition it is normalized as given by (2.14), then $4s(s+1)$ parameters are required to describe it. Since the T_{IM} tensors form a complete set of operators, the density matrix can be expanded in terms of them, resulting in:

$$\rho = \frac{1}{2s+1}\sum_{I=0}^{2s}\sum_{M=-I}^{I}\left\langle T_{IM}^{+}\right\rangle T_{IM}\ , \tag{2.27}$$

where

$$\left\langle T_{IM}\right\rangle = Tr\left\{T_{IM}\rho\right\}. \tag{2.28}$$

Using this expression for the density matrix, the description of polarized particles can treated in terms of the set of tensors T_{IM}. In the special case of spin ½ particles, the spin tensors (2.26) become:

$$\begin{aligned} T_{00} &= 1 \\ T_{10} &= \sigma_z \\ T_{1\pm1} &= \mp\frac{1}{\sqrt{2}}\left(\sigma_x \pm i\sigma_y\right) \end{aligned}\ , \tag{2.28}$$

where σ_x, σ_y, and σ_z are the Pauli matrices. The expansion coefficients in (2.27), according to (2.28) and (2.17), are functions of the particle density and the polarization vector:

$$\left\langle T_{10}\right\rangle = P_z, \quad \left\langle T_{1\pm1}\right\rangle = \mp\frac{1}{\sqrt{2}}\left(P_x \mp iP_y\right). \tag{2.29}$$

Therefore, the matrix density can be expressed as:

$$\rho = \frac{1}{2}\left(1 + \vec{P}\cdot\vec{\sigma}\right). \tag{2.30}$$

Similar expressions for spin 1 particles can be found in [Bar 71].

2.3 Scattering of Polarized Particles

The most general description of scattering phenomena is given by the collision matrix (*S*-matrix) formalism, introduced by Heisenberg. The *S*-matrix is a unitary operator connecting states in the entrance channel α of a reaction with states β in the exit channel:

$$\left|\vec{k}'s'\mu'\right\rangle_{\beta} = S_{\beta\alpha}\left|\vec{k}s\mu\right\rangle_{\alpha}, \tag{2.31}$$

where $\vec{k}$ and $\vec{k}'$ represent the momenta of the particle in channels α and β, respectively. According to its definition, the *S*-matrix contains all the information of the interaction responsible for the scattering process. Hence, its complete determination would become the ultimate test for reaction mechanisms and nuclear structure theories.

In the *S*-matrix formalism, the scattering problem by a central potential is equivalent to solving the Lipmann-Schwinger equation through the use of a Green function [Mer 98]. In particular, the differential

cross section for scattering of a particle of spin s and magnetic quantum number μ into a state with magnetic quantum number μ' by a spin 0 particle is given by

$$\frac{d\sigma}{d\Omega}(\theta,\varphi)=\left|f_{\mu\mu'}(\theta,\varphi)\right|^2, \tag{2.32}$$

where $f_{\mu\mu'}$ is the scattering amplitude, which is related to the transition matrix $\hat{t}$ and to the S-matrix through:

$$f_{\mu\mu'}(\theta,\varphi)=-\frac{m}{2\pi\hbar^2}\left\langle\vec{k}'\mu'\middle|\hat{t}\middle|\vec{k}\mu\right\rangle=\frac{im}{4\pi^2\hbar^2}\left\langle\vec{k}'\mu'\middle|\hat{1}-\hat{S}\middle|\vec{k}\mu\right\rangle. \tag{2.33}$$

If the particles in the entrance channel are unpolarized and the final spin projection is not fixed, then the differential cross section is given by the average of all probable spin projections, which removes the dependence on the azimuthal angle and leads to the familiar expression for the cross section in terms of $|f(\theta)|^2$ found in most elementary books on quantum mechanics:

$$\frac{d\sigma}{d\Omega}(\theta)=\frac{1}{2s+1}\sum_{\mu\mu'}\left|f_{\mu\mu'}(\theta,\varphi)\right|^2=\left|f(\theta)\right|^2. \tag{2.35}$$

Equation (2.35) can be generalized to the case when both particles in the entrance channel posses spin ($\chi_{s_1\mu_2}, \chi_{s_1\mu_2}$), for which it is necessary to introduce the concept of channel spin. Each spin channel is defined by the addition of the angular momenta of the reactants and it is described by the wave function $\chi_{s\mu}$ obtained through the addition rules:

$$\left|\chi_{s\mu}\right\rangle=\sum_{\mu_1\mu_2}\left\langle s_1\mu_1 s_2\mu_2\middle|s\mu\right\rangle\left|\chi_{s_1\mu_1}\right\rangle\left|\chi_{s_2\mu_2}\right\rangle. \tag{2.36}$$

Using this wave function, scattering from different entrance channels can be described in the same manner as scattering of a particle with spin s by a spin zero particle. One can then use the transition operator to find the scattering amplitude for a spin channel $f_{s\mu s'\mu'}$ in complete analogy to (2.33). However, since the scattering amplitude of spin channels are not observable quantities *per se*, one should compute $f_{\mu_1\mu_2\mu_1'\mu_2'}$ rather than $f_{s\mu s'\mu'}$. The former can be expressed in terms of the latter by:

$$f_{\mu_1\mu_2\mu_1'\mu_2'}(\theta,\varphi)=\sum_{s\mu s'\mu'}\left\langle s_1\mu_1 s_2\mu_2\middle|s\mu\right\rangle\left\langle s_1\mu_1' s_2\mu_2'\middle|s'\mu'\right\rangle f_{s\mu s'\mu'}(\theta,\varphi). \tag{2.37}$$

If the spin projections of the particles in the entrance and exit channels are not fixed, then the average over initial and final states yields a differential cross section analogous to (2.35):

$$\frac{d\sigma}{d\Omega}(\theta)=\frac{1}{(2s_1+1)(2s_2+1)}\sum_{\mu_1\mu_2\mu_1'\mu_2'}\left|f_{\mu_1\mu_2\mu_1'\mu_2'}(\theta,\varphi)\right|^2. \tag{2.38}$$

In actual cases, where the beams and targets are described by density matrices, the relation between the initial and final density matrices can be derived from $|\chi'\rangle = \hat{f}|\chi_\mu\rangle$. Then, under a proper normalization choice, the final density matrix of the system is given by:

$$\rho' = \langle \chi' \chi'^{+} \rangle = f\rho f^{+} . \tag{2.39}$$

Consequently, the differential cross section is given by:

$$\frac{d\sigma}{d\Omega}(\theta,\varphi) = \frac{Tr\{\rho'\}}{Tr\{\rho\}} = \frac{Tr\{f\rho f^{+}\}}{Tr\{\rho\}} . \tag{2.40}$$

Such an expression can be reduced to a combination of tensor operators for a particular spin value. The simplest case is the elastic scattering of a particle with spin ½ by a spinless particle, which is explicitly shown in the next section.

2.4 Spin ½ - Spin 0 Elastic Scattering

The spin operator *s* of a spin ½ particle is determined by the Pauli matrices $\boldsymbol{\sigma}$.

$$s_k = \frac{1}{2}\sigma_k . \qquad k = x, y, z , \tag{2.41}$$

where

$$\sigma_x = \begin{pmatrix} 0 & 1 \\ 1 & 0 \end{pmatrix}, \quad \sigma_y = \begin{pmatrix} 0 & -i \\ i & 0 \end{pmatrix}, \quad \sigma_z = \begin{pmatrix} 1 & 0 \\ 0 & -1 \end{pmatrix} . \tag{2.42}$$

The eigenvectors of the spin squared and the spin projection operator along the *z* axis are:

$$\chi_{1/2,1/2} = \begin{pmatrix} 1 \\ 0 \end{pmatrix}, \quad \chi_{1/2,-1/2} = \begin{pmatrix} 0 \\ 1 \end{pmatrix} . \tag{2.43}$$

Since the Pauli matrix together with the unit matrix form a set of complete observables, any two by two matrix can be written as a linear combination of them. In particular, the density matrix describing the target (or beam) particles can be expressed as:

$$\rho = a\hat{1} + \vec{b} \cdot \vec{\sigma} , \tag{2.44}$$

where the constants *a* and b_k have a distinctive physical meaning. If the sum of the statistical weights in equation (2.12) corresponds to the density of particles in the target (or beam), then the quantity *a* is related to the particle density n_0 as:

$$n_0 = Tr\{\rho\} = 2a , \tag{2.45}$$

while $\vec{b}$ is proportional to the polarization vector $\vec{P}$:

$$\vec{P} = \frac{Tr\{\vec{\sigma}\rho\}}{Tr\{\rho\}} = \frac{2\vec{b}}{n_0}. \tag{2.46}$$

Thus, the density matrix of an ensemble of particles with arbitrary polarization can be represented in the form:

$$\rho = \frac{n_0}{2}\left(\hat{1} + \vec{P}\cdot\vec{\sigma}\right). \tag{2.47}$$

Hence, if the particles are completely polarized in the positive direction along the *z* axis, then:

$$\rho = \begin{pmatrix} n_0 & 0 \\ 0 & 0 \end{pmatrix}, \tag{2.48}$$

but if the ensemble is completely unpolarized, then the density matrix is simply:

$$\rho = \begin{pmatrix} n_0/2 & 0 \\ 0 & n_0/2 \end{pmatrix}. \tag{2.49}$$

On the other hand, the density matrix ρ' of the scattered particles is expressed in terms of the density matrix in the entrance channel and the scattering amplitude *f* according to (2.39). The scattering amplitude can in turn be expanded in terms of the unit and Pauli matrices:

$$f = g\hat{1} + \vec{h}\cdot\vec{\sigma}, \tag{2.50}$$

Where *g* and *h* are functions determined by the geometry of the collision, i.e., by the initial and final momenta $\vec{k}$ and $\vec{k}'$, respectively. Following Wolfenstein and Ashkin, it is possible to gain additional information on *f* by using symmetry considerations [Wol 52]. Since the amplitude of scattering is invariant under rotations and reflections of the coordinate system, the two summands on the right hand side of (2.50) should be too. As a result, *g* must be scalar and h must be a pseudovector (since the spin σ is also a pseudovector). Since $\vec{k}$ and $\vec{k}'$ cannot form any pseudovectors other than $\vec{k}\times\vec{k}'$, $\vec{h}$ can be written as:

$$\vec{h} = h\vec{n}, \tag{2.51}$$

Where *h* is a scalar and $\vec{n}$ is the unit vector perpendicular to the scattering plane:

$$\vec{n} = \frac{\vec{k}\times\vec{k}'}{\left|\vec{k}\times\vec{k}'\right|}. \tag{2.52}$$

Thus, the scattering amplitude (2.50) is reduced to:

$$f = g + h\vec{n}\cdot\vec{\sigma}\,, \tag{2.53}$$

where the scalar amplitudes g and h are complex numbers that contain all the information of the scattering process. In other words, g and h are directly related to the S-matrix. In order to make explicit such a connection, it is convenient to expand the scattering amplitudes in terms of the scattering phase shifts. Before proceeding, it should be noticed that in the general case, the interaction potential of spin-possessing particles is non-central, which leads to phase shifts defined not only by the orbital angular momentum number but also by the total angular momentum number. In other words, for a state with fixed total angular momentum j, the orbital angular momentum number l can take the values $l=j+1/2$ and $l=j-1/2$, which are associated with different parities. Therefore, if the interaction preserves parity, then the scattering matrix is diagonal with respect to the quantum numbers l and l':

$$S^{j}_{l'1/2,l1/2} = \delta_{ll'}S^{j}_{l}\,. \tag{2.54}$$

Since the S-matrix is unitary, it can be parametrized in the form:

$$S^{j}_{l} = \exp\left(2i\delta^{j}_{l}\right), \tag{2.55}$$

where the δ^{j}_{l} are real scattering phase shifts in the states with fixed j and l. If some channels other than the elastic scattering are also open, then the phase shifts are complex.

In order to find the explicit forms of g and h, the spin dependence of the scattering matrix should be taken into account. This can be done by introducing projection operators onto states with a common l. Thus, for $j=l\pm1/2$ the projection operators $\prod_{l\pm(1/2)}$ are defined as:

$$\prod_{l+(1/2)} = \frac{l+1+\vec{l}\cdot\vec{\sigma}}{2l+1}, \quad \prod_{l-(1/2)} = \frac{l-\vec{l}\cdot\vec{\sigma}}{2l+1}\,, \tag{2.56}$$

where $\vec{l} = -i\vec{n}\dfrac{\partial}{\partial\theta}$ is the angular momentum operator. Using these two operators, the S-matrix can be written as:

$$S_l = S_l^{j=l+(1/2)}\prod_{l+(1/2)} + S_l^{j=l-(1/2)}\prod_{l-(1/2)}\,. \tag{2.57}$$

Recalling that for elastic scattering the S-matrix is directly related to the scattering amplitude through the relation:

$$f\left(\vec{k},\vec{k}'\right) = \frac{i}{2k}\sum_{l=0}^{\infty}(2l+1)(1-S_l)P_l(\cos\theta)\,, \tag{2.58}$$

One can then use (2.50) to find g and h:

$$g(\theta)=\frac{i}{2k}\sum_{l=0}^{\infty}\left\{2l+1-(l+1)\exp\left(2i\delta_l^{l+(1/2)}\right)-l\exp\left(2i\delta_l^{l-(1/2)}\right)\right\}P_l(\cos\theta)$$
$$h(\theta)=-\frac{i}{2k}\sum_{l=0}^{\infty}\left\{\exp\left(2i\delta_l^{l+(1/2)}\right)-\exp\left(2i\delta_l^{l-(1/2)}\right)\right\}\frac{\partial}{\partial\theta}P_l(\cos\theta) \quad . \tag{2.59}$$

At this point, it is illustrative to consider two situations. First, I will assume that particles in the entrance channel are unpolarized. In such a case, the density matrix coincides with the unit matrix. Since the cross section is given by the ratio of the traces of the scattered and incident density matrices, one can show that this reduces to:

$$\frac{d\sigma}{d\Omega}(\theta)=|g(\theta)|^2+|h(\theta)|^2 \quad . \tag{2.60}$$

In this case, according to (2.17), the particle polarization produced by scattering turns out to be directed along $\vec{n}$, i.e., normal to the scattering plane and it is given by:

$$\vec{P}=P\vec{n} \quad , \tag{2.61}$$

where the modulus of the polarization corresponds to:

$$P=\frac{2\,\mathrm{Re}\{gh^*\}}{|g|^2+|h|^2} \quad . \tag{2.62}$$

This result clearly indicates that polarization arises as a consequence of the interference between different scattering amplitudes.

The second situation to be considered is more relevant for initial applications of the polarized target that are described in this dissertation (experiments type 1 defined at the beginning of this chapter). It is concerned with an ensemble of particles in the entrance channel with initial polarization $\vec{P}_0$. Here, according to (2.47), the initial density matrix is given by:

$$\rho=\frac{n_0}{2}\left(\hat{1}+\vec{P}_0\cdot\vec{\sigma}\right), \tag{2.63}$$

While the density matrix in the exit channel can be obtained by replacing (2.63) into (2.39) and using (2.53):

$$\rho'=\frac{n_0}{2}\left(g+h\vec{n}\cdot\vec{\sigma}\right)\left(\hat{1}+\vec{P}_0\cdot\vec{\sigma}\right)\left(g^*+h^*\vec{n}\cdot\vec{\sigma}\right). \tag{2.64}$$

The cross section can be calculated as before, by taking the ratio between the traces of the density matrices in the exit and entrance channels. This can be done by using algebraic properties of the Pauli matrices, resulting in:

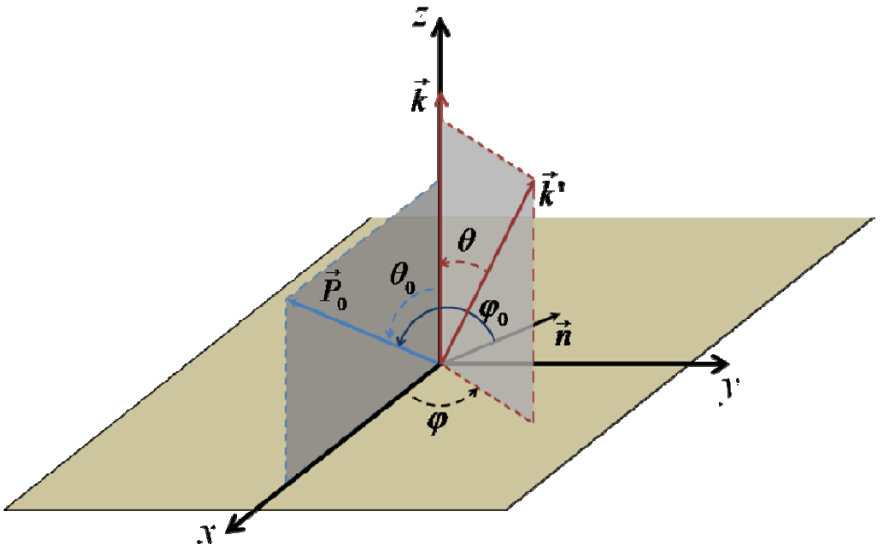

Figure 2.1. Scattering of polarized particles in the laboratory system, where the wave vector of the incident particle $\vec{k}$ defines the z direction. The initial polarization lies on the x-z plane and it is specified by the angle θ_0. Scattered particles can be detected along the scattering plane at angles (θ, φ). φ_0 is the angle between the initial polarization vector and the normal to the scattering plane $\vec{n}$. For this choice of axes, $\cos\varphi_0 = \sin\theta_0 \cos[(\pi/2)+\varphi]$. If $\theta_0 = \pi/2$, then $\varphi_0 = \pi/2 + \varphi$.

$$\frac{d\sigma}{d\Omega}(\theta,\varphi) = \left(|g(\theta)|^2 + |h(\theta)|^2\right)\left(1 + \vec{P}_0 \cdot \vec{A}\right), \tag{2.65}$$

where $\vec{A}$ is called the analyzing power of the reaction and it is equal to the polarization vector $\vec{P}$ that would be produced by scattering of unpolarized particles (equations (2.61) and (2.62)). The first factor in (2.65) is the differential cross section (2.60) for the reaction with unpolarized particles, while the second factor,

$$\left(1 + \vec{P}_0 \cdot \vec{A}\right) = 1 + P_0 A \cos\varphi_0 , \tag{2.66}$$

is responsible for the azimuthal asymmetry that occurs after scattering of polarized particles. In this expression, φ_0 is the angle between the particle polarization in the entrance channel and the normal to the scattering plane (see figure 2.1). If the initial polarization is perpendicular to the incident momentum, then expanding (2.66) in terms of spherical harmonics results in:

$$\left(1 + \vec{P}_0 \cdot \vec{A}\right) = 1 + P_0 \sin\theta \sin\varphi \sum_{l=1}^{\infty} a_l \frac{d}{d(\cos\theta)} P_l(\cos\theta), \tag{2.67}$$

where (θ,φ) are the spherical angles at which the particle is detected in the laboratory system and a_l is the expansion coefficient associated with the derivative of the Legendre polynomial P_l.

It is evident from equations (2.66) and (2.67) that polarization effects on scattering are maximized when the initial polarization is perpendicular to the scattering plane. In addition, these two equations indicate two alternative methods to measure the analyzing power of a reaction. The first method consists in measuring the left-right asymmetry introduced by the odd-parity factor $sin\theta$ in (2.67). As a consequence of such a factor, the analyzing power can be seen to be an odd function of the angle, which means that for a given initial polarization, the difference between the number of scattered particles to the right and to the left is proportional to the magnitude of the analyzing power:

$$A = \frac{1}{P_0 \cos\varphi} \frac{\frac{d\sigma}{d\Omega}(\theta,\varphi) - \frac{d\sigma}{d\Omega}(-\theta,\varphi)}{\frac{d\sigma}{d\Omega}(\theta,\varphi) + \frac{d\sigma}{d\Omega}(-\theta,\varphi)}. \tag{2.68}$$

Determining the analyzing power based on this equation is a method well suited for experiments with polarized beams that is independent on beam normalization, but requires well characterized detector efficiencies and alignment conditions.

The second method for measuring analyzing powers comes from observing that independent measurements of cross section at given angles (θ, φ) with opposite initial polarizations can be combined into:

$$A = \frac{1}{P_0 \cos\varphi} \frac{\left.\frac{d\sigma(\theta,\varphi)}{d\Omega}\right|_{\vec{P}_0} - \left.\frac{d\sigma(\theta,\varphi)}{d\Omega}\right|_{-\vec{P}_0}}{\left.\frac{d\sigma(\theta,\varphi)}{d\Omega}\right|_{\vec{P}_0} + \left.\frac{d\sigma(\theta,\varphi)}{d\Omega}\right|_{-\vec{P}_0}}. \tag{2.69}$$

This method is only possible if beam normalization can be established for the two independent measurements required. In chapter 5 it is demonstrated that such is indeed the case for the polarized target developed during this work.

The formulae presented in this chapter are general. However, the choice of the coordinate system best suited for calculating or measuring polarization observables is completely arbitrary. This was an issue in the early days of polarization experiments, when often authors published their results using different reference frames, which made direct comparisons impossible. In response to this situation, the 3rd International Conference on Polarization Phenomena established a set of guidelines for defining the

reference system, known as the "Madison Convention" [Bar 71]. For scattering of spin ½ particles by spinless nuclei, the Madison convention states that the z axis should coincide with the direction of the incident momentum, while the normal to the scattering plane defines the *y* axis (which is positive in the direction determined by $\vec{k} \times \vec{k}'$). In virtue of this choice of axis, the analyzing power is referred to simply as A_y.

CHAPTER 3

Perspectives of Polarization in Experiments with RIBs

3.1 Introduction

New and exciting opportunities in the study of nuclei far from stability in both the neutron and proton rich sides are opening at several radioactive beam facilities around the world. The exploration of new regions of isospin constitutes nowadays one of the major fields in nuclear science [Nup 04], [Nsa 07]. As we move away from stability, the determination of experimental observables becomes increasingly challenging due to low intensity beams, short lived species and high background. In order to circumvent these difficulties it is necessary to develop new and adapt old experimental tools that, in conjunction with the available instrumentation, would allow us to measure relevant nuclear properties. In this context, the development of a polarized target will constitute a new and important tool for the study of exotic nuclei.

This chapter describes the physics motivations of studying polarization observables in experiments with RIBs. Section 3.2 gives a very broad description of the field of RIBs. In section 3.3, I present several examples where the use of polarized beams and stable targets has resulted in valuable information, unlikely to be found by other means. Following each case, I provide a short description of systems in which analogous experiments with RIBs could be of interest.

3.2 Radioactive Ion Beams

Roughly speaking, the physics of the atomic nucleus is defined by three fundamental degrees of freedom: Temperature (E, excitation energy), spin (I, angular momentum), and the ratio of neutrons to protons (T, isospin). Since the discovery of natural radioactivity by Becquerel in 1896 until very recently, nuclear physicists had constrained their studies to a narrow region of such phase space around the E-I plane, due to the technical challenges associated with the production of nuclei with desired combinations of protons and neutrons. This resulted in a picture of atomic nuclei along the stability line that included fundamental insights on the nucleon-nucleon interaction, the role of two and three body forces, mean field effects, stability against Coulomb breakup and fission, among others. However, successful as they have been,

studies based on nuclei along or close to the stability line have left unanswered a number of important questions [Nsa 07], including:

1. How many neutrons can we add to a stable nucleus before it can not hold any more?
2. What is the nature of the nuclear force that binds protons and neutrons into stable nuclei and rare isotopes?
3. What is the origin of simple patterns in complex nuclei?
4. What is the nature of neutron stars and dense nuclear matter?
5. What is the origin of the elements in the cosmos?
6. What are the nuclear reactions that drive stars and stellar explosions?

These questions have been identified by the nuclear physics community as guiding marks in our scientific endeavors. In consequence, the field of RIBs has become the fastest growing field in nuclear physics over the last few years, leading to a number of important and surprising discoveries (including exotic nuclear forms, like halo nuclei or neutron skin, new decay modes, the breakdown of the shell model, and the effects of shell corrections in superheavy elements).

Up to some extent, the research effort in the field of exotic nuclei has been driven by experiments. The facilities around the world that constitute the main centers for the study of exotic nuclei are indicated in figure 3.1. Those facilities make use of two methods to produce RIBs: the in-flight Projectile Fragmentation (PF) and the Isotope Separation On-Line (ISOL) methods. The two approaches are complementary in the sense that PF is best suited for experiments at high and intermediate energies ($E >\sim 30$MeV/A), whereas the ISOL technique allows the use of high quality beams in experiments at low energies ($E<\sim 10$MeV/A). Useful reviews about these methods can be found in [Alk 04], [Huy 02].

The fragmentation method is illustrated in figure 3.2(*a*). Production of short lived nuclear species occurs upon fragmentation of a high energy, stable beam in peripheral collisions with nuclei from a thin target. The fragments are then directed into a spectrometer, where nuclei of interest are selected and focused based on various combinations of atomic number, mass, charge, momentum and time of flight. Since the reaction products are emitted in the forward direction with about the same velocity as the primary beam, no post-acceleration is needed. The method also has the advantages that the production rates of RIBs are independent of their chemical properties and that there is no fundamental limitation on the RIBs that can be produced due to their lifetimes[3]. Production rates are limited by the primary beam intensity (typically

[3] The only limitation is the transit time of the RIB through the spectrometer, until it reaches the target of the experiment for which it was produced.

Figure 3.1. Major radioactive beam facilities around the world. In addition to these facilities, plans for a new generation of facilities are under way in the U.S.A (FRIB) and in Europe (EURISOL).

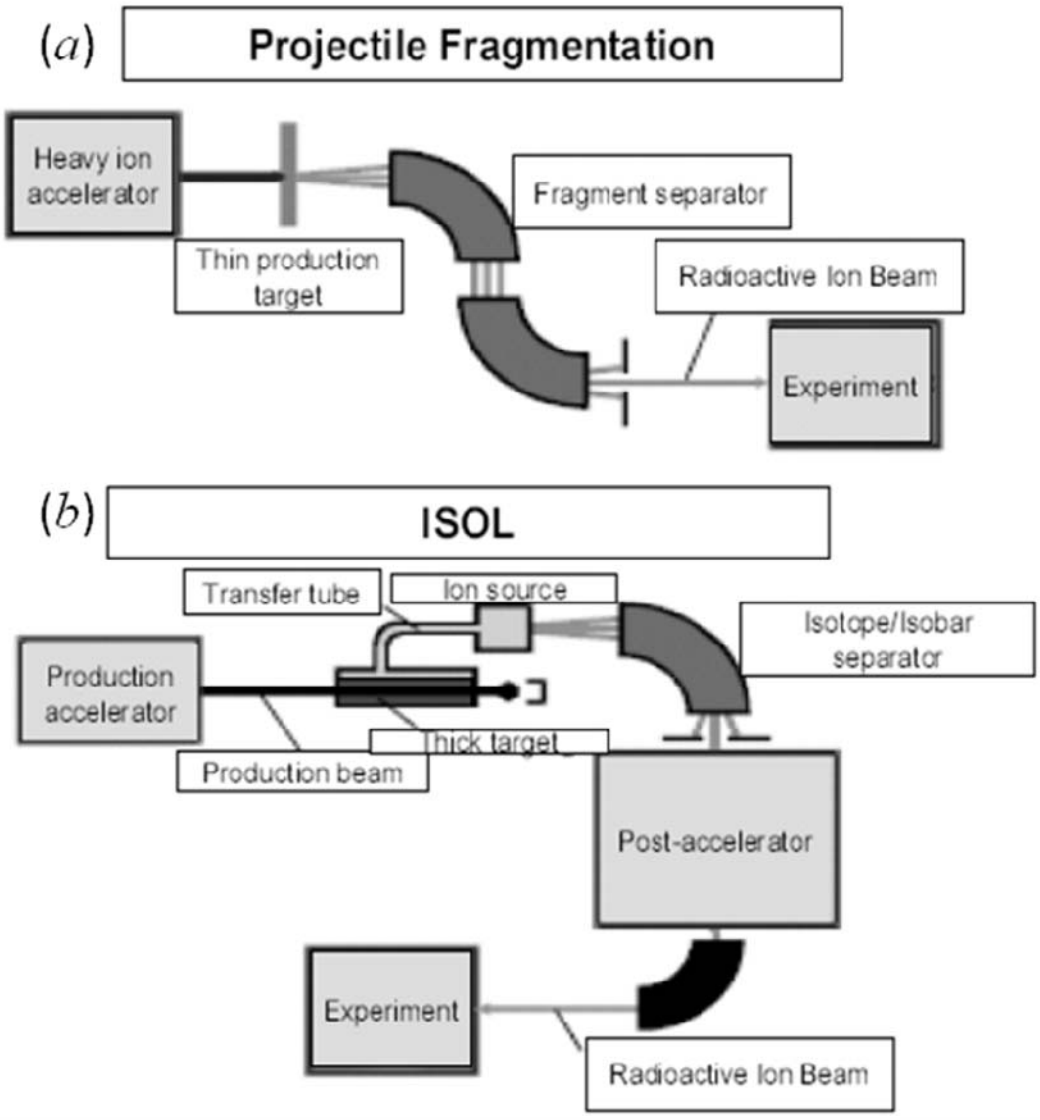

Figure 3.2. Production methods of RIBs (adapted from [Lee 07]). The upper panel of the figure illustrates the projectile fragmentation method, whereas the lower panel depicts the fundamental components of the ISOL method.

~6*10^{12}pps), the acceptance of the spectrometers, and the quality of the ion optics throughout the beam line. The main problem associated with this scheme is that the beam quality can be affected by the initial momentum dispersion of the beam and aberrations in the ion optics.

In contrast with the PF method, the ISOL method requires the use of two accelerators. Radioactive nuclei are first produced in reactions induced by intense beams of light particles impinging on a thick target, as schematically shown in figure 3.2(*b*). The products from the reaction diffuse out of the target and are eventually extracted into an ion source. Upon ionization, radioactive nuclei can then be fed into the second accelerator in an analogue way than stable nuclei would. In this manner, a high quality beam can be obtained, although it is often difficult to achieve isobaric purity.

At present, there are two leading efforts in the world to develop the next generation of RIB facilities: FRIB and EURISOL. One long term goal of the nuclear physics community is to combine the best of the PF and ISOL methods in a single facility. Such an approach is based on the concept of accelerating a fast beam of light particles (~1GeV) onto a thick target. The reaction products are slowed down by passage through a suitable material and stopped inside a gas cell, from which they can be extracted, separated by mass, and then reaccelerated to the desired energy [Gee 06].

3.2.1 Experimental Challenges with RIBs

The study of nuclei far from stability relies on the production of RIBs by one of the methods mentioned above. However, the challenges associated with experiments involving RIBs extend far beyond that stage. Although each experiment has its own particular requirements, in most cases experimenters have to cope with the typically low RIB intensities available, the lack of isotopically pure beams, the large radioactive background associated with the finite lifetime of the beam, and the use of inverse kinematics.

3.2.1.1 Weak Beam Intensities – Thick-Target Technique

Due to the complex production mechanisms of RIBs, their intensities on experimental targets typically lie in the range below 10^6pps, with very few exceptions reaching more than 10^7pps. As an example, figure 3.3 illustrates the production rates of beams available at HRIBF. In contrast with these intensities, rates for beams of stable isotopes can easily be five or six orders of magnitude higher. As a consequence, reactions with RIBs often yield low statistics spectra, a situation that might be worsen by low cross sections of phenomena of interest. Such issue is dealt with long experimental runs and, especially, with efficient detection techniques that maximize the amount of information conveyed by each experiment and

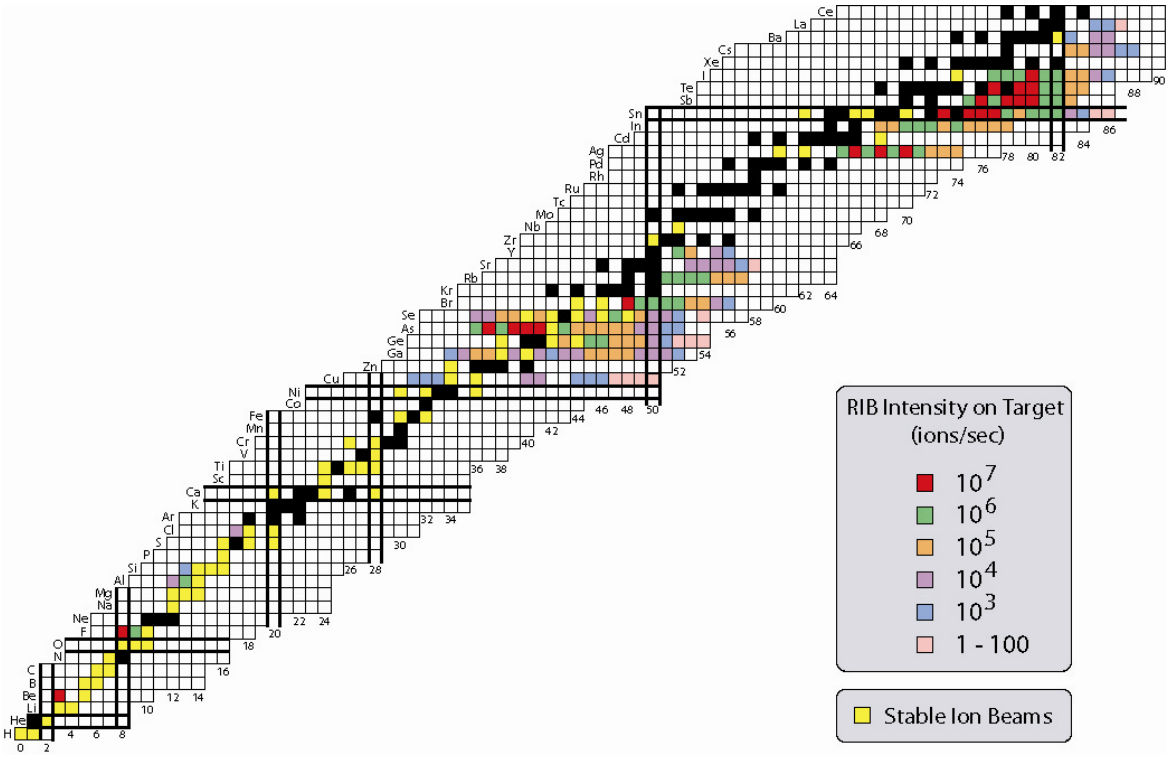

Figure 3.3. RIB intensities currently available at HRIBF at Oak Ridge National Laboratory [Str 09]. This state of the art ISOL facility provides some of the most intense RIBs from fission fragments in the world.

reduce possible systematic errors inherent to long measurement processes. Examples of such techniques include the use of multiple detection systems, the use of arrays of detectors covering a large area of the phase space, and, in the case of elastic scattering experiments, the use of the so called thick-target technique [Gal 00].

Due to the relevance of the thick-target technique for some of the foreseen applications of the polarized target, I will address its foundations here. Typically, in normal kinematics experiments with stable nuclei, resonant scattering measurements have consisted mainly of excitation functions at a few angles. Even for conventional techniques using normal kinematics and a thin target (~100μg/cm^2) the measurement of excitation functions with small energy steps is very time consuming. Using a thick target constitutes a powerful method for the efficient determination of relative excitation functions at a single bombarding energy. To the best of my knowledge, thick targets were first used for such purposes in the fifties (see, for instance [Bro 51] and [Kaf 56), and have been rediscovered in the early nineties in the context of RIBs

[Gal 91a], [Ben 92]. In this technique, the projectile is slowed down or completely stopped in the target, effectively varying its energy during deceleration and possibly exciting several resonances along its trajectory. The light recoils (e.g. *p, d*), on the other hand, might exit the target as their ionization power is much lower than the the ionization power of the beam.

The thick target technique is specially suited for low energy studies with light nuclei in inverse kinematics. The reason being that in these systems, their low lying energy levels are well separated, which leaves the corresponding groups of scattered particles well resolved in energy. A detailed analysis of this technique applied to the case of an isolated Breit-Wigner resonance excited by elastic scattering has been done by Benjelloun et al. [Ben 92]. Their analysis takes into account the beam energy loss and straggling in the target, the multiple scattering of the beam particles, the target inhomogeneity, and the energy loss and straggling of the light recoils in the target. Such factors are convoluted with the cross section from the Breit-Wigner shape, resulting in a precise determination of the resonance parameters for the system they studied. Successful applications of this technique can be seen, for instance in [Gal 00] or [Gom 01].

In spite of its advantages, the thick target technique has some limitations. For example, analyses like the one performed by Benjelloun are not valid if the inelastic channels are strongly populated. If no previous information is known about the system under study, the determination of excitation functions could be severely compromised by the presence of multiple reaction channels. An example of this is the system ^{7}Be+*p*, which was studied at Notre Dame using the thick target technique [Rog 01]. That study assumed that contributions from the inelastic channel were negligible, which led to the wrong conclusion that a predicted 1^{+} state in ^{8}B was non-existent. Recently, Livesay and collaborators demonstrated that the 1^{+} state does exist in a series of thin target experiments that showed that the contribution from inelastic scattering was indeed significant [Liv 06].

3.2.1.2 Beam Purity

In addition to the weak intensities of RIBs, ISOL facilities might not be able to produce RIBs of single nuclear species, depending on the chemistry of the element under consideration. Instead, RIBs are often produced as a mixture of nuclei that cannot be separated by conventional electromagnetic methods. As an example, at HRIBF some fission fragments from ^{nat}U with mass differences of less than one part in 15000 cannot be separated in the low energy mass analyzer, which results in isobaric cocktail beams where the relevant nuclei might not even be the most abundant species [Str 04]. In order to deal with this issue, a number of techniques have been developed to increase the relative yield of the isotopes of interest. These

include complete electronic stripping of light ions in the post-acceleration stage that enables the use of an analyzing magnet before delivering the beam into the experimental area [Gal 01], the use of specially designed ion sources [Str 03], and the use of chemical carriers that bond with ions of interest and facilitate their transport into the ion source [Hag 92], [Str 03]. In cases where a pure beam cannot be developed, care should be taken to continuously monitor the composition of the beam. This can be accomplished in a number of ways, including the identification of characteristic X-rays from ions in the beams and through the use of gas detectors that allow a distinction of the atomic number of the projectile based on its stopping power. A discussion of these techniques and their use in RIBs experiments can be found in [Pad 04] and references therein.

3.3.1.3 Large Background

Another issue in experiments with RIBs is the background originated by the decay of the radioactive beam. This effect can be particularly large for short lived beams and/or for implantation experiments (including reactions with thick targets where the beam is completely stopped inside the target). Even at typical RIB rates of 10^5pps, accumulation of short live ions eventually becomes a source of beta radiation, which has high penetrability and high ionization power. Such a source could produce spectra with large backgrounds and it also has the potential to saturate the electronics of the detection system. Among the strategies used to deal with this issue, one can find the use of moving targets and collection tapes, the use of active targets that provide a signal upon beam incidence that can be used as an electronic trigger, time of flight measurements that give rise to cleaner spectra, the use of coincidences, and the use of electromagnetic fields to deflect the decay products into one preferential direction [Eng 74a].

3.2.1.4 Inverse Kinematics

The detection schemes utilized in reactions induced by RIBs are sometimes radically different than those used in similar experiments with stable isotopes. This is not only related to new detection technologies, but to a rather more fundamental factor: most experiments with RIBs are performed in inverse kinematics, i.e., in such a way that the projectile is heavier than the target nucleus. Inverse kinematics has a profound impact on the detection geometry of each experiment. In general, particles emitted in the reactions tend to be strongly forward focused, which makes the use of large area detection arrays with high granularity desirable. A discussion on inverse kinematics can be found in appendix A.

In spite of the formidable challenges described here, the field of RIBs is significantly enhancing our understanding of the nuclear many-body problem [Gee 06]. So far, nuclear scientists have mainly focused

on conventional observables in reactions with RIBs: masses, decay parameters, energy levels, B(E2)'s, and transition rates. Although rapid progress has been made in all these fronts, the use of polarized probes remains practically unexplored. The motivation for their use in the context of RIBs constitutes the subject of the next section.

3.3 Nuclear Physics with Polarized Probes

Ranging from deuterium, the simplest nuclear system, to the superheavy elements, where shell effects are responsible for stabilizing nuclei against Coulomb repulsion, spin dependent interactions (spin-orbit and tensor interaction) are known to play a major role in the structure of atomic nuclei. Nowadays, experiments with RIBs give us the opportunity to explore the evolution of those effects with isospin. In principle, this could be best done through reactions where all the degrees of freedom are controlled independently. In particular, by controlling the spin degree of freedom in the entrance channel of a reaction, information on the scattering process and the final states is maximized. This point is illustrated here with selected examples where reactions have been performed with beams in well defined spin states.

3.3.1 Few Body Systems

The physics of few body systems at low energies is an area where polarization observables have driven a substantial amount of research [Car 98]. Due to the small number of particles involved in the lightest nuclei, these systems constitute a natural ground to test the validity of nucleon-nucleon interactions and three body forces. Nowadays, several phenomenological potentials including two and three body forces (e.g. AV18, CD-Bonn, Tucson-Melbourne, etc) can claim a remarkable success in predicting spectroscopic observables. In addition, effective field theories and the chiral perturbation approach are pushing further our understanding of systems up to A=4 [Bed 02]. However, in spite of all this, a satisfactory account of polarization observables in three body systems (n+d and p+d) at low energies remains elusive.

The first evidence that state of the art nucleon-nucleon interactions fail to predict the polarization observables in three body systems appeared more than twenty years ago. Back then, Koike and Haidenbauer [Koi 87] showed that although the Paris potential gave very accurate results for cross sections, it underestimated the analyzing power of the n-d elastic scattering between 6 and 20 MeV, as compared with high quality data measured earlier at TUNL [Tor 82]. Eventually, it became clear that this was a general problem for all NN potentials available in the market that not even the inclusion of three body interactions could remedy [Wit 94]. Figure 3.4 illustrates this long standing issue that, for obvious

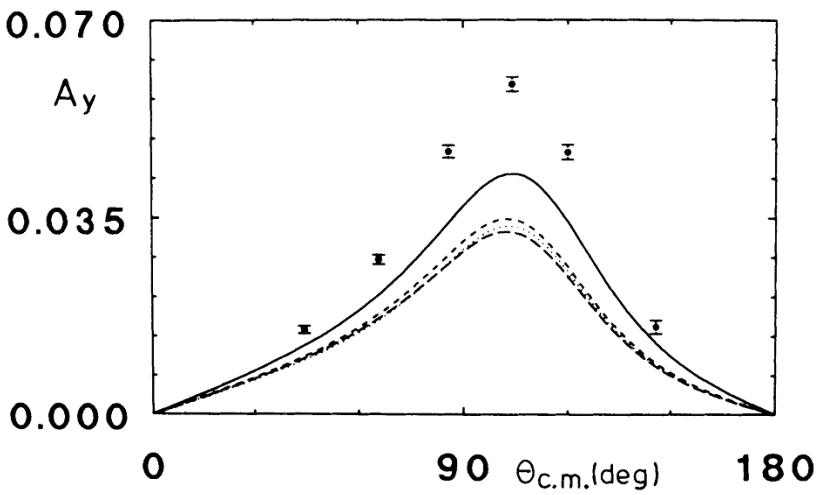

Figure 3.4. Measured and calculated analyzing powers for the *n-d* system at E_n=3.0 MeV. Full dots represent experimental data. The solid line is the prediction of the Bonn B potential alone, while the short-dashed, dotted, and long-dashed lines correspond to the Bonn B, Nijmegen, and Paris 2N interactions plus a 2-pion exchange force. The figure has been adapted from [Wit 94].

reasons, is known as the 'A_y puzzle'. In the mid-nineties, the A_y puzzle acquired a renewed interest as rigorous *p-d* calculations below the deuteron break-up threshold became a reality [Kie 95]. As a result, not only was the A_y puzzle confirmed for *p-d* scattering, but it was also found that a similar problem exists for the vector-analyzing power in *d-p* scattering, while the tensor-analyzing power data were described fairly well by theory.

The current status of the A_y puzzle is summarized in figure 3.5 (adapted from [Tor 08]). There, Tornow shows the relative difference between calculations and data for A_y in nucleon-deuteron scattering in the energy range between 650 keV and 35 MeV. For nucleon energies below 15 MeV, the relative difference was computed for the angular region of the A_y maximum using the AV18 potential, resulting in a rather constant energy dependence of the A_y puzzle. The point at 35 MeV indicates the well known fact that the A_y puzzle disappears at energies above ~35 MeV. But between ~18 MeV and ~30 MeV, the quantity plotted exhibits a behavior that is further obscured by the lack of experimental data in that energy range (in particular, above 24 MeV).

Interestingly, the Pisa group showed in 2001 that the four-nucleon scattering system also exhibits an A_y puzzle of its own [Viv 01]. Contrary to the 3N systems, where differences up to 25% were found between

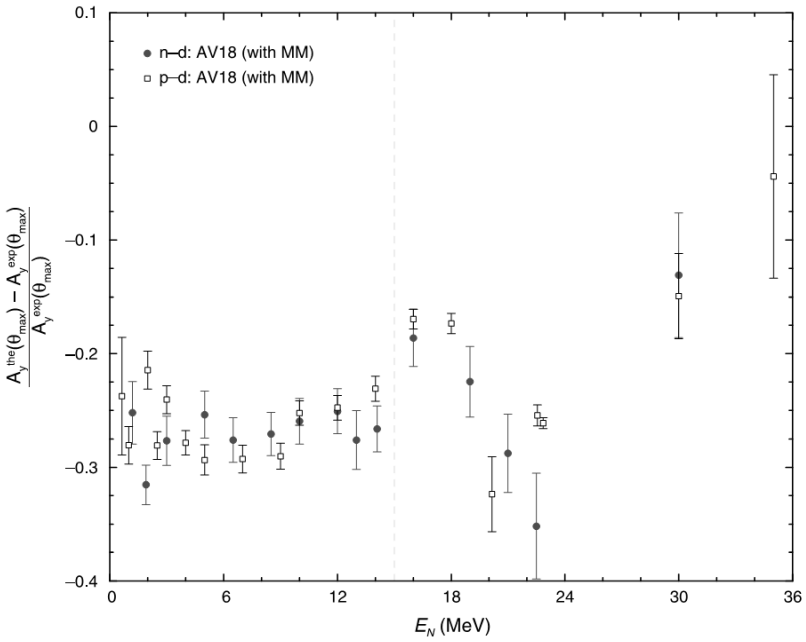

Figure 3.5. Relative differences between experimental data and calculations for the three nucleon system. The figure has been adapted from [Tor 08].

data and calculations, the discrepancies for A_y in elastic p-^{3}He scattering approach 40%. Recently, a complete, high precision set of n-^{3}He A_y data has been measured at TUNL using a polarized ^{3}He target [Tor 07]. Extending the existing sets of data for the p-t system will undoubtedly be useful to further explore the isospin dependence of the 4N A_y puzzle. Given the large quantities of tritium that would be needed to produce a target, the use of a (radioactive) beam of tritium could contribute to shed light on this issue.[4] Moreover, it is conceivable to extend the study of polarization observables to the light nuclear systems available in RIB facilities.

3.3.2 Elastic Scattering

I will describe four examples where polarization becomes an important tool in scattering experiments with heavy ions. For the first three, the main goal is to obtain unambiguous resonance parameters for nuclear structure studies and for reactions of astrophysical interest. For the last example, elastic scattering of ^{6}He and ^{8}He nuclei from polarized targets is proposed as a mechanism to investigate properties of these weakly bound systems.

[4] The use of large quantities of tritium faces inherent occupational and homeland security concerns.

Table 3.1. Resonance parameters for the 1.56 MeV excited state in ^{7}Be. Remarkably different widths are obtained when polarization data are included in the analysis of the phase shifts from the p+^{6}Li elastic scattering. No error bars are provided by McCray.

	Analysis of dσ/dΩ and A_y *Skill et al. (1995)*	Analysis of dσ/dΩ only *McCray (1963)*
E_R [MeV]	1.56±0.1	1.57
Γ [MeV]	0.4 ±0.05	0.84
Γ_p [MeV]	0.19±0.05	0.8

The power of polarized probes is illustrated in the study of isolated resonances with the example of elastic scattering of protons by ^{6}Li. This reaction has been used to study the level structure of ^{7}Be and to test different theoretical models ([Kan 95] and references therein). Experiments in the early sixties [Mcc 63] demonstrated the existence of a resonant state at 7.45 MeV in ^{7}Be (1.56 MeV in the c.m.). A tentative spin and parity assignment of I=5/2^{-} was made based on the angular distributions of cross sections at energies between 0.45 MeV and 3.6 MeV. The parameters of that resonance were determined using a phase shift analysis of the excitation function. Later, Skill *et al*. [Ski 95] investigated the same reaction using polarized proton beams with energies between 0.4 MeV and 3.2 MeV. Cross sections and analyzing powers were measured and both were included in the phase shift analysis used to determine resonance parameters for the $E_{c.m.}$=1.56 MeV state. Table 3.1 compares their results along with those of McCray. Notice that although the energy of the resonance is the same in both studies, there is a large difference in the widths of the resonance: the total width estimated from the cross section data alone in [Mcc 63] is two times that of the estimate made taking into account the polarization measurement, while the difference in the partial widths is a factor of four.

Another case where the use of polarization might be important is the reaction ^{7}Be(p,γ)^{8}B, which is one of the most important in nuclear astrophysics: It is responsible for the production of ^{8}B, the main source of high-energy solar neutrinos. The Gamow window for such reaction is centered around 20 keV, which makes a direct measurement of the reaction rate at solar energies extremely difficult. As a consequence, determinations of the S-factor have been based on theoretical extrapolations from data at higher energies, which calls for a precise knowledge of the structure of ^{8}B [Ade 98] [Nav 06]. A substantial amount of

work has been devoted to that end. However, until now only four states in ^{8}B have been unambiguously identified [Til 04]. The study of resonances in the ^{7}Be+*p* system is an important step towards a deeper understanding of the nuclear structure of ^{8}B. Recently beams of ^{7}Be have been used to study resonant scattering covering the energy range between 0.3-3.5 MeV obtaining controversial results for states above 1 MeV [Rog 01], [Ang 03], [Liv 06]. For example, using the thick-target technique Rogachev *et al*. [Rog 01] measured an excitation function of cross sections between 1 and 3.3 MeV. They claim that a 2^{-} state at 3.5 MeV is needed to fit their data and estimate a width Γ = 8±4 MeV for that resonance. However, Angulo et al. [Ang 03] performed an R-matrix analysis of their own data that is numerically consistent with a resonance at E =3 MeV and Γ = 7 MeV but find no physical meaning whatsoever for it. A second important point in the study of Rogachev is the lack of evidence for a 1^{+} state at ~1.4 MeV which has been predicted by numerous theoretical calculations, including ab initio no-core shell model [Nav 06] and recoil-corrected continuum shell model [Hal 04] calculations and that was recently observed by Livesay in experiments at HRIBF [Liv 06]. Finally, a 1^{+} resonance at 3.8 MeV cannot be confirmed or rejected based only on the excitation function obtained in [Rog 01]. Clearly a more constrained data set is needed in order to extract definitive conclusions. In this regard, the determination of spin observables, such as analyzing powers, becomes important. Figure 3.6 shows the calculated excitation function of the analyzing power for ^{7}Be+*p* in the range of interest according to [Hal 04]. The predicted behavior shows a strong variation of A_y with energy. A phase-shift analysis of elastic differential cross section and analyzing power A_y will allow a better estimate of the resonance parameters as has proved to be the case with other systems. The measurement of low energy reactions of importance to nuclear astrophysics is one of the main objectives of the physics programs of the existing radioactive ion beam facilities.

The second example of the potential use of polarized probes in elastic scattering experiments with RIBs is concerned with a series of radiative proton and helium capture reactions involving short lived isotopes that are key reactions in the hot-CNO cycle. An astrophysical problem that has recently received considerable attention is related to the ^{18}F abundance in novae. Information about nucleosynthesis and the understanding of the ejection mechanism in novae can be determined from the γ-ray emission coming predominantly from the electron-positron annihilation at 511 keV following the β^{+} decay of ^{18}F ($t_{1/2}$ = 110 min.). It is believed that this relatively long decay is responsible for the majority of γ-rays during the first hours after the explosion.

The destruction of ^{18}F in novae is determined primarily by the reaction ^{18}F(p,α)^{15}O and to a lesser extent by the ^{18}F(p,γ)^{19}Ne reaction. Related relevant properties of ^{19}Ne states are being studied with a series of

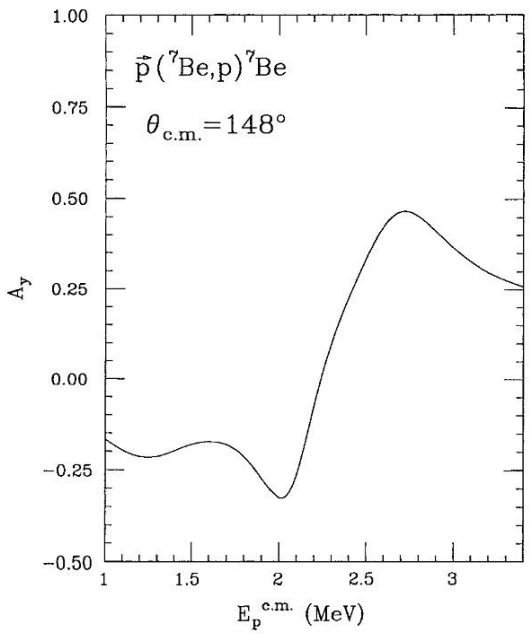

Figure 3.6. Calculated analyzing power for elastic scattering of polarized protons by ^{7}Be (adapted from [Hal 04]).

experiments such as (*p*, *p*) elastic scattering and transfer reactions with stable and radioactive ion beams to populate levels in ^{19}Ne or in the mirror nucleus ^{19}F [Koz 05]. Many uncertainties still remain on the reaction rates and on the detailed properties of the resonances involved. Customarily, the astrophysical S-factors are calculated as a sum of contributions of individual states. However, recently Chae and collaborators have drawn attention to possible interference effects among $3/2^+$ resonances and their effect on excitation functions of cross sections for the ^{18}F(*p*,α)^{15}O reaction [Cha 06]. Furthermore, a microscopic approach has been applied in the study of this reaction [Duf 07]. The authors assume a cluster structure for the nucleus and define the wave functions in a Generator Coordinate Method. They show that the $1/2^+$ partial wave plays an important role in a wide range of energy. They predict new $1/2^+$ states near the proton threshold for ^{19}Ne that could be observed in elastic scattering experiments. The access to polarization observables could help elucidate these issues.

A third case of interest in elastic scattering involving RIBs and polarized protons is the investigation of weakly bound nuclei. For those systems, states in the continuum are expected to play a major role in describing scattering processes. Recently, the first experiment using a polarized proton target was performed at RIKEN, resulting in measurements of the analyzing power of the ^{6}He + *p* elastic scattering

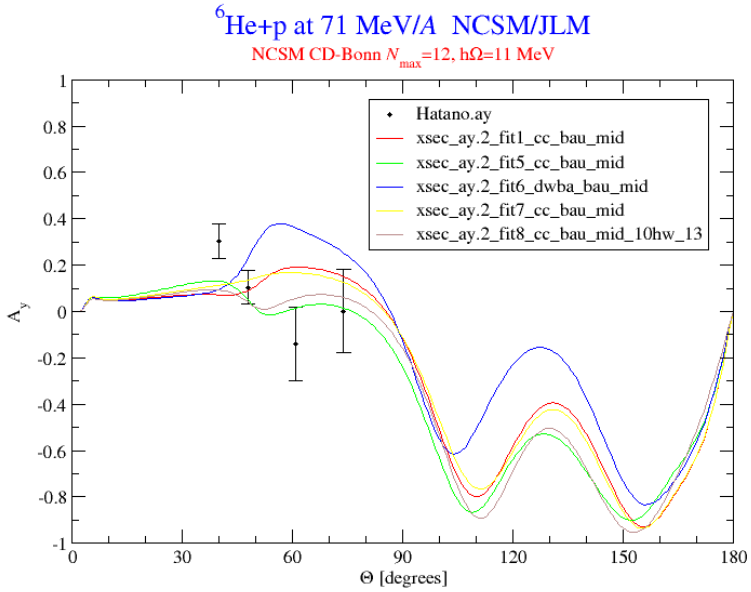

Figure 3.7. Analyzing power of the $\vec{p}\left(^6He,^6He\right)p$ reaction at 71 MeV/A. The dots correspond to the experimental data reported by Hatano [Hat 05], while the curves correspond to NCSM/JLM calculations. The blue curve was obtained using a DWBA calculation (direct reaction), while the others were obtained by including the first 2^+ excited state of ^{6}He in coupled channels calculations with different parametrizations of the JLM optical potential [Jeu 77]. This figure has been provided by [Nav 05].

at a beam energy of 71A MeV [Hat 05]. Striking differences were observed for the measured analyzing powers A_y between the scattering of ^{6}He + p and ^{6}Li + p [Hen 94]. By contrast, the differential elastic-scattering angular distributions are almost identical. A change in A_y from positive to negative values was observed for ^{6}He + p while a rapid increase of positive A_y values is observed for ^{6}Li + p for the same angular range. Although different theoretical efforts fail to reproduce this behavior [Wep 00], [Gup 00], P. Navratil noticed that a two step process is required in order to correctly predict the sign of A_y reported by Hatano and his collaborators [Nav 05]. Figure 3.7 shows the data taken by Hatano, along with the no core shell model/JLM calculations from Navratil for the analyzing power of the reaction $\vec{p}\left(^6He,^6He\right)p$. Although all the calculations are able to reproduce the cross section for the reaction, only coupled channels calculations including the first 2^+ excited state of ^{6}He can alter the sign of the analyzing power. Unfortunately, a calibration for the target polarization was not performed during the experiment and the estimated value of the polarization relies on a best guess. More recently S. Sakaguchi reported at the DREB2007 conference an average polarization of 13.8% for the RIKEN target [Sak 07], but the resulting error bars are too large to define the sign of A_y. Clearly, this peculiar behavior of A_y for ^{6}He + p, if

confirmed, represents a theoretical challenge.

3.3.3 One Nucleon Transfer Reactions

The assignment of spin and parities to nuclear levels is one of the main goals of nuclear spectroscopy. It is through these assignments that we can arrive at a view of nuclear level structure and test the predictions of various model calculations. Transfer reactions with stable light-ion beams are important tools to extract information about the spins and parities of nuclei resulting from reactions with targets of stable or long-lived isotopes. With the availability of high quality, intense RIBs it will be possible to perform transfer reactions in inverse kinematics allowing us to study nuclei away from the valley of stability and to map out single-particle properties, searching for changes in shell structure and evidence of the onset of deformation. The selectivity of nucleon transfer for mapping out the single particle structure of nuclei complements other processes (e.g. CoulEx) that probe collective aspects. The first (*d,p*) experiment on a shortlived beam was done in inverse kinematics on ^{56}Ni, confirming the single-particle structure [Reh 98]. Reviews of experimental challenges associated with transfer reactions in inverse kinematics with RIBs can be found in [Win 97] and [Cat 02].

Transfer reactions with polarized probes are sensitive to the angular momentum of the transferred nucleon l_n and the total angular momentum j. Using the formalism of irreducible operators described in chapter 2, Satchler [Sat 64] showed that if no spin-dependent distortions are considered in the Distorted Wave Born Approximation (DWBA) formalism, then the predicted vector analyzing powers $iT_{11}(\theta)$ for reactions involving polarized deuterons are opposite in sign for $j = l_n + ½$ and for $j = l_n - ½$, and satisfy, at least semi-quantitatively, the relation:

$$\frac{\left[iT_{11}(\theta)\right]_{j=l_n+1/2}}{\left[iT_{11}(\theta)\right]_{j=l_n-1/2}} = -\frac{l_n}{l_n+1}. \qquad (3.1)$$

The striking j-dependence of the vector analyzing powers provides a mechanism to assign spins in an unambiguous way. The determination of the transferred j in one-nucleon transfer reactions in inverse kinematics with RIBs can become an important spectroscopic tool. For example in a stripping reaction a single-particle excitation is formed when a nucleus captures a nucleon in a definite shell-model orbit *nlj* in a reaction such as (*d,p*), (^{3}He,*d*) or (*n,γ*). From angular distributions in (*d,p*) it has been possible to assign orbital angular momentum *l*.

For the existing facilities that use the ISOL method, the majority of the RIBs available are on the neutron rich side. Of considerable interest is the development of RIBs in the region centered on the doubly magic

nucleus ^{132}Sn. To study the potential use of a polarized target in the study of single-particle properties of nuclei in this region using transfer reactions with RIBs, we chose an existing good-quality data set for a transfer reaction, namely $^{118}Sn\left(\vec{d},t\right)^{117}Sn$ [Vig 75]. This pickup reaction is particularly relevant since it was done at a low bombarding energy (6A·MeV), it involved a "fission-fragment like" nucleus (^{118}Sn), and angular distributions for cross sections and analyzing powers were measured for various excited states. We performed distorted wave Born Approximation (DWBA) calculations with the code DWUCK4 [Kun 00] and compared them with the published data showing good agreement with the experiment. The good quality data allows assignment of the nuclear spin values of a few states based on the cross sections alone. However, for other states this is not possible as the shape of the angular distributions for the final states with different j is very similar. Figure 3.8 shows an example where the experimental data falls between the calculated curves for the two allowed values in spin for the residual nucleus. By contrast, the sensitivity of the analyzing powers to the spin of the residual nucleus is remarkable. For the excited states of interest it is possible to unambiguously assign the nuclear spin based on the agreement between the experimental and the calculated analyzing powers. Firstly, the polarization measurements involve determinations of only ratios of cross sections, and are therefore free of the normalization problems encountered in making absolute cross-section measurements. Secondly, a change of sign is predicted for the analyzing powers. By judicious choice one can locate detectors in the region of maximum sensitivity. There is no need to measure detailed features of the angular distribution; the measurement of only a sign of an asymmetry suffices to make the spin assignment. This is very significant in experiments involving RIBs in inverse kinematics with a polarized target, where low statistics are expected. A sensitive observable, such as the analyzing power, could be a powerful tool for spectroscopic purposes even if the resulting error bars are relatively large and/or if only a restricted angular coverage for the recoiling particles is possible.

Since the maximum energy that can be obtained at HRIBF for a fission fragment is about 5A MeV, we investigated the effect of the bombarding energy on the angular distributions of both cross sections and analyzing powers for the $^{118}Sn\left(\vec{d},t\right)^{117}Sn$ reaction [Urr 05]. Figure 3.9 shows the analyzing power angular distributions for two hypothetical states of ^{117}Sn at an excitation energy of 1.18 MeV calculated for bombarding energies between 4A MeV and 8A MeV. We observe that while the cross sections are smaller the sensitivity of A_y to the final state increases at low energies.

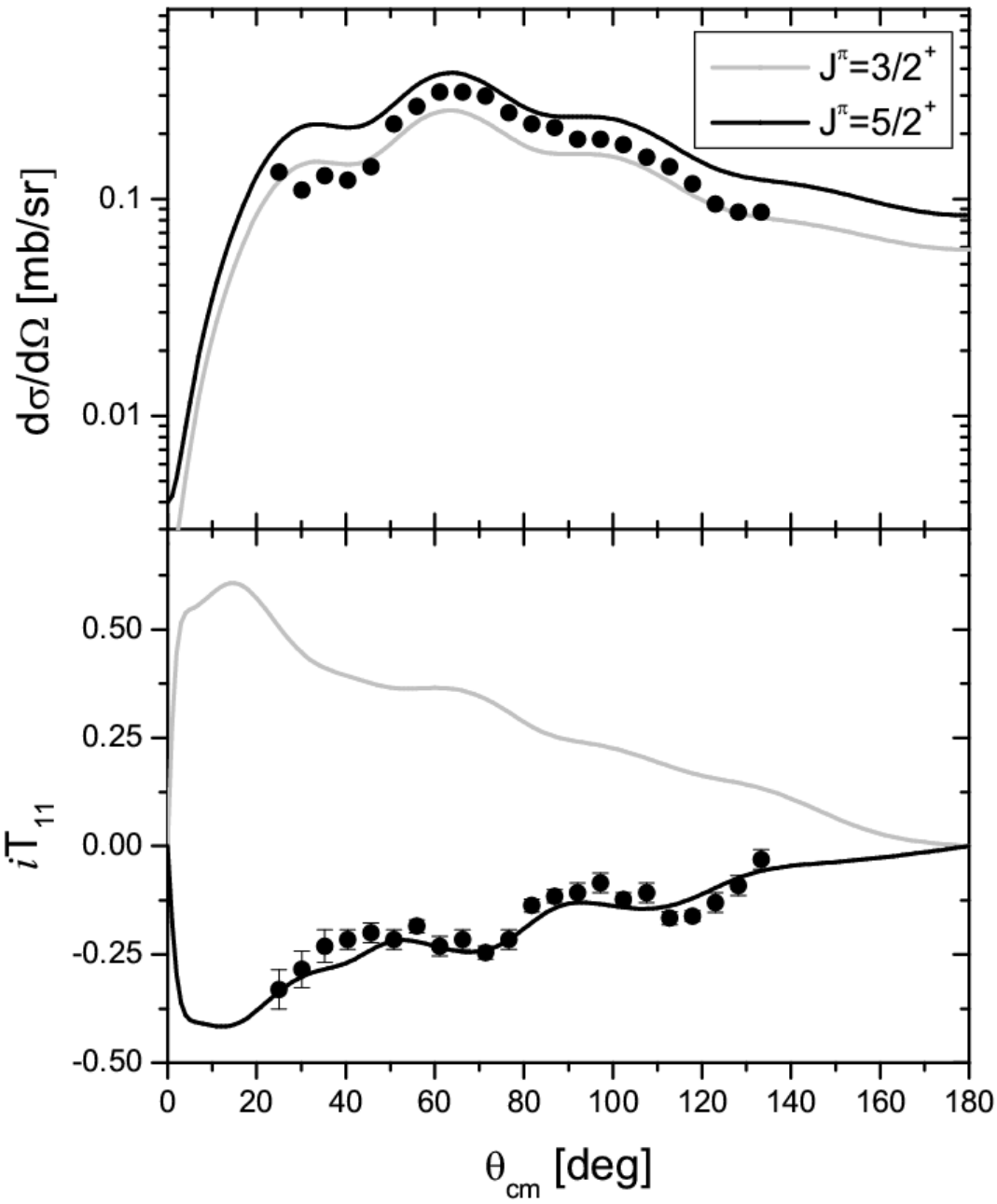

Figure 3.8. Spin dependent observables in a transfer reaction involving a fission fragment-like nucleus. The top panel shows the differential cross section for an excited state (E_x=1.18 MeV) populated in the reaction $^{118}Sn\left(\vec{d},t\right)^{117}Sn$, while the bottom panel shows the vector analyzing power (in spherical representation). The dots represent experimental data extracted from [Vig 75], while the lines correspond to DWBA calculations for two allowed values in spin for the residual nucleus. The parameters associated with the potentials were extracted from [Vig 75].

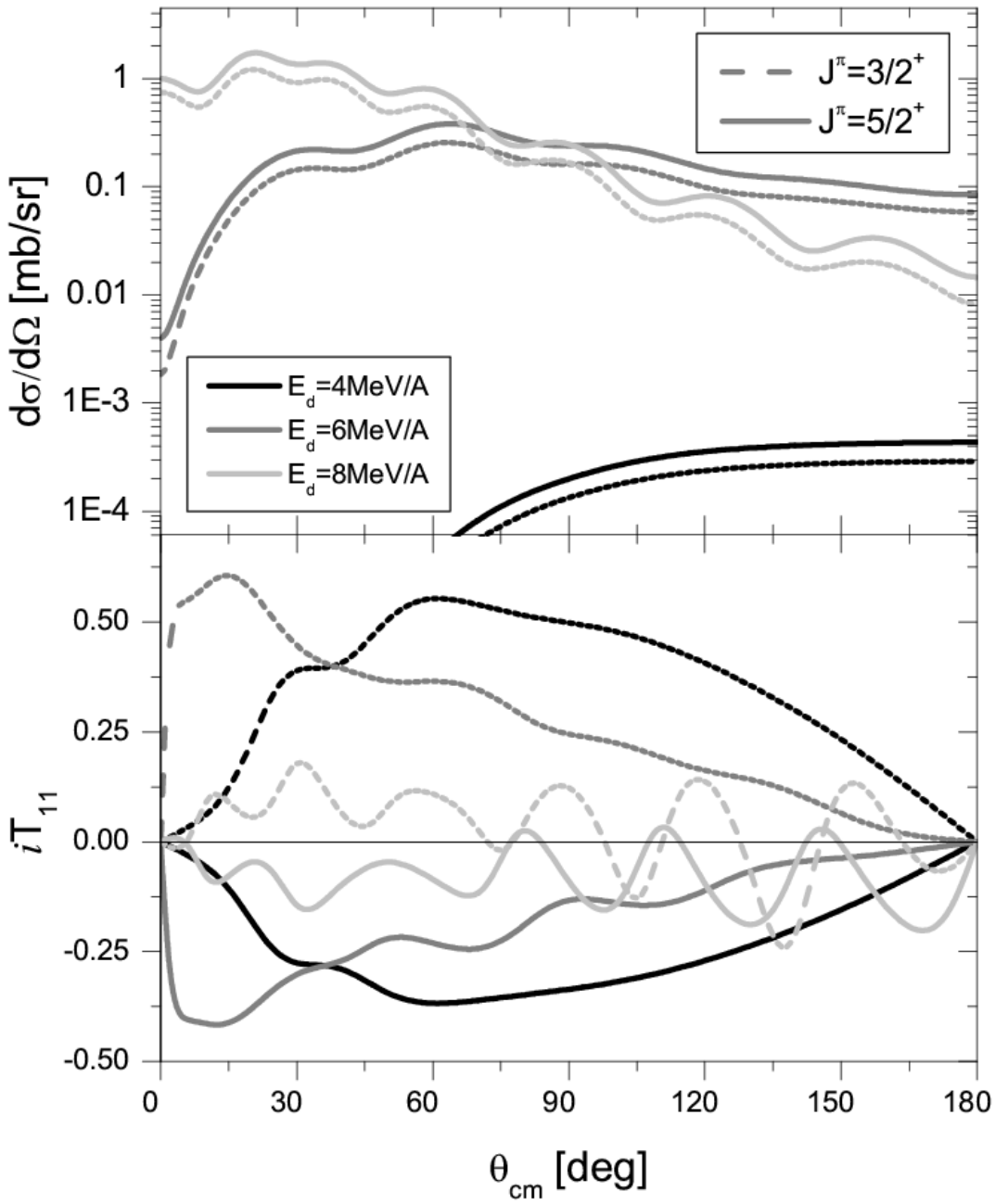

Figure 3.9. Energy dependence of the differential cross section and vector analyzing power for two hypothetical states of ^{117}Sn at an excitation energy of 1.18 MeV. The curves correspond to DWBA calculations for the two allowed values of spin for the residual nucleus. The parameters associated with the potentials used to calculate the pseudodata were taken from [Vig 75].

For transfer reactions with RIBs, a polarized target will be a very useful tool to make spin assignments. One-nucleon transfer reactions directly probe the single-particle nature of nuclear states and will allow us to address the question of how the single-particle structure changes with isospin asymmetry.

3.3.4 Reaction Mechanisms

In chapter 2 it was shown that polarization observables are sensitive to interference between various nuclear transition amplitudes. Therefore, the determination of analyzing powers can provide a clear signature for the interference between different reaction mechanisms. An example is given by the angular distributions measured for two nucleon transfer reactions induced by polarized protons and populating nuclei in the N=50-82 shell [Yag 78]. These investigations performed in Tsukuba show the critical role of nuclear structure in the scattering process: as neutrons are added into the system a gradual change in analyzing power is observed for reactions populating the first 2^+ excited state. This effect can be seen in figure 3.10, where the analyzing power for residual nuclei with N=62 and N=74 is illustrated for both the ground and the 2_1^+ excited state. Whereas the analyzing powers for the reactions populating the ground state are quite similar, a profound difference exists between the reactions populating the excited state. Based on microscopic analysis of the structure of the states involved in the reactions, the authors of the study were able to interpret the change in the sign of the analyzing power for the upper shell nuclei in terms of a two-step reaction, arising as a consequence of the neutron number dependence of the occupation probability of single particle orbits and that of ground state correlations with collective oscillations of nuclei. Such type of studies might be valuable in investigations of the dynamics of nuclear reactions as a function of isospin and in the assessment of the onset of deformation and shape coexistence in transitional regions such as N=40—N=50 and the neighborhood of ^{132}Sn.

In conclusion, I have shown that the use of polarized probes in nuclear reactions provides valuable elements to the comprehensive understanding of atomic nuclei. Extending their use to reactions induced by RIBs will undoubtedly push it further away, perhaps through the discovery of new phenomena, through the use of polarization observables as powerful spectroscopic tools, or through the use of cross sections and analyzing powers as benchmarks for new theories.

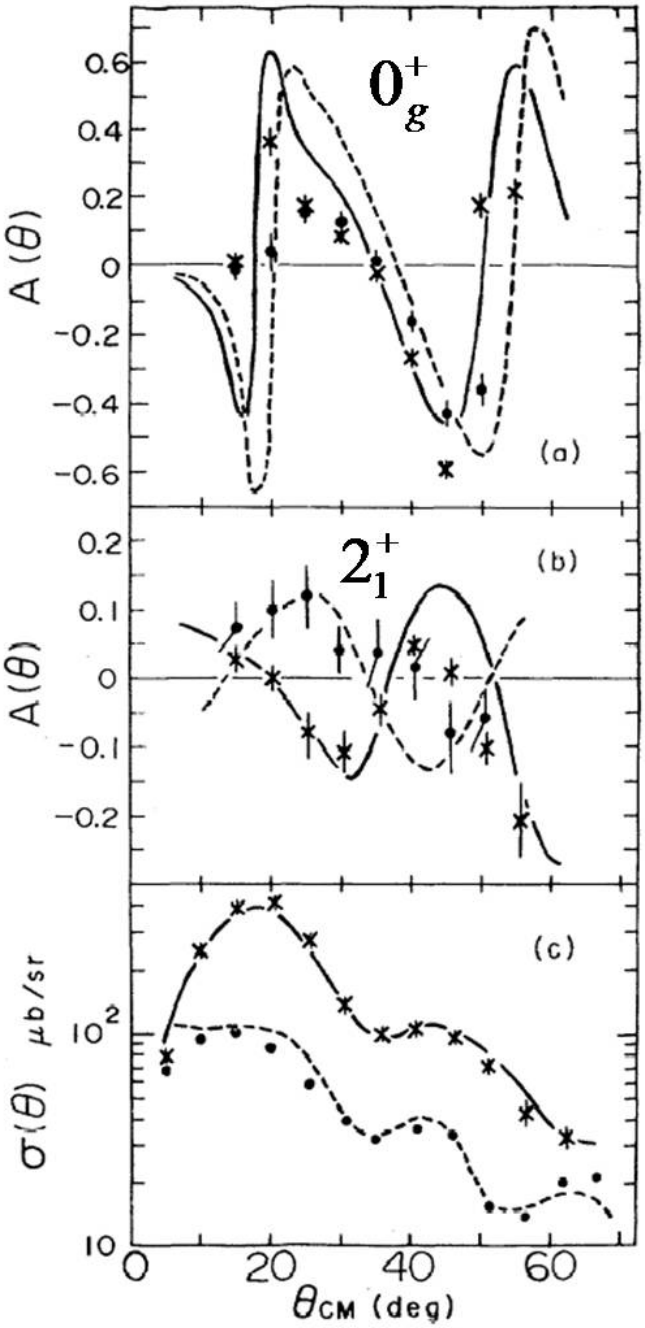

Figure 3.10. Experimental and calculated analyzing powers (*a*), (*b*) and cross sections (*c*) for the reactions $^{128}Te(\vec{p},t)^{126}Te$ (crosses) and $^{110}Pd(\vec{p},t)^{108}Pd$ (circles) at E_p=23.0 MeV. The solid (dashed) curves are coupled channels Born approximation calculations for the first (second) reaction. Figure adapted from [Yag 78].

CHAPTER 4

Spin Polarized Target for Reactions with RIBs

4.1 Introduction

The core of this thesis is to find a suitable way to use polarization observables in reactions with RIBs. This chapter and the next one describe the approach taken to address this matter, the technical challenges that were encountered, and the results obtained during the development of a polarized target.

I begin by exploring the technological choices available for polarized targets and briefly describe their advantages and disadvantages in terms of their potential use with RIBs. Then, in section 4.3, there is a short discussion about the physical principles behind Dynamic Nuclear Polarization (DNP), the method of choice for the target. I conclude that section by describing two different types of targets that can be implemented using DNP. Section 4.4 contains a detailed description of the target that closes with an account of its performance in off-line laboratory tests.

4.2 Overview of Polarized Target Technologies

Ranging from high energy physics to condensed matter, polarized targets have been the key leading to fundamental insights in spin-dependent phenomena [Cra 09]. The first reported nuclear physics experiment involving a polarized target dates back to 1955, when ^{115}In was polarized and bombarded with neutrons at Oak Ridge National Laboratory [Dab 55]. A few years later, the development of more universal targets became a reality. In 1962, Abragam and his collaborators at Saclay reported the first experiment using a polarized proton target [Abr 62]. Since then, much progress has been made in terms of polarizable materials and target technology, but to this day, the essential mechanisms of polarization remain the same [Ues 07a]. Nevertheless, polarized targets can not be considered, by any means, typical tools in a nuclear physics laboratory: They are designed and built for very specific classes of experiments. The potential use of polarized targets in RIB experiments has its own challenges, the most significant being the large density of polarized nuclei required and the minimization of the amount of materials

surrounding the target. The first constraint is imposed by the typically low RIB intensities available, whereas the second has to do with the high ionizing power of heavy ions. In this thesis we have designed and built a polarized target that can be used at low and intermediate energies.

There are several methods to achieve sizable polarizations in an assembly of nuclei, but only a few of them are suitable for the desired targets. The method of choice depends on whether the polarized target is a gas or a solid. Gas targets are typically used in electron and neutron scattering, while most solid targets are used in hadronic reactions at high energies. In the following paragraphs I will briefly mention the main features of each method, but the interested reader might find thorough discussions in any of the proceeding volumes of the SPIN conference, in the Polarized Sources and Targets conference proceedings, or in specialized reviews in [Bra 92], [Chu 94], and [Cra 97].

4.2.1 Gas Targets

Gas targets can be roughly separated into internal targets and spin-exchange targets. A typical internal target includes a source of polarized particles, normally hydrogen or deuterium, and a windowless storage cell where the polarized nuclei dwell inside the beam line. Since nuclei come from an atomic source, polarizations above 90% can be routinely achieved and rapidly reversed [Cou 94, Rat 93], plus the purity of the targets is very high. In addition, the absence of windows favors the detection of recoils at very forward angles, which is required in inverse kinematics reactions. Unfortunately, practical limits on the flux of polarized particles from atomic sources, finite dwelling times in the storage cell, and depolarization effects on the walls of the cell, impose strong constraints on the number of target nuclei that can be achieved. To the best of my knowledge, up to this point, the internal target with the highest density of polarized protons has been developed at Argonne National Laboratory, reaching $4*10^{14}$nuclei/cm^2 [Jon 93]. Because of their design, these targets are best suited for proton or electron rings. The low luminosity obtained when combining these targets with current RIB intensities (~10^7 pps in best case scenarios) would make them rather impractical for the nuclear physics studies that have been mentioned in previous chapters.

Spin-exchange targets are a good alternative to obtain high luminosities with gas targets (particularly for ^{3}He). This type of targets involves optical pumping of one atomic species (an alkali-metal or metastable ^{3}He) with a subsequent polarization transfer to a second species via spin exchange collisions. In 1960, it was shown that angular momentum could indeed be transferred from the electron spins of optically pumped Rb atoms to the nuclear spins of ^{3}He [Bou 60]. In that case, Rb atoms are pumped via the

electronic transitions $S_{1/2} - P_{1/2}$ (795.0 nm) and $S_{1/2} - P_{3/2}$ (780.2 nm). In a relatively weak magnetic field (typically tens of Gauss), the former transition can be driven by circularly polarized laser light (795 nm) to selectively pump the ground-state Rb electrons entirely to the +½ (or −½) state. The electronic polarization of the optically pumped Rb atoms is transferred to the nuclei of the noble gas atoms via formation of loosely bound van der Waals molecules or via binary collisions. The method has been extended to efficiently polarize hydrogen isotopes [Cou 92] and even noble gases nuclei, such as ^{129}Xe of interest for medical applications [Gro 78]. Equilibrium polarization of the nuclei of interest is reached after establishing a balance between the cross section for spin exchange collisions and depolarization effects such as collision with the walls of the target cell, magnetic field gradients, or beam ionization. In the best cases reported in the literature, polarizations of up to 85% have been reached for ^{3}He and ~80% for protons [Chu 94]. The effective thickness is however, dramatically different: ~10^{21}nuclei/cm^2 for ^{3}He and ~10^{15}nuclei/cm^2 for hydrogen isotopes. Therefore, among the spin exchange targets, only ^{3}He targets might be appropriate for reactions with RIBs [Kat 05].

4.2.2. Solid Targets

In contrast to gas targets, solid targets do have a high density of scattering centers, which makes them attractive for experiments at low beam intensities. Solid polarized proton and deuterium targets are widely used in medium and high energy physics. Targets with thicknesses ranging from a few mm to 60 cm have been used [Cra 97]. Factors to be taken into account when selecting a solid target include the intensity of the beam, the ionization power of the projectiles and the radiation damage to the target material.

Basically two different approaches are used in achieving high nuclear polarization in hydrogen targets: the thermal equilibrium polarization or ‘‘brute force’’ method and the dynamical nuclear polarization (DNP) method [Dan 65]. All of them use the fact that the magnetic states of a quantum mechanical system can be separated by the action of an external magnetic field. If the imbalance in the population of the Zeeman levels of an assembly of spins can be maintained over a period of time long enough for an experiment to take place, then one has succeeded in producing a polarized system.

4.2.2.1. “Brute Force” Targets

Conceptually, the “brute force” or static method is the simplest polarization method existing for solid targets, but the long polarization times involved often make it impractical to use. It consists in placing the target in an intense magnetic field $\boldsymbol{B}$ and cooling it down to a temperature T, such that thermal lattice excitations become smaller than the separation between Zeeman levels in the nuclei of interest. After

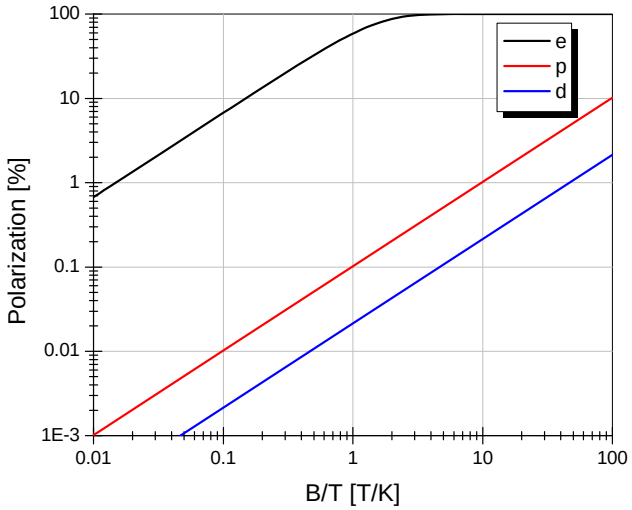

Figure 4.1. Thermal equilibrium polarization as a function of the magnetic field to temperature ratio. The large difference between protons and electrons is due to their different magnetic moments (μ_e/μ_p=658.21).

reaching thermal equilibrium, the imbalance in the population of the magnetic states gives rise to a net polarization P of nuclei of spin I and magnetic moment μ, which is given by the Langevin-Brillouin function:

$$P = \frac{2I+1}{2I}\coth\left(\frac{2I+1}{2}\frac{\mu B}{kT}\right) - \frac{1}{2I}\coth\left(\frac{\mu B}{2kT}\right). \tag{4.1}$$

For the case of spin ½ particles, such expression reduces to

$$P = \tanh\left(\frac{\mu B}{2kT}\right). \tag{4.2}$$

Figure 4.1 shows the predicted level of polarization for electrons, protons and deuterium. It can be seen that extreme field to temperature ratios are required to produce sizeable polarizations in nuclear species: At a temperature of 1 K, a magnetic field of 10 T would be required to produce proton polarizations slightly above 1%. The modest polarization values and the extraordinarily challenging combination of very large magnetic fields with very low temperatures, makes it impractical to use this method for building universal targets for experiments with RIBs.

4.2.2.2. DNP Targets

Dynamic Nuclear Polarization (DNP) methods are the alternatives to static methods of polarization in solids. As the spin-exchange gas targets, they also require the two basic steps of building up electronic or atomic polarization and then transfer it to the nearby nuclei. Several physical processes might be distinguished, namely the Overhauser effect [Ove 55], the differential solid effect, the solid effect, and the thermal mixing effect [Abr 78]. For simplicity we will briefly discuss the last two in the next section, but a good source of information on the physics addressed by all these effects can be found in [Dan 65].

There are at least two methods to build up the initial electronic polarization: optical pumping and the 'brute force' method. As it turns out, both of these methods can be implemented in a target for reactions with heavy ions. The first method has been followed by the CNS-RIKEN group [Hat 05] [Ues 07], while we have followed the second approach [Urr 05] [Urr 07]. Before explaining in detail our method, I will mention here the main features of the Japanese target.

The CNS-RIKEN target is polarized upon optical pumping of molecular triplet states in pentacene [Hen 90]. A complete description of this system can be found in [Wak 05]. The target itself consists of a 1 mm thick crystal of naphthalene doped with ~0.01% pentacene. Optical pumping is done with an Ar ion laser at ~100 K and in a magnetic field of ~900 G. The maximum polarization reported in off-line tests is 37% at 3 kG. However, once the beam hits the target, the polarization drops down to ~13%. In addition to the high density of nuclei in the material, this target has two great advantages: the temperature of operation is relatively high (no complex cryogenic equipment is required) and the magnetic field is rather weak, which results in an almost negligible influence in the trajectories of the particles from reactions at intermediate energies [Ues 07]. However, its large thickness is a disadvantage for the performance of this target at low energies. Protons with energies below 8 MeV are stopped by a 1 mm naphthalene crystal, which makes the target impractical for low energy studies.

In contrast with the CNS-RIKEN target, our target requires the use of low temperatures and high magnetic fields. The target is made of a plastic, a material that exhibits a satisfactory performance when used as a target in reactions with RIBs [Hue 98] [Gom 01]. Based on previous experience at PSI [Bra 00], we chose polystyrene, which has a proton filling factor of 0.5 as the target material. The plastic is doped with the free radical TEMPO [Roz 70], [Bun 04], which at 1 K and 2.5 T acquires a polarization close to 100%. Afterwards, microwave irradiation at ~70 GHz transfers the polarization to the protons. The physics foundations of this technique are given in the next section.

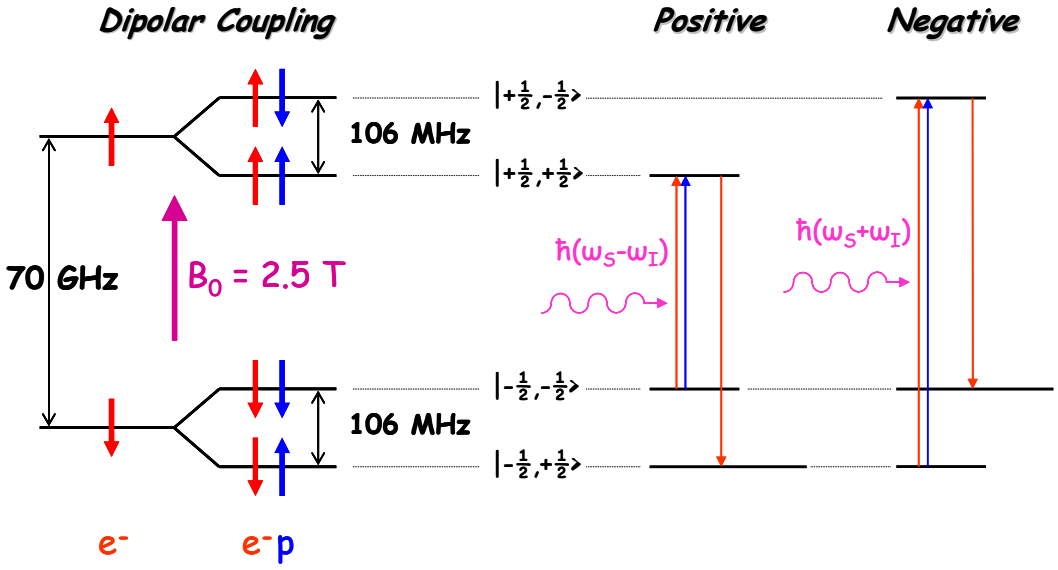

Figure 4.2. Schematics of the solid effect. At high magnetic fields and low temperatures, microwave irradiation around the ESR frequency can induce flip-flips ($\Omega=\omega_S-\omega_I$) or flip-flops ($\Omega=\omega_S+\omega_I$) in order to obtain positive or negative proton polarizations respectively.

4.3 Principle of Operation of the Polarized Target

The fundamentals of the DNP process can be better understood by considering the solid effect, discovered by Abragam in the fifties [Abr 55], [Abr 58]. It is based on the fact that electronic Zeeman levels of unpaired electrons in a dielectric are coupled to nuclear spins by the hyperfine interaction. Consider a free electron with spin S=½ surrounded by protons of spin I=½ in the presence of an external magnetic field B at temperature T. The energy of a given electron-proton pair is determined, to a first approximation, by a Hamiltonian H that considers only the magnetic interaction with neighboring particles:

$$H = \hbar\gamma_S \vec{S}\cdot\vec{B} + \hbar\gamma_I \vec{I}\cdot\vec{B} + \hbar\gamma_I\gamma_S \frac{\vec{I}\cdot\vec{S} - 3\left(\vec{I}\cdot\hat{n}\right)\left(\vec{S}\cdot\hat{n}\right)}{r^3}. \qquad (4.3)$$

The first term is dominant and corresponds to the Zeeman energy of the electrons, the second term gives the Zeeman energy of the protons, and the third term is the dipolar interaction between proton and electron. By virtue of this Hamiltonian, the pure electronic Zeeman levels are split as schematically shown in figure 4.2. The starting point of the polarization process requires values of B and T such that the electronic spins are almost fully polarized but the nuclear spins are almost completely unpolarized.

The dipolar interaction between electrons and protons in (4.3) permits simultaneous reversals of $\vec{S}$ and $\vec{I}$. For a given electron–proton pair, if the spins are reversed in opposite directions the reversal is called a flip-flop, whereas if the reversal occurs in the same direction for both spins it is called a flip-flip. At first order, the total energy of the spin system changes in such reversals by an amount $\cong(\omega_S \pm \omega_I)$, where $\omega_{S(I)}$ corresponds to the Larmor frequency of the electron (proton). Evidently, reversals will not occur unless this missing energy is supplied by the lattice, usually in the form of one or several phonons. As a matter of fact, those simultaneous reversals are responsible for the classical mechanism of nuclear relaxation by paramagnetic impurities [Abr82].

The rate of these processes can be very small at low temperatures ($10^{-3}s^{-1}$ is a typical value for the rate of proton relaxation in polarized target materials). On the other hand, the reversal of an electronic spin alone caused by its coupling to the lattice occurs at a much faster rate ($\sim 10^{3}s^{-1}$).

Suppose now that an external source of microwave energy at a frequency $\Omega=\omega_S \pm \omega_I$ is capable of inducing either flip-flops ($\Omega=\omega_S+\omega_I$) or flip-flips ($\Omega=\omega_S-\omega_I$). Assume also that the electronic line width $\Delta\omega_S$ is much smaller than the nuclear frequency ω_I, so that when flip-flops occur, flip-flips are impossible because they are off-resonance with the driving frequency Ω and vice-versa. In this picture, the nuclear relaxation process becomes allowed through the dipolar interaction that mixes the electronic and nuclear states. Assume then that forced flip-flips are driven and that the strength of the source is such that the rate at which they occur is much greater than the proton relaxation rate. As will be explained next, in this way it is possible to force "up" all the spins *I*.

Consider first a spin *I* that is up. The spins *S* being all down, transitions from the spin *I* are forbidden as they would be off-resonance. On the other hand, a spin *I* that is down may do a flip-flip with a spin *S* that is down, ending in a situation where both *I* and *S* are up. This spin *S*, which has come up, becomes perilous for all the spins *I* that are up, since it could bring one of them down through a forced flip-flip. Fortunately, before any harm is done, its powerful relaxation mechanism will have brought this spin *S* to its down position of thermal equilibrium and the cycle can start again until all the spins *I* are up. Evidently, if the source frequency is $\Omega=\omega_S+\omega_I$, flip-flops are forced rather than flip-flips, and the spins *I* will all go down with a polarization of equal sign to that of the *S* spins.

This simple model of the solid effect gives insight into the requirements for a polarized target material. The electronic width line should be narrow enough to forbid the simultaneous occurrence of forced flip-flops and flip-flips, which would cancel each other. This precludes large concentrations of electronic spins which would lead to a broadening of the ESR line through dipolar *S*-*S* coupling.

For small electronic concentrations, each electronic spin must service a large number N_I of nuclear spins. In order to be effective, it must be able after each forced flip-flop (flip-flip) to flip back into its thermal equilibrium position before any of the N_I nuclear spins of its sphere of influence has flipped through a nuclear relaxation mechanism. Borghini has shown that this condition is always verified in reasonably high fields if the nuclear relaxation has no other origin than their couplings with the spins *S* [Bor 66]. If however, other nuclear relaxation mechanisms are present, caused either by couplings with another species of electronic spins S', or by a purely nuclear mechanism, the condition might be violated and the nuclear polarization *P* could be much smaller than the electronic polarization P_e, as is often observed.

While the solid effect gives insight into the polarization process in plastic targets, it fails to consider the increased width of the electronic Zeeman levels in these materials and to give a precise accounting of the nuclear relaxation mechanisms involved. If the ESR line width is comparable to the transition energy between the nuclear Zeeman levels, it is not possible to induce only one of the electron nucleus transitions, as assumed by the solid effect model.

A more adequate picture of the process can be given by using the concept of spin temperature. This concept was originally developed to describe NMR in solids in the rotating frame [Red 55] and a detailed account of its application to DNP can be found in [Abr 78]. In this reference, the authors show that by considering the dipole-dipole interaction among the paramagnetic centers in the Hamiltonian (4.3), the description in terms of the quantum mechanics of transitions of individual particles is replaced by a theory of multi-particle states. Practical implications of the DNP mechanism for polarized targets are increased separations of the microwave frequencies driving the spin transitions as compared with the solid effect. This manifests in the parameter of operation of the target described in the following section.

4.4 Description of the Polarized Target

Generally speaking, the typical DNP setup consists of a cryostat to cool down the target, a magnet, a microwave system, and an NMR system to measure the polarization. The major differences of our target with other polarized targets are the small thickness of the target, its cooling mechanism and the design of

the target chamber. Next, I will describe each component, the operation of the target system, and I will finish with a summary of the parameters of operation of the target.

4.4.1 Cryogenic System and Superconducting Magnet

The cryogenic system comprises the ^{4}He cryostat and the ^{3}He-^{4}He dilution unit used to cool down the target, the means for supplying liquid helium to the cryostat, the pumping system used to reduce the temperature of the helium in the cryostat, the equipment concerned with temperature measurement and control, a gas handling system to manipulate the ^{3}He-^{4}He mixture and a gas recovery line. The superconducting magnet has been included in this section because it is directly coupled to the 4.2 K stage of the cryostat.

In order to cool the target we used one of the dilution refrigerators from the PSI Low Temperature Group. The principle of operation of this type of device is explained in detail in a variety of low temperature books such as [Pob 96] or [Lou 74], whereas some of the specific features of the PSI models are described in [Bra 90]. A general scheme and a photograph of the cryostat used are presented in figures 4.3 and 4.4. It is a continuous cycle, vertical, dilution refrigerator of the Roubeau type [Rou 66]. The central part is a cylindrical stainless-steel tube which contains the dilution unit. Around this cylinder and from top to bottom, there is one large volume that contains the ^{4}He liquid bath and its ascending vapor. That volume is also connected to the interior of the superconductor magnet by three ports (just one of them is shown in the figure), in such a way that the magnet is entirely filled with ^{4}He at 4.2 K. The lower part of the ^{4}He bath is pumped through a needle valve controlled from the upper flange of the cryostat. This effectively lowers the temperature in that region to ~2.17 K and establishes a thermal gradient around the central tube that is crucial for the proper operation of the dilution unit. The isolation volume is formed by the regions outside the ^{4}He bath that are kept under high vacuum during operation of the cryostat, thus minimizing heat conduction from the external walls. The problem of heat transport by radiation is solved by using four thermal radiation shields around the target. The two most outer shields are made of a thin foil of aluminum (~100 μm), except for a small aperture of ~6 mm x 5 mm that clears the beam path[5]. The third shield is formed by a single foil of household aluminum surrounding the magnet, except for a 6x4 mm^2 hole centered along the beam entrance point, which is covered with a 2 μm thick gold foil. The idea behind the gold foil is to use a material that while being a good thermal conductor, it is also thin enough to keep energy loss and straggling of the beam at a minimum. The inner most shield is a 1mm thick

[5] This comes at the expense of a slightly higher evaporation rate from the main ^{4}He bath.

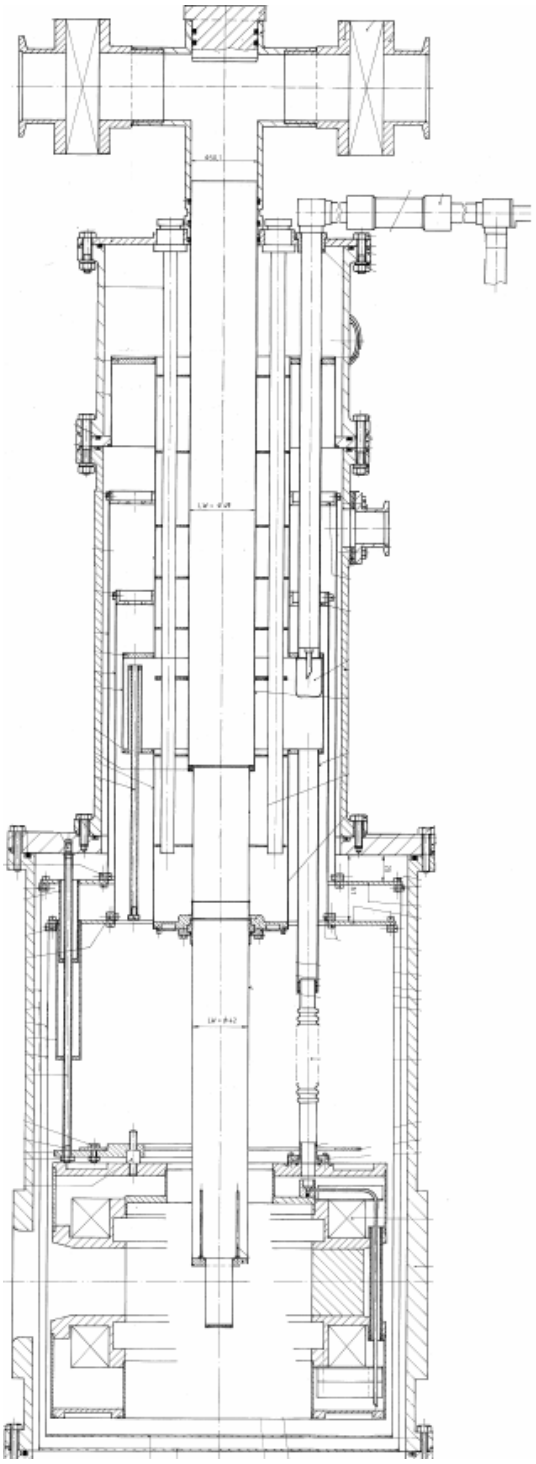

Figure 4.3. Transverse view of the cryostat.

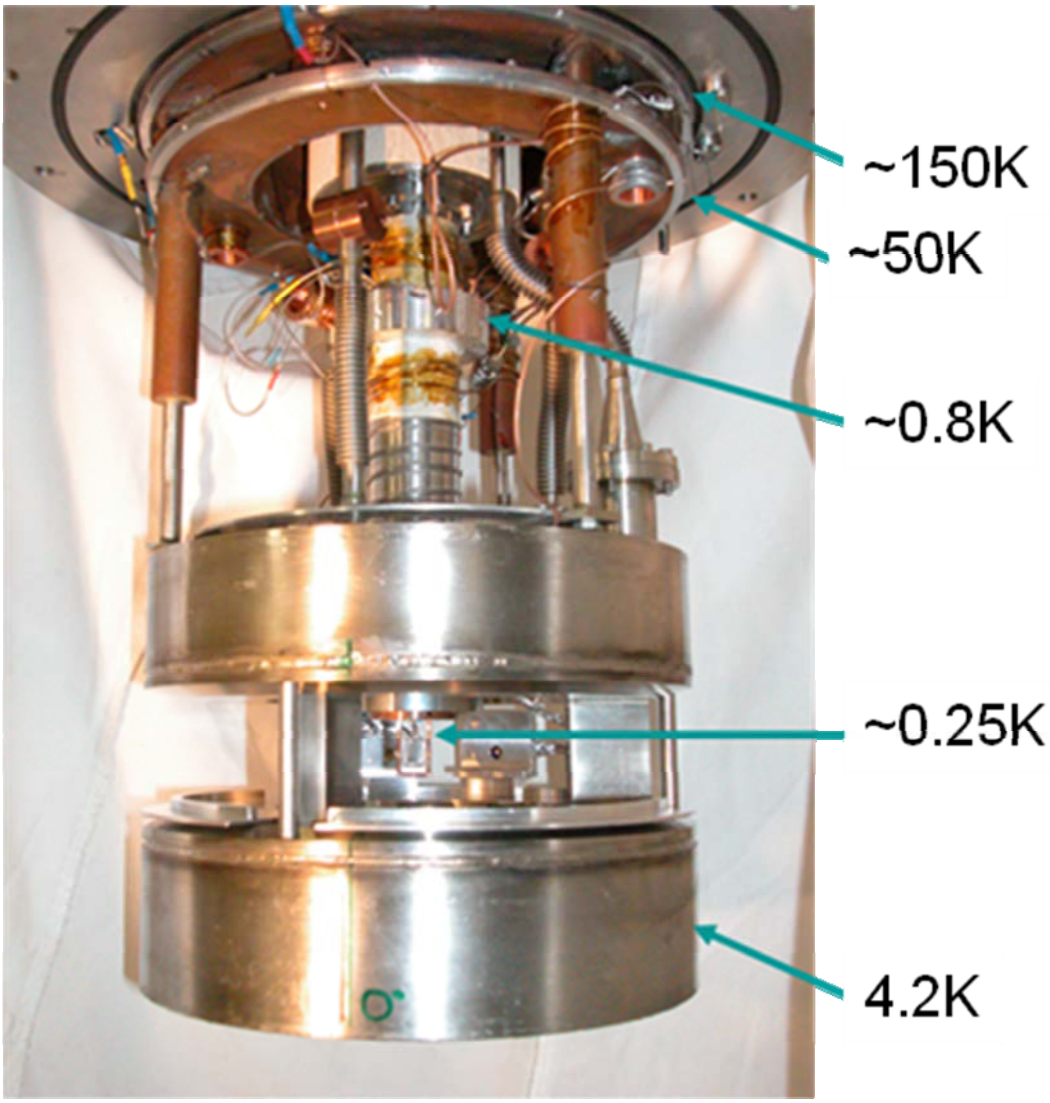

Figure 4.4. Open cryostat. Approximate values of the temperature of operation are indicated at the different anchoring sites of the thermal radiation shields described in the text. In this photograph, the open geometry of the magnet can also be appreciated.

cylinder of aluminum with an external diameter of 12 cm. It is thermally anchored to the still of the dilution refrigerator and has open window sections for the incoming beam and the outgoing recoils.

In principle, thinner foils could be used as thermal shields provided that the skin depth of thermal radiation is smaller than the thickness of the foil. According to [Jac 75], the skin depth δ can be calculated from the expression:

$$\delta \approx \frac{c}{\sqrt{2\pi\mu\sigma\omega}}, \tag{4.4}$$

where μ is the vacuum permeability, σ is the electrical conductivity of the foil, and ω is the angular frequency of the incident radiation. Conductivity measurements of gold at 4 K yield a value for σ of 0.456×10^6 Ω^{-1}-cm^{-1} [cryo x]. Using this value and assuming a black body spectrum at 300 K, whose maximum emission occurs at 31 THz, the calculated value for δ is only 10 nm. This demonstrates that much thinner foils could be used as radiation shields. However, for the purpose of the proof of principle of the polarized target, the 2 μm thickness was chosen as a compromise between thickness and robustness that allow multiple operations without running into the risk of damaging the foil.

The dilution refrigerator unit is schematically shown in figure 4.5. It is loaded from above and it fits tightly into the central tube of the cryostat. It consists of a top flange, an upper stainless steel heat exchanger, where the incoming helium condenses, a needle valve used to adjust the flow impedance, a lower liquid-liquid heat exchanger, and a mixing chamber at the very bottom. The central clearance of the unit is occupied by a cylinder originally designed as a sample holder. In our design, the target is not located in the mixing chamber and such device is used instead as a microwave guide from the exterior of the cryostat to the target chamber. The cylinder fits hermetically into the dilution unit and its lower 30 cm are filled with a tightly fitting Teflon rod that prevents superfluid helium from reaching regions of high temperature. Complete details of this unit and the sample holder device can also be found in [Bra 90]. The sample holder device terminates into a microwave horn that fits into a conical flange at the bottom of the mixing chamber. This flange presses an optical window made of sapphire and with a thickness of 6 mm, as it shown in figure 4.6. The window separates the mixing chamber from the target cell thanks to a hermetically closed indium seal[6].

[6] Indium seals have been routinely used in low temperature physics, but the design adopted in this work was first developed at Leiden in the late sixties by J. A. Konter [Kon 68] (see also [Aga 74]).

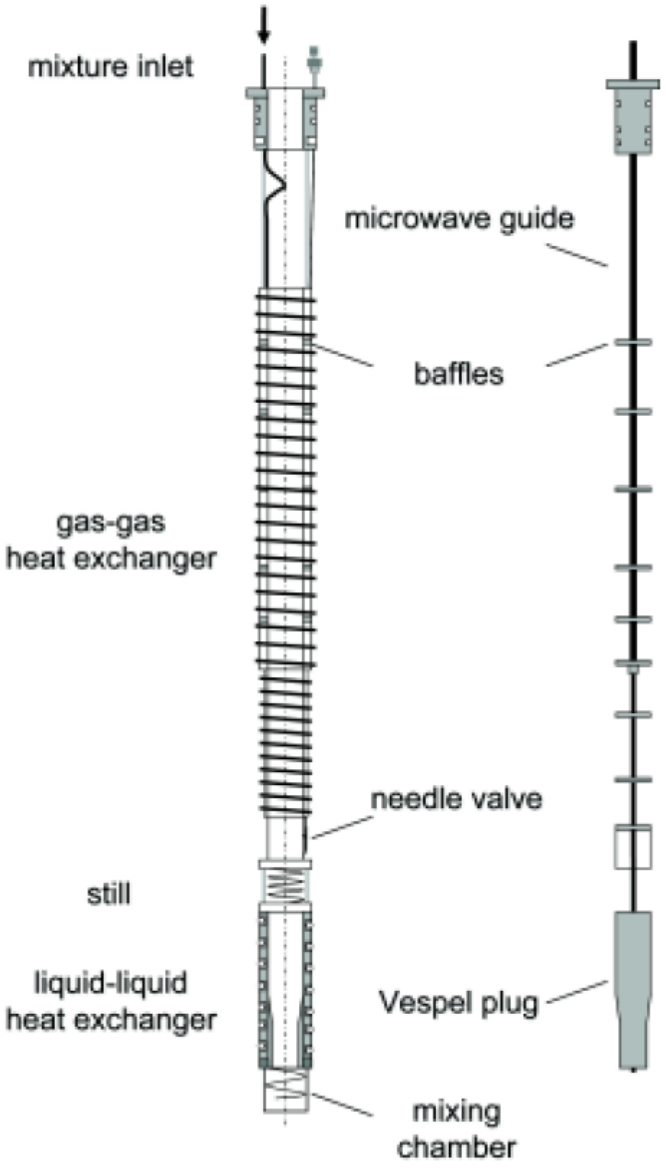

Figure 4.5. Dilution refrigeration unit (adapted from [Pie 09]). The figure on the right hand side illustrates the dilution unit, whereas the figure on the left shows the central insert with the microwave guide to irradiate the target.

Figure 4.6. Detail of the lower part of the cryostat and access to the target chamber.

The magnet is a superconducting split pair dipole wound from niobium-titanium superconductor, with a temperature of operation of 4.2 K. Its maximum energization rate is 0.5 T per minute, but it is normally energized at 0.12 T per minute. It provides a vertical magnetic field at the center of the target with a uniformity of one part in 10^4 in a 16 mm diameter sphere around the center, as is required for the NMR measurements. The two halves of the magnet are 5 cm apart and are connected by three equidistant pillars defining equal opening angles of 110° on the equatorial plane. The open geometry of this magnet makes it appropriate for a wide variety of experiments in inverse kinematics including elastic scattering and transfer reactions. This magnet is well characterized. Figure 4.7 shows the corresponding flux vectors at a maximum field of 2.5 T in the cylindrical ρ-z plane.

Another essential component of the cryogenic system is the pumping system. There are, in fact, three different sets of pumps utilized in the setup. The first set includes two vacuum pumps that evacuate the cryostat and the target chamber. During operation, the main vacuum is connected to a quadrupole mass spectrometer that continuously samples the residual gas composition at the interior of the cryostat, looking for potential leaks of superfluid ^{4}He from the target chamber. The second system is simply an oil free pump used to lower the temperature to ~2 K in the lower part of the main ^{4}He bath. The third pumping system helps circulate the ^{3}He-^{4}He mixture throughout the dilution refrigerator. It consists of a Roots blower backed by a hermetically sealed rotary pump. The Roots blower has a nominal pumping rate of 250 m^3/h, whereas the rotary pump reaches 30 m^3/h.

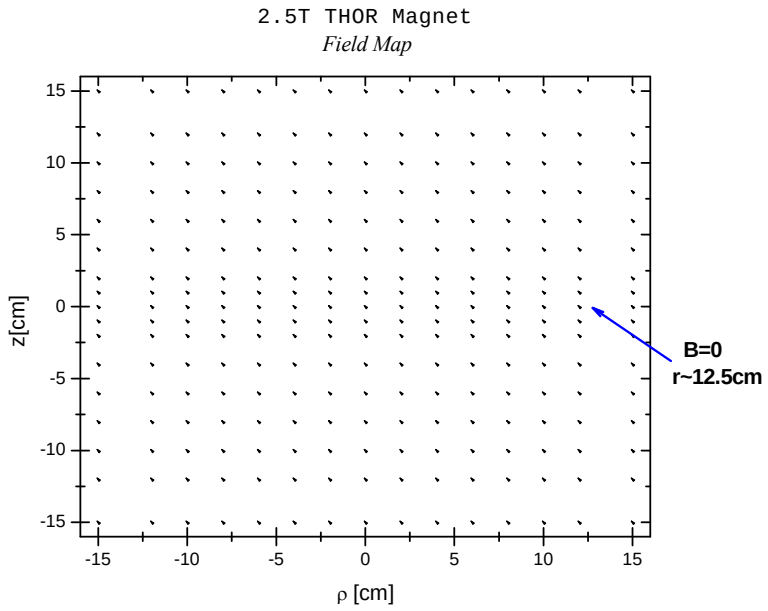

Figure 4.7. Magnetic field lines generated by the superconducting magnet of the target system. The length of the arrows is directly proportional to the strength of the field. The nominal uniformity of the field is 1 part in 10^4 in a 16 mm diameter sphere around the center of the magnet.

The description of the target chamber closes the description of the cryogenic system. It is precisely the design of this component what makes this cryogenic system unique. Figure 4.8 shows a schematic view of the target chamber and figure 4.6 and 4.9 show photographs that illustrate some details of the construction. It is attached via an indium seal to the flange with the sapphire window closing the mixing chamber. Although the target chamber is thermally anchored to the mixing chamber, there is no physical connection between the two volumes, preventing the ^{3}He-^{4}He mixture to descend into the target region. The chamber has two 7x7 mm^2, 500 nm thick, self-supported, silicon nitride windows etched on a 525 μm thick silicon frame (see figure 4.9). Considering their thickness, these windows are rather strong and only have a small impact in the energy loss of ionization particles. According to *SRIM*, 1 MeV protons only lose 33 keV after passing through a window, whereas a 38 MeV ^{12}C beam loses on average 520 keV [Zie 06].

The windows are pressed against an indium seal, making the target chamber completely leak tight for superfluid helium. Considerable effort was devoted to finding the best possible alternative for the windows. The dimensions of the grooves for the indium seal on the target chamber required a precise

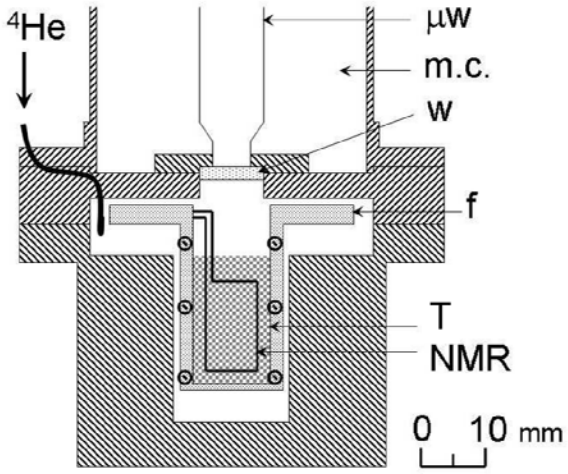

Figure 4.8. Schematic frontal view of the target chamber, situated below the mixing chamber (m.c.), with target (T) mounted on a frame (f) with visible clamping screws and a rectangular NMR copper coil. Microwaves from the waveguide (μW) enter the sample cell through a sapphire window (w).

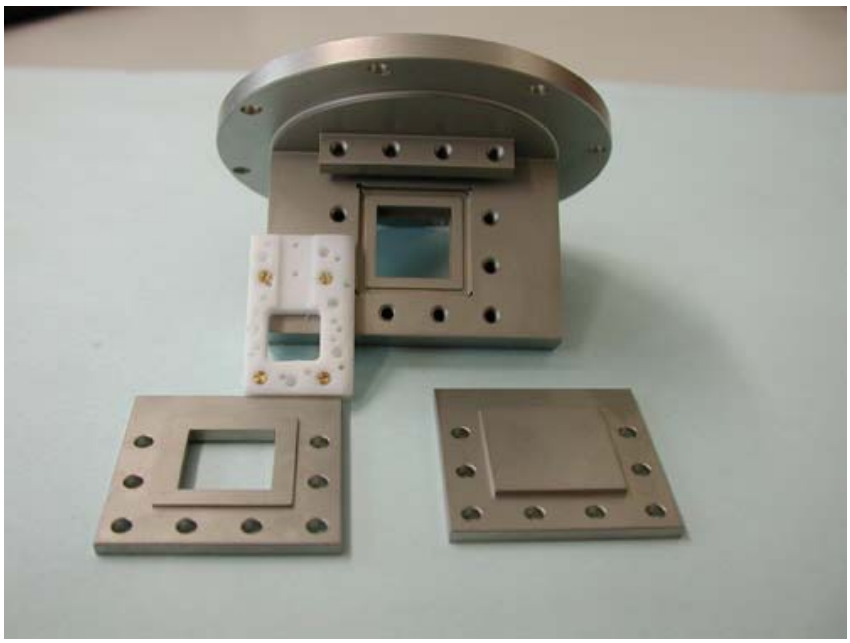

Figure 4.9. Target chamber. The square groove on the chamber has been especially designed for indium sealing. Two different sets of windows have been designed: An open frame set to be used with silicon nitride windows in a beam of particles and a solid stainless steel set of windows for cryogenic tests. The Teflon frame that holds the target foil and the NMR coil is also shown in the photograph.

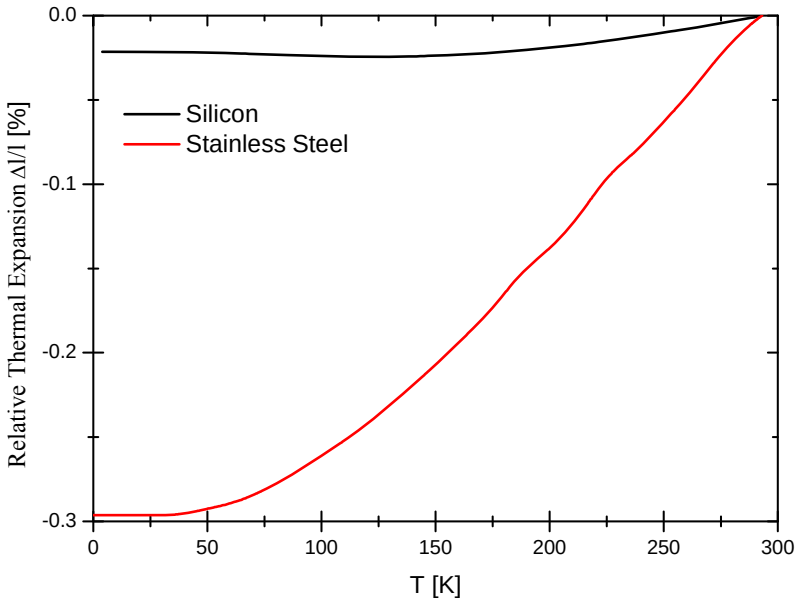

Figure 4.10. Relative expansion coefficients of silicon and stainless-steel as taken from [Lyo 77] and [Pob 96]. The difference in the expansion coefficients between the two materials at low temperatures is a critical issue that provokes cracking of the windows of the target chamber during thermal cycling.

knowledge of the thermal expansion coefficients of stainless steel and silicon [Lyo 77], [Pob 96]. Figure 4.10 shows that the relative expansion from 300 K to 4 K for these two materials is significantly different. The windows need to be replaced every time after the cryostat is warmed up. Also, the reliability of the seals of the windows is a matter of concern in the present design. As it turns out, only in ~40% of the tests, the windows were leak tight. A method to diagnose faulty seals before the target chamber reaches liquid helium temperatures remains yet to be found.

In the upper part of the target chamber, fitting in the space above the target cavity a copper flange has been mounted. This flange serves various purposes: It provides a smooth transition for the microwaves between the sapphire window and the target cavity and it also acts as a holder for the NMR coil, the target frame, two ruthenium oxide thermometers and a heater. The target itself is pressed by a Teflon frame against a 1 mm diameter copper NMR coil. The Teflon frame fits tightly into the target cavity, keeping the target in a well defined position and also serving as a sample to diagnose possible NMR problems

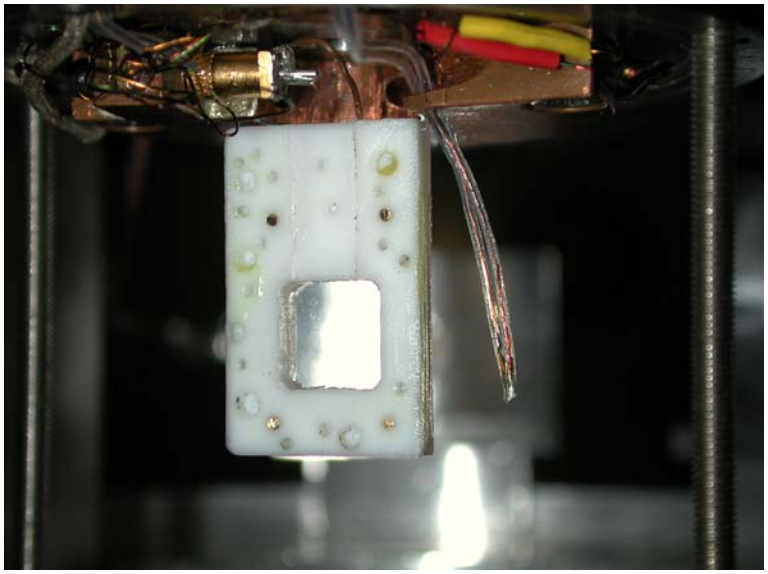

Figure 4.11. Internal components of the target chamber: Copper flange, NMR coil, Teflon frame, target foil, and thermometry.

during the course of an experiment[7]. Figure 4.11 shows these components. Last, the target chamber is connected to the exterior of the cryostat by two long, 1.1 mm outer diameter, two-layered stainless steel capillaries. These two lines allow evacuation of the air in the target chamber and are used to admit a small quantity of ^{4}He in order to further cool the target.

4.4.1.1 Operation of the Cryostat

The first step in the operation of the cryostat is to evacuate air both from the isolation volume and from the target chamber. The silicon nitride windows can withstand a differential pressure of up to 300 mbar, which implies that pumping on those two volumes should be done simultaneously and carefully. We accomplish this by using a bypass that connects the capillary lines of the target with the isolation volume from the exterior of the cryostat. Pumping proceeds through a calibrated needle valve with an impedance larger than that of the capillary lines. After ~20 h of pumping, the pressure at the interior of the cryostat is low enough to safely pump separately on the two volumes at full speed. Once the pressure in the isolation volume reaches ~10^{-3} mbar, a valve connecting the back of the cryostat with a cold trap operated at liquid nitrogen (LN_2) temperature can be opened, bringing down the pressure at a much faster rate. Safe evacuation of the whole system to the point one can start to cool down takes, an average of 40 h.

[7] This can be done by tuning the NMR system to the resonance frequency of the ^{19}F nuclei in Teflon.

The next step is pre-cooling of the cryostat and the magnet with LN_2. The fluid is drawn from a Dewar through the siphon of the cryostat and the evaporated gas is dumped into the atmosphere after passing through a flow-meter that allows monitoring of the evaporation rate, which varies between 80 and 110 *l*/h, depending on the length of the transfer line. Indirect measurements of the temperature are obtained through a set of four resistors located at different heights along the magnet and the main ^{4}He bath of the cryostat. After ~3 h, the inner parts of the cryostat reach a temperature close to the boiling point of nitrogen, at which point the flow is interrupted. Care should be taken that no LN_2 remains inside the cryostat before proceeding to fill the cryostat with helium. If the pre-cooling went well, it typically takes ~1 h until all nitrogen has evaporated from the magnet.

After filling the dilution unit with a small amount of ^{4}He gas (to act as exchange gas, establishing thermal contact with the rest of the cryostat), the transfer of liquid ^{4}He can be started. It normally takes ~1 h to fill the main ^{4}He bath of the cryostat, although it requires ~22 h to fully thermalize the rest of the cryostat at liquid helium temperature. Transfer of helium is routinely done from a 250 *l* Dewar, with a daily consumption of ~70 *l*. Once thermalization at 4.2 K has taken place, the exchange gas is pumped out of the cryostat and pumping on the main ^{4}He bath through a needle valve is initiated in order to establish a temperature gradient between the bottom of the bath and its surface. At the same time, ^{3}He-^{4}He mixture is admitted into the dilution unit for condensation.

The total amount of ^{3}He-^{4}He is optimized in such a way that gas is condensed until the liquid level fills the still, whereas the relative concentration of ^{3}He in the mixture is imposed by the condition of having the phase boundary between the ^{3}He rich phase and the dilute phase in the mixing chamber. In this setup we routinely used 150 *l* NTP of mixture with a 30% content of ^{3}He. The mixture is circulated by the Roots blower in series with the rotary pump, which allows a pumping rate of ~1 mmol/s at a pumping pressure of ~0.1 mbar. The exhausted mixture is passed first through an oil mist filter and then through a charcoal trap at LN_2 temperature. In this way it can be purified before entering into the dilution unit again. Typically, condensation of the mixture and steady flow conditions are achieved within ~8 h, reaching temperatures of ~100 mK in the mixing chamber, ~220 mK in the copper flange inside the target chamber and ~360 mK in the vicinity of the target.

If one is to polarize the target at his point, the results would be far from optimal. The temperature of the target itself should be lowered and the large gradient inside the target chamber should be first minimized.

Both effects can be achieved by admitting a very small amount of ^{4}He inside the target chamber through the capillary lines. This is done by isolating previously cleaned ^{4}He gas in a chamber at a certain pressure. Given the dimensions of the target chamber, a minimum amount of 0.26 cm^3 of STP ^{4}He is required to effectively bring further down the target temperature. Such small quantity of helium condenses into a superfluid film with an estimated thickness of ~0.3 μm inside the target chamber[8] in ~4½ h. This is very attractive from the point of view of using the target in reactions with ionizing particles: In Chapter 5 it is demonstrated that energy losses of low energy recoil protons due to the ^{4}He film are practically negligible. Faster condensation times of the superfluid film are also feasible by increasing the initial amount of ^{4}He gas, for instance, 6 cm^3 STP ^{4}He have been condensed in ~10 min without significantly altering the energy of recoiling protons from the target between 3 and 11 MeV. With that amount of helium inside the target chamber, the temperature in the mixing chamber is ~100 mK, 180 mK in the copper flange and 208 mK in the target foil. Even with these values, the temperature gradient is still considerable. Although there is no conclusive evidence, this fact might be due to the Kapitza resistance between the materials inside the target chamber and ^{4}He [Wil 67], [Pob 96]. If this is the case, it might not be possible to reduce the temperature inside the target chamber further. I will come back to this point in chapter 6.

The cooling mechanism of the target foil through the superfluid helium film was first proposed and demonstrated at PSI [Bra 96]. Its effectiveness in obtaining high levels of polarization is illustrated by figure 4.12, where a polystyrene target has been polarized at 1 K and 3.5 T. As can be seen, there is a dramatic enhancement of the polarization once the superfluid film covers the surface of the target. Once the target foil is covered by superfluid helium, one can proceed to polarize the target by irradiating with microwaves at the right frequency, depending on whether positive or negative polarization is desired. This process is monitored by the NMR system, as is explained next.

4.4.2 NMR and Microwave Systems

A continuous wave NMR system is used to sample the target polarization, as it is indicated in figure 4.13. It consists of the copper coil that has already been described, a coaxial line, a Liverpool Q-meter [Cou 93], and a radiofrequency generator. Frequency sweeping and data acquisition are computer controlled via Labview routines [Hau 08].

[8] As is pointed out by [Wil 67], the determination of the thickness of a film of superfluid ^{4}He suffers from multiple uncertainties. Best estimates are often off by an order of magnitude due to surface roughness and cleanliness.

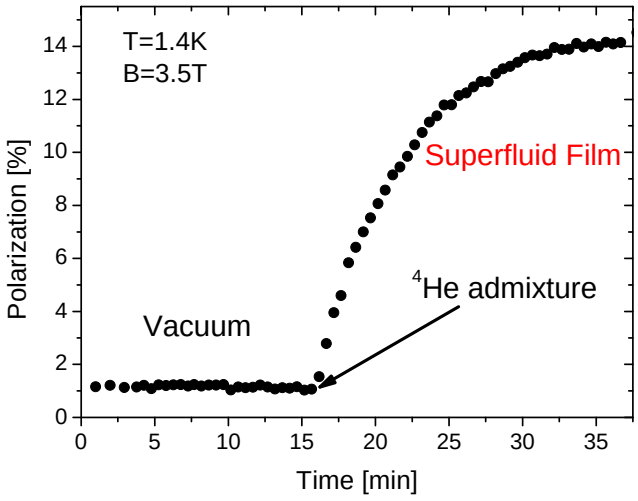

Figure 4.12. Polarization of the target in vacuum and in the presence of a superfluid film of ^{4}He. The dramatic enhancement in polarization demonstrates the power of the cooling mechanism of the target through a superfluid ^{4}He film.

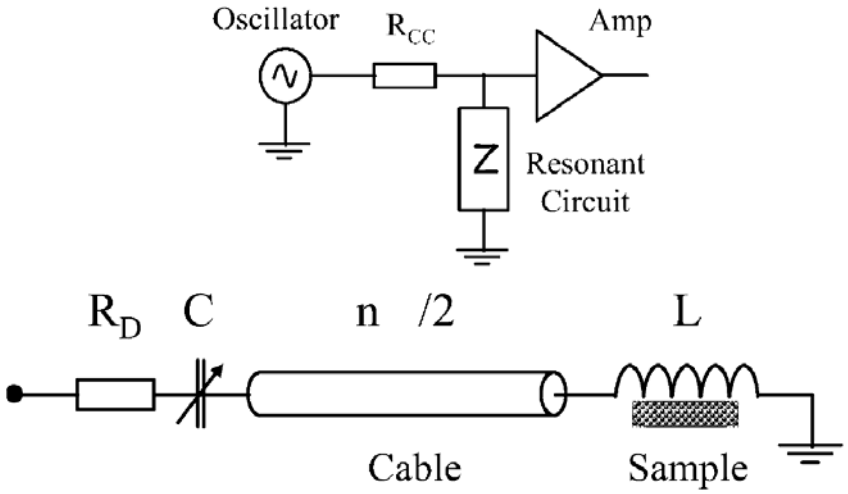

Figure 4.13. Schematic view of an NMR system. The NMR target (sample) coil is connected to the rest of the resonant circuit via a resonant nλ/2 cable. Adapted from [Hau 04].

Continuous wave NMR is a suitable tool for sampling proton polarization as the energy delivered by radiofrequency signals from the coil to the target material can be minimized by sweeping the frequency at the proper rate. Thus, 1000 frequency sweeps performed every two minutes within a 600 kHz band show no significant effect on the performance of the target at a temperature of 225 mK. Figure 4.14 shows typical NMR signals obtained at 2.5 T from polarized protons at 208 mK. The fundamentals of the NMR technique as a polarization sampler are explained in detail in [Gol 75] and a good historical account of the role of NMR in the field of polarized solids targets is available in [Cou 04]. The method for measuring polarization is based upon the fact that nuclear spins in the target are flipped in the direction perpendicular to the coil by an RF signal at the NMR frequency. Goldman demonstrated that if only one spin species is present, the frequency integral of the absorption signal (line shape of the NMR signal) is proportional to the net polarization in the target [Gol 75]. In turn, the absorption signal corresponds to the imaginary part of the magnetic susceptibility of the target, χ, which is a function of the frequency:

$$\chi = \chi' - i\chi'' . \tag{4.5}$$

Experimentally, what is measured is a voltage proportional to the absorption signal χ''. On the other hand, L_T, the combined inductance of the NMR coil, L, and target is given by:

$$L_T = L(1 + 4\pi\eta\chi) , \tag{4.6}$$

where η, the filling factor, expresses the degree of coupling between the target and the coil. Such change in inductance effectively modifies the impedance of the NMR coil and hence the Q-value of the resonating circuit attached to it. χ'' can then be measured by carefully balancing the impedance associated with (4.6) with an LCR circuit. The idea is as follows. The impedance Z of such a circuit is determined by:

$$\frac{1}{Z} = \frac{1}{R + i\omega L(1 + 4\pi\eta\chi)} + i\omega C , \tag{4.7}$$

where R is the resistance of the circuit, C its capacitance and ω the angular frequency of the RF signal. In the setup used, the dispersive component of the susceptibility, χ', is minimized by the use of transmission lines from the coil to the Q-meter with a length that is an odd multiple of $\lambda/2$ at the resonance frequency (λ being the wavelength of the RF wave in the cables)[9]. Therefore, the main effect of the target material is to add a real term to the resistance R. Assuming that χ' is negligible and that the circuit is in resonance, the magnitude of the impedance extracted from (4.7) is:

[9] This guarantees to a first approximation that the coil impedance as seen from the remote end of the cable is the same as would be seen in the absence of the cable.

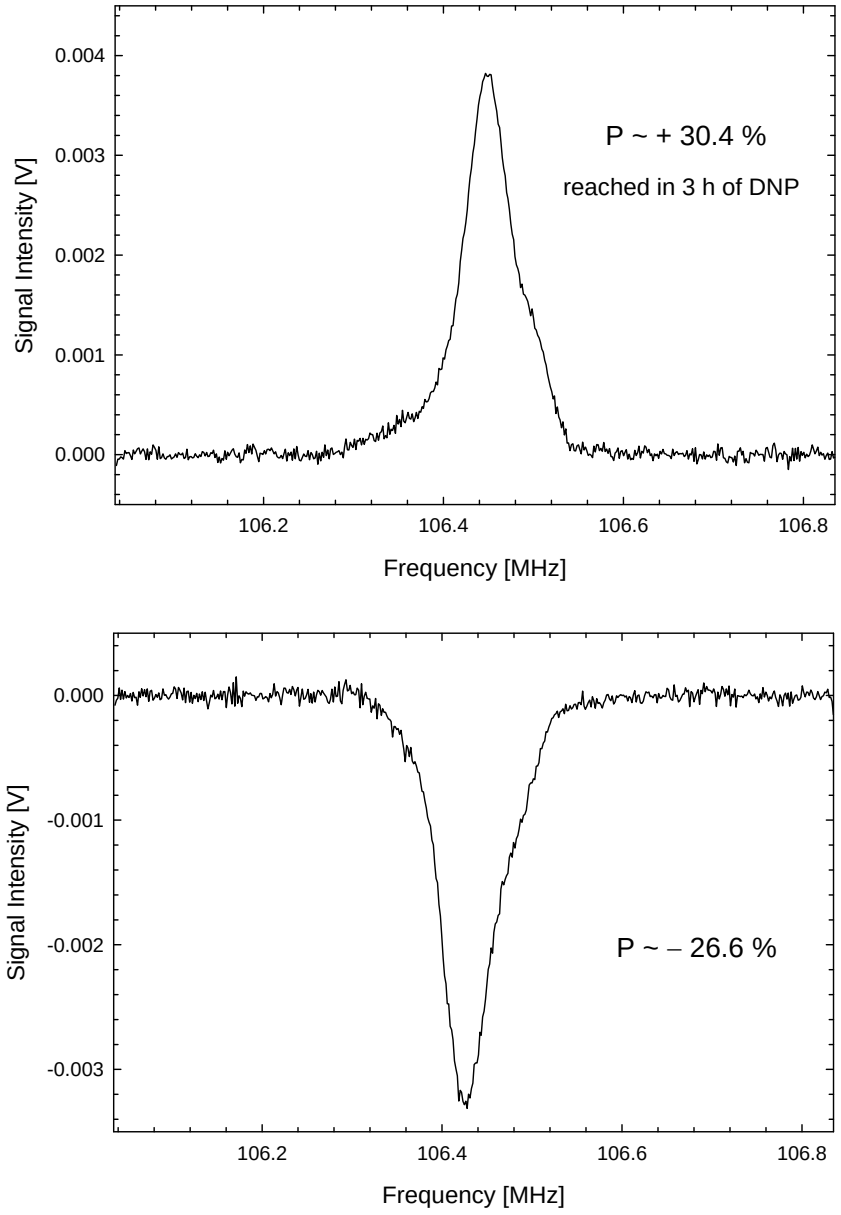

Figure 4.14. Proton NMR signals from the target at 2.5 T and 208 mK. The asymmetry in the signals is due to non-homogeneities from stray components of the magnetic field. Such broadening affects the maximum polarization that can be achieved as well as the precision of thermal equilibrium calibrations (see appendix B).

$$Z = \frac{QR}{1 + 4\pi Q\eta\chi''}, \tag{4.8}$$

where $Q = \omega L / R$ is the quality factor. Hence, the absorptive part of the susceptibility can be expressed as:

$$\chi'' = \frac{1}{4\pi Q\eta}\left(\frac{QR - Z}{Z}\right). \tag{4.9}$$

According to this result and to [Gol 75], the target polarization P can therefore be expressed as:

$$P = \kappa\int_0^\infty \frac{1}{4\pi Q\eta}\left(\frac{QR - Z}{Z}\right)d\omega, \tag{4.10}$$

where κ is a constant that depends on the measurement instruments. Although this is a closed expression, η is in practice very difficult to evaluate. Instead, the two constants appearing in the expression are combined into a single constant that is determined by a thermal equilibrium calibration as is shown in Appendix B.

A final remark concerning the NMR system is related to the transmission lines from the NMR coil to the Q-meter. Several thermal anchoring schemes were originally considered for the low noise coaxial cables used, but due to the rather high thermal conductivities of good electrical lines it was not possible to use a $\lambda/2$ cable. Instead we used a $3\lambda/2$ cable. The thermal load on the mixing chamber of the cryostat brought by the NMR lines was minimized by using stainless steel coaxial cables without external insulations. Such lines provided a reasonable solution at a cost of attenuating the signals -0.78 dB/m at 106 MHz.

As for the microwave source we used, is consisted of a 70 GHz oscillator with a band width of ~500 MHz and a maximum power output of 240 mW distributed over an area of 0.70 cm^2. The output of the oscillator is regulated by a graphite absorber coupled to a waveguide where the microwaves travel until they reach the target chamber. Unfortunately, the wave guides have not been properly characterized and therefore no direct measurement of the microwave power delivered to the target is available. Instead, the microwave power delivered to the target is regulated empirically by correlating the attenuator settings with the integral of the NMR signal in real time.

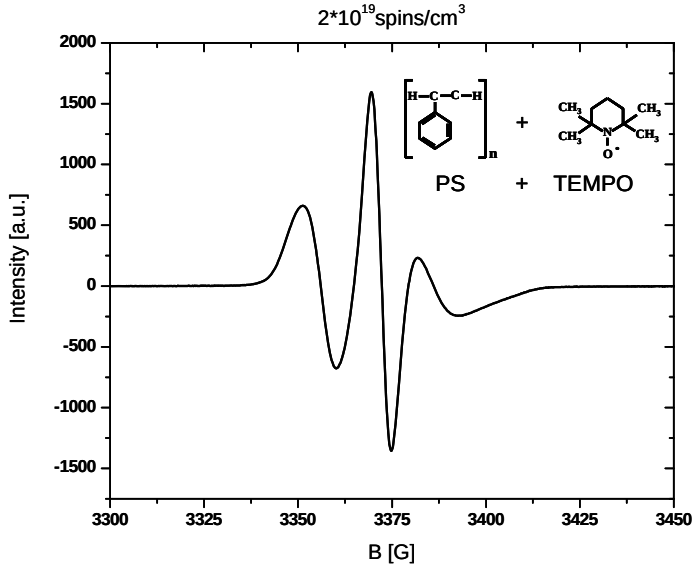

Figure 4.15. EPR spectrum of the target at room temperature. The three peaks indicate the dipolar coupling between the free electron and the nitrogen nucleus in TEMPO.

4.4.3. Target Material

As was mentioned before, the material of choice for the proton target is polystyrene ($[C_8H_8]_n$) doped with the free radical TEMPO (2,2,6,6-tetramethylpiperidin-1-oxyl) [Roz 70], [Bun 04], at a concentration of $2*10^{19}$ radicals/cm^3. Figure 4.15 depicts the molecular structure of the compounds together with an EPR spectrum of the target that clearly shows the presence of localized free electrons in the plastic. It is worth noticing that deuterium targets can also be prepared in a very similar way by using deuterated polystyrene and TEMPO [Bra 00], [Bra 04]. For the normal compounds, the dilution factor[10] of protons in polystyrene is d_f=0.5, a value that is lower than the dilution factor of organic compounds with similar physical properties, such as polyethylene ($[C_2H_4]_n$, d_f=0.67). In spite of this, polystyrene was chosen over polyethylene because previous experience at PSI with EPR spectra have shown that the migration time of TEMPO from the plastic matrix is longer in this material [Hau 05], which would give more flexibility in case a single target was needed in experiments well separated in time.

[10] The dilution factor is defined as the ratio between the amount of polarizable nuclei and the total number of nuclei in the target.

Preparation of the target foils includes two crucial steps, namely, the production of uniform foils and the mixing of TEMPO in the plastic foil. Unlike polyethylene, it is very difficult to find commercially available polystyrene foils in the thickness range of interest for low energy nuclear physics experiments[11]. Instead, the foils have to be prepared by dissolving pellets of polystyrene in a glass container filled with toluene. The optimal polystyrene to toluene weight ratio of the solution is 1:10. The solution is heated to ~120 °C until the pellets have completely dissolved. At this point, TEMPO is added to the solution and the glass container is sealed in order to minimize losses of the dopant. The amount of TEMPO added , m_{TEMPO}, can be determined from the relation:

$$m_{TEMPO} = \frac{m_{PS} \cdot M}{\rho_{PS} \cdot N_A} n \,, \tag{4.11}$$

where m_{PS} is the mass of polystyrene in the solution, ρ_{PS} its density, M the molecular weight of TEMPO, N_A the number of Avogadro, and n the desired concentration of paramagnetic centers in the target. As soon as TEMPO is added to the solution, it acquires a slightly red coloration. If the uniformity of the target is not an issue, the doped solution can be poured into uniform large glass plates after a few minutes[12]. At room temperature it takes ~8 h until toluene has evaporated, leaving behind a foil of polarizable polystyrene adhered to the glass. Recovery of the foil can be achieved by floating it in distilled water. On the other hand, if the uniformity of the target is a matter of concern, the best alternative is to use the spin coating technique.

In the spin coating technique, the doped solution is spun at high speed, forming a uniform layer on a suitable substrate upon drying [Wea 96]. Since a high uniformity is required, it is crucial to prepare the solution for the targets in a clean room environment and to deposit it on a polished silicon wafer. In this technique, the most important parameter governing the thickness and quality of the foils is the viscosity of the solution, which is directly related to the concentration of polystyrene in toluene. Figure 4.16 shows an example of the thickness that can be obtained from different concentrations. Empirically, it was determined that a spin speed of 2000 rpm maintained over 45 s after an acceleration period of 2 s gives good results. Higher speeds might be used to produce foils with thicknesses below 100 μg/cm^2, but its handling is extremely delicate. Longer spinning times on the contrary do not have a major impact on the foils as the solvent evaporates rapidly and the viscosity of the solution reaches high values soon after the spin coating begins. Using this technique, we have prepared foils with thicknesses between 125 μg/cm^2 and 3.4 mg/cm^2 at the Laboratory for Nanotechnology in PSI and at the Institute of Mechanical Systems

[11] Preparation of polymer foils for DNP by diffusion is also possible, as was described in [Bra 95].
[12] This method typically yields variations of ~0.5mg/cm^2 in target thickness.

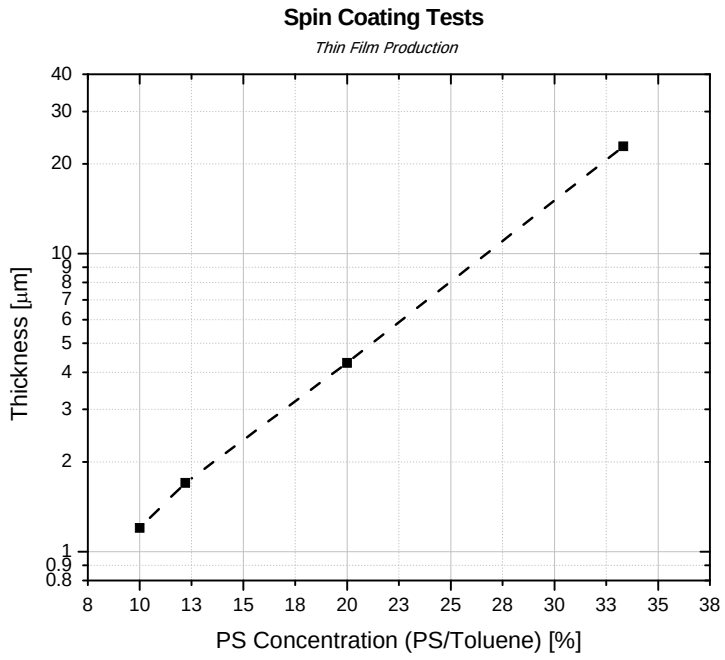

Figure 4.16. Thickness of spin coated polystyrene foils doped with TEMPO as a function of the concentration of the polymer in a toluene solution. The samples were prepared by spinning the solution for 45 s at 2000 rpm after 2 s acceleration time followed by 15 m rest on a hot plate at 50 °C.

in ETH Zurich. The uniformity of the foils was checked in all cases with a stylus profiler and it was found to be better than 2% ($\Delta t \sim 200$ nm). Based on the range of thicknesses reached in this way, it is possible to design polarized targets for experiments requiring good uniformity.

4.4.4 Performance of the Polarized Target in Cryogenic Tests

In the experimental setup described above, two adjustable parameters govern the performance of the polarized target: Its temperature and the strength of the magnetic field. A third parameter to be considered is the concentration of paramagnetic centers in the samples, but this quantity has been kept fixed in these studies[13]. Protons in the target were polarized in a magnetic field of 2.5 T. In the best cases, microwave irradiation of the target started at a base temperature of 208 mK in the target and 100 mK in the mixing chamber. Under those conditions, the maximum polarization obtained was 31% for the spin up state and

[13] A report on the effects of the concentration of TEMPO in polystyrene can be found in [Bra 00], where a concentration of $2*10^{19}$ spins/cm^3 was recommended as it resulted in a reasonable compromise between maximum polarization and long relaxation times of the targets.

26% for the spin down state. The values were achieved after irradiating the target with frequency modulated microwaves at 1 kHz for ~3 h. The frequency of the microwaves used was 69990 MHz (up) and 70265 GHz (down), i.e. they are 275 MHz apart, a value that is close to the figure indicated by the solid effect. Similar results can be found in [Bra 00] for much thicker polystyrene targets doped with different concentrations of TEMPO.

4.4.5 Magnetic Field and Temperature Dependence of the Performance

One of the major challenges in operating the polarized targets in reactions with charged particles is the effect of the magnetic field on their trajectories, particularly in low energy reactions. Depending on the experiment, it might be necessary to operate the target in the so called frozen spin mode, where once a certain level of polarization has been achieved, microwave irradiation is interrupted and the magnetic field is lowered to a value more appropriate for the detection of particles. In this case, measurements take place while the spins of the protons in the target gradually reach a Boltzmann distribution. Once the polarization level is so low that no significant information can be obtained, the magnetic field is ramped again to a full value, so a new polarization cycle might begin. Since many experiments will require operation of the target in frozen spin mode, it is useful to illustrate the effect of both magnetic field and temperature on the relaxation time of the target. Figure 4.17 shows the dependence of the relaxation time on the temperature of the target at 2.5 T, while figure 4.18 shows the dependence on the magnetic field at a constant temperature of 230 mK. The behavior observed in both cases is in agreement with previous results reported in [Bra 00].

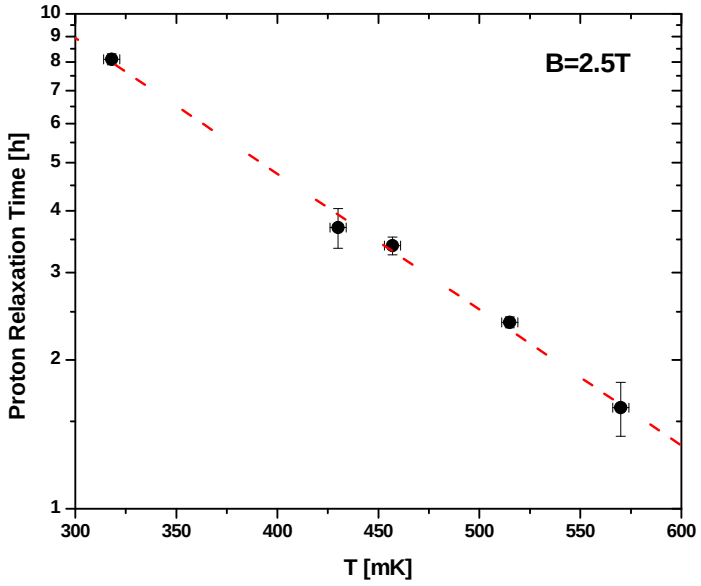

Figure 4.17. Dependence of the relaxation time with the temperature at a constant magnetic field. The observed exponential behavior is in agreement with similar works reported in [Gol 82].

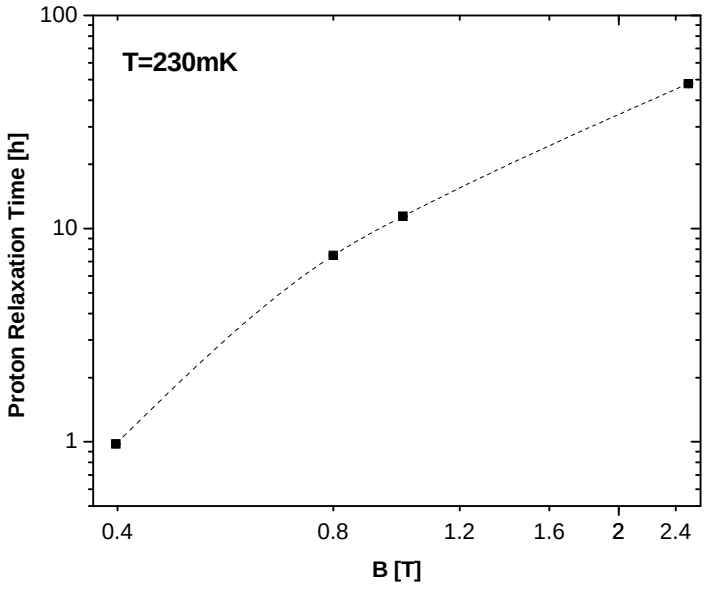

Figure 4.18. Dependence of the relaxation time with the magnetic field at a constant temperature.

CHAPTER 5

Proof of Principle of the Polarized Target

5.1 Introduction

We decided to demonstrate the use of the polarized target using elastic resonant scattering of a stable beam in inverse kinematics with the thick-target technique. In this way, while the experimental conditions were comparable to those with RIBs, the additional complications associated with their use were avoided. We chose the elastic scattering of ^{12}C with protons, leading to the population of resonant states at 3.50 MeV and 3.55 MeV in ^{13}N, as the test case. For this reaction, the low level density at low excitation energies results in a clean separation of the resonant states formed during the scattering process. Besides, the large compilation of data on this reaction available in the literature (see [Azj 91] and references therein) serves as support for our studies. In particular, during the late fifties, Phillips and Miller carried out an experimental program aimed to characterize nuclear reactions for the purpose of nuclear polarimetry at low energies. The elastic scattering of protons by ^{12}C was one of the reactions they studied, resulting in the extensive set of data of analyzing powers shown figure 5.1 [Phi 59].

As part of the proof-of-principle of the polarized target system, we explored the experimental issues associated to a reaction with an unpolarized target. For this we used the thick-target technique (with polystyrene targets) in conjunction with a ^{12}C beam produced at HRIBF. In section 5.2, we characterize the ^{12}C-p reaction in inverse kinematics and discuss the challenges associated with the presence of C in the target. Tests with the polarized target took place at PSI and are described in section 5.3. Such tests include the assessment of effects induced by the beam on target, the study of the impact of the cooling mechanism of the target on the energy spectra from the recoils, and studies on the influence of the magnetic field on the trajectories of charged particles.

5.2 Elastic Scattering of Unpolarized Protons by ^{12}C at HRIBF

We intend to use the polarized target at low and intermediate energies, where spin dependent observables can provide valuable spectroscopic information. We decided to test the target with a beam energy of just a

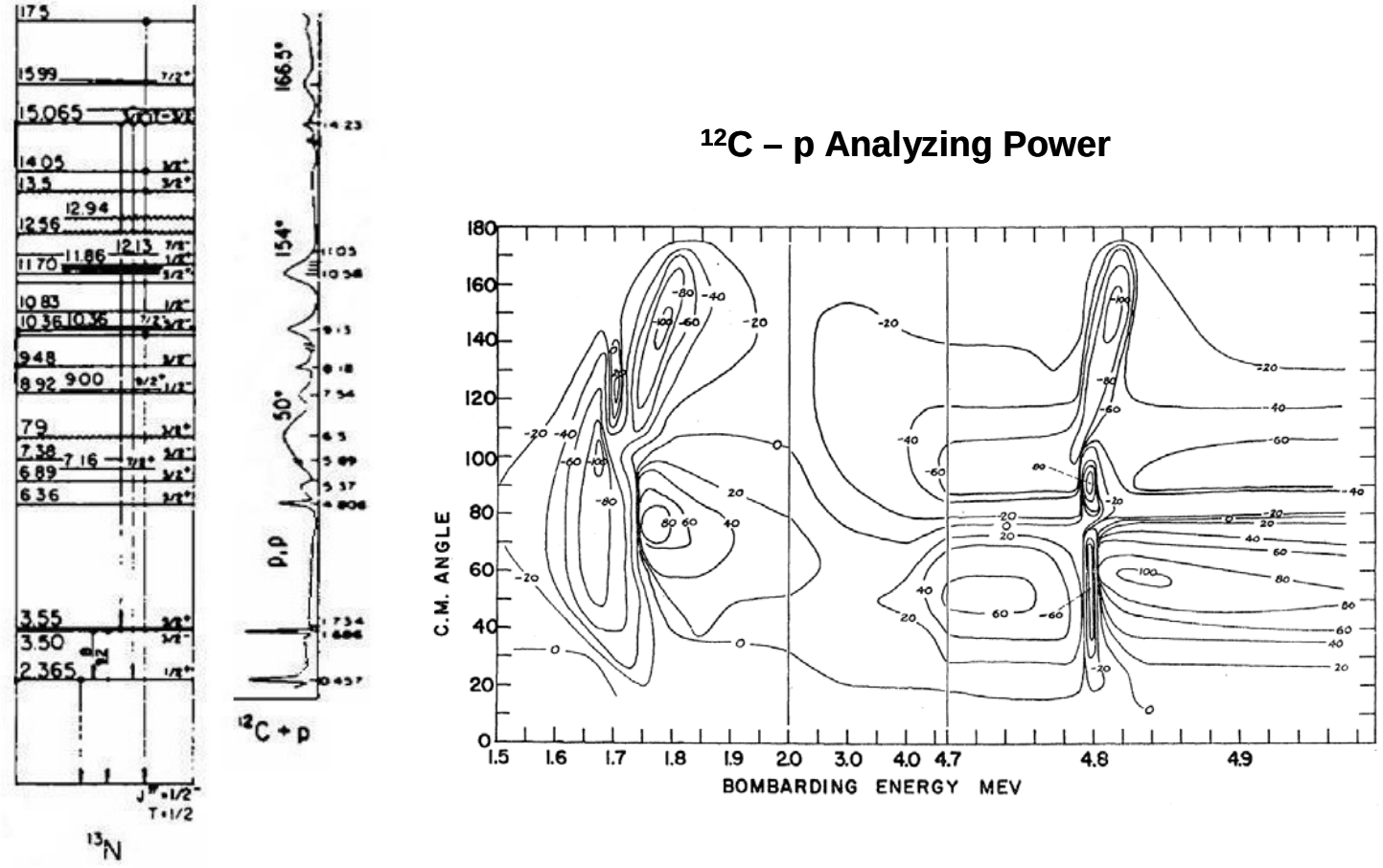

Figure 5.1. (*a*) Energy levels of ^{13}N. Energy values are plotted vertically in MeV, based on the ground state as zero. Some typical thin-target excitation functions of the ^{12}C+*p* reaction are shown schematically, with the yield plotted horizontally and the bombarding energy vertically. Bombarding energies are indicated in laboratory coordinates and plotted to scale in c.m. coordinates. This figure has been adapted from [Azj 91]. (*b*) Contour plot of analyzing powers for the *p*-^{12}C reaction in normal kinematics, adapted from [Phi 59].

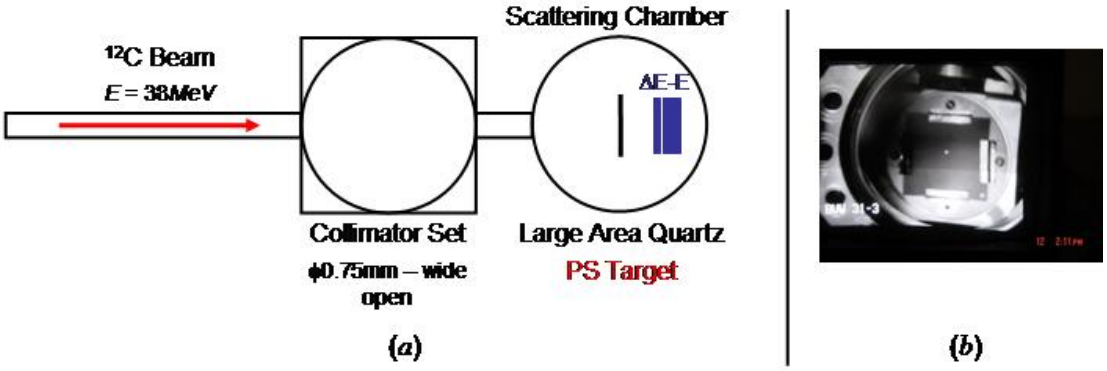

Figure 5.2. (*a*) Schematic view of the setup initially used at HRIBF to explore experimental issues associated with the ^{12}C scattering on a polystyrene target. Particle identification from the silicon ΔE-E telescope placed 5 cm behind the target allowed us to estimate the contributions from reactions with the carbon nuclei in the plastic target. (*b*) Beam spot corresponding to 10 pA of ^{12}C impinging on the diagnostics quartz after passing through a ϕ1 mm collimator.

few MeV per nucleon. The operation of the target becomes increasingly challenging as the energy of the reaction decreases. Under this condition, the effect of the magnetic field on the trajectories of beam and recoils becomes critical for the performance and interpretation of possible experiments.

The initial step towards evaluating the performance of the polarized target during beam irradiation was the exploration of the ^{12}C-*p* reaction and of possible experimental issues under controlled conditions at HRIBF. We used ^{12}C beams from the 25 MV Tandem, as well as unpolarized polystyrene targets with thicknesses just above the required value to stop the beam. The first tests were performed using the setup schematically shown in figure 5.2.(*a*) at bombarding energies of 24 and 38 MeV. The beams were directed into the target after passing through a collimator with sets of holes ranging from 0.75 mm to wide open. Figure 5.2.(*b*) illustrates the shape of the beam spot as it impinged on a sensitive Al_2O_3:Cr screen placed in the position of the target. The screen served as a visual indicator for beam tuning purposes at relatively high intensities (~10 pA≈6.2*10^7 pps) but, once the beam was tuned, the current was reduced to the point where no light from the screen could be detected with the naked eye. This occurs at intensities around 1.3*10^5 pps. The targets were mounted on an eccentric rotating ladder that permitted to change the target position to a fresh spot whenever necessary. We placed our detection system 5 cm behind the target, at zero degrees. It consisted of a telescope for charged particles formed by two surface barrier detectors with thicknesses of 117 μm for the ΔE (front) and 181 μm for the E (back) stages.

Particle identification of the recoils emitted in the reactions can be performed with the silicon telescope by taking advantage of the energy loss dependence of ions on their mass m and atomic number z. According to Bethe's formula for non-relativistic particles, the energy loss of a particle with incident energy E is given by [Kno 79],

$$\frac{dE}{dx} = C_1 \frac{mz^2}{E} \ln\left(C_2 \frac{E}{m} \right), \tag{5.1}$$

where C_1 and C_2 are constants. At energies relevant for low energy nuclear physics, the logarithmic term behaves in a smoother way than the inverse of the energy. Therefore, the ΔE signal approximately follows a hyperbolic behavior as a function of the total energy. In addition, the mass and the atomic number of the detected particle are parameters that scale up or down the magnitude of the energy loss in the ΔE detector. As a result, it is possible to isolate contributions from a single nuclear species in energy spectra.

5.2.1 Effects from Carbon Nuclei in the Target

Figure 5.3 shows the correlation between the energy deposited in the ΔE detector and the sum of the energies deposited both in the front and back detectors for reactions at the bombarding energies mentioned earlier. Three different groups of events corresponding to different types of nuclei can be clearly identified on each plot, namely, protons, deuterons and alpha particles. The predicted hyperbolic branches of the plot for each type of particles are enclosed in the figure by 'banana' gates. However, there also appear inverted branches for some of the particle distributions in the figure, which indicate that the effective thickness of the E-detector is insufficient to collect the residual energy of the high energy recoils –that punch through the detector— and therefore, only a fraction of the total energy is measured. Information on punch-thru distributions can in principle be recovered provided a precise knowledge of the detectors thicknesses, dead layers and stopping powers is available.

In order to fully interpret figure 5.3, we must recall that the recoils are primarily originated in two reactions: ^{12}C-p and ^{12}C-^{12}C. There were, of course, other nuclei present in the target but, since their abundance was well below 1%, we will neglect them in this analysis. Let us consider first the ^{12}C-p reaction and the particles that can result from it. Given the available phase space and the thickness of the targets used, the only particles that could potentially be observed were protons. Moreover, the only mechanism allowed for this reaction at low energies is elastic scattering. This arises from the fact that the first excited state of ^{12}C has an excitation energy of 4.438 MeV, implying that for this system, inelastic scattering only needs to be taken into account if the beam energy was above 57 MeV in inverse kinematics. Most of the protons emitted in the ^{12}C + p reaction are emitted from resonant states in ^{13}N.

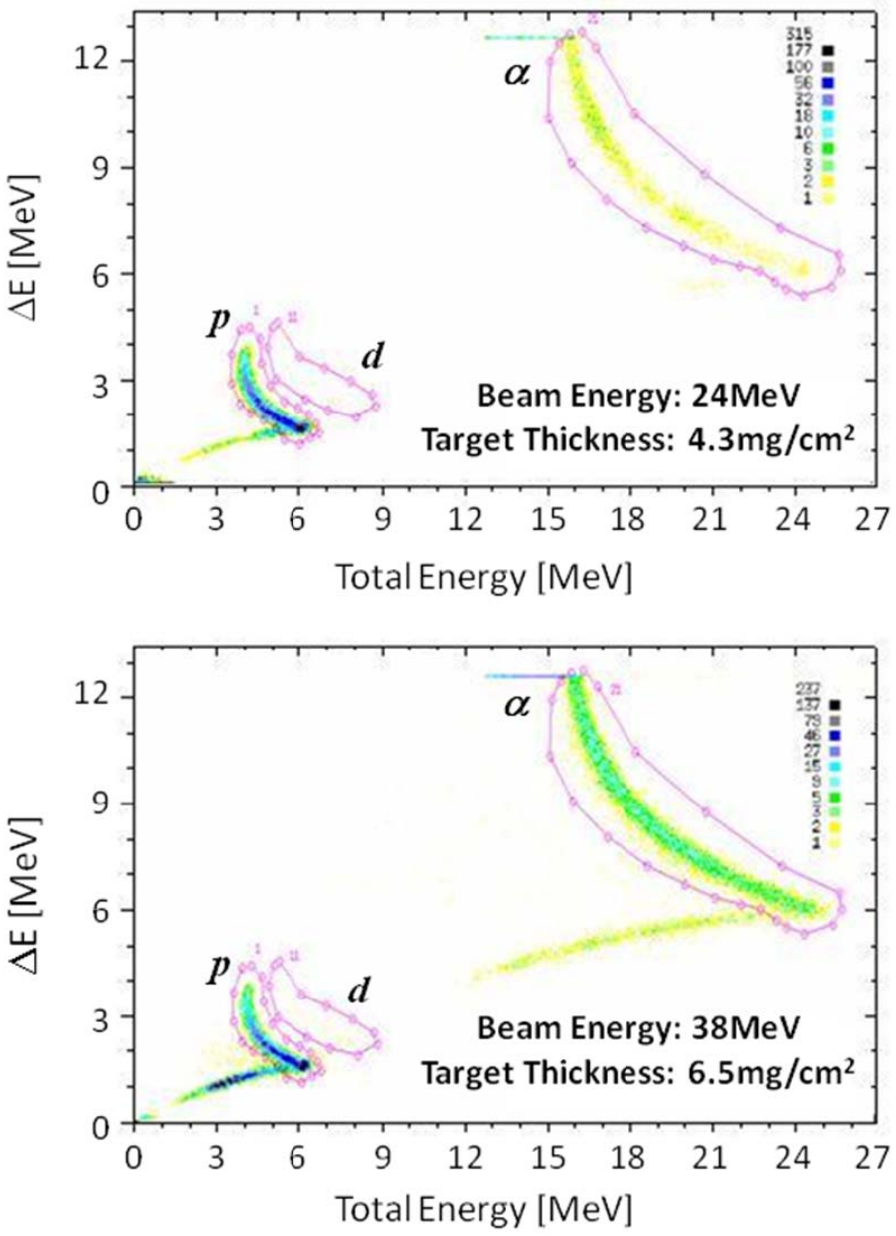

Figure 5.3. ΔE-E correlation plots of signals from the silicon telescope indicated in figure 5.2. Several groups of particles can be readily identified, corresponding to protons, deuterons and alpha particles originated in the reaction of the ^{12}C beam with both the hydrogen and carbon nuclei present in the targets.

Compound-nucleus reactions occur if the reaction mechanism involves many degrees of freedom in the combined projectile-target system at close contact, which is not the case when the collision partners are both light nuclei. When a light low energy nucleus combines with a heavier nucleus, narrow isolated resonances in the reaction cross section as a function of the incident energy are generated (e.g. $^{12}C + p$). When both partners are heavy nuclei (e.g. $^{12}C + ^{12}C$), the complexity of the compound nucleus becomes so high that statistical methods are required. For the sake of completeness, we emphasize that direct measurements of the lifetimes of the relevant resonances in ^{13}N suggest a strong suppression of the compound-nucleus mechanism [Ere 86].

Let us consider now the ^{12}C-^{12}C reaction. In this case, the reaction energy in the center of mass system corresponds to half of the energy in the laboratory system, which is much higher energy than for the proton collision case. That energy, combined with the massive projectile and target is enough to populate regions of relatively high angular momentum and excitation energy in ^{24}Mg, the compound system from which particles are evaporated. In other words, the ^{12}C-^{12}C system undergoes a fusion-evaporation reaction. It turns out that in the energy regime explored by our experiments, the evaporation of protons and alpha particles can account, at least qualitatively for the observed spectra.

Figure 5.4 shows the projection of the banana gates from figure 5.3 on the total energy axis. The upper panel shows a comparison between the spectra measured at the two different beam energies. Spectra have been normalized with respect to each other by taking as reference the maximum height of the resonance peak at E≈6.14 MeV. The position of such peak corresponds to the 3502 and 3547 keV levels in ^{13}N. Notice that both spectra exhibit an artificial gap between 6.5 and 15.5 MeV, which is consequence of 1), punch-thru in the silicon detectors and 2), the lack of information from alpha particles stopped in the ΔE detector (E was the trigger). We draw conclusions from this graph and figure 5.3, namely:

1. Only protons contribute to the low energy part of these spectra (below the resonance), while alpha particles are responsible for the high energy part (above 16 MeV).
2. If our normalization condition matches the experiment[14], then the energy distribution of the protons below the resonance remains unchanged. Since the thick target technique guarantees that the cross section for elastic scattering is the same at the two bombarding energies explored, this means that the energy distributions of the protons from the statistical decay of the compound

[14] This is equivalent to the requirement that the combined probability for the emission of a 6.14 MeV proton in the ^{12}C-p and ^{12}C-^{12}C reactions are the same at bombarding energies of 24 and 38 MeV.

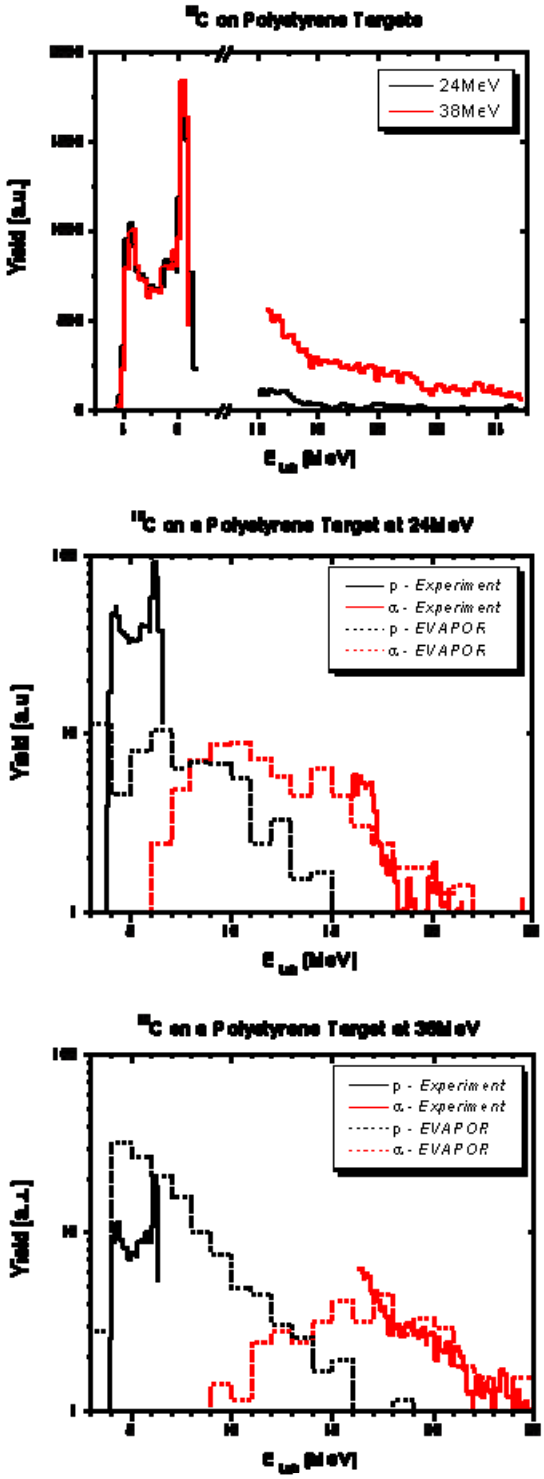

Figure 5.4. Measured and estimated particle spectra from nuclear reactions between ^{12}C beams and polystyrene targets. The solid histograms correspond to our experimental data, whereas the dashed lines represent *EvapOR* calculations.

nucleus are identical within the statistical error. Even if our arbitrary normalization condition were not satisfied by the experiment, such proton distribution would still be flat.

3. If the normalization condition is satisfied, the production of alpha particles above 16 MeV is greatly enhanced upon increasing the energy of the reaction from 24 to 38 MeV.

Based on these considerations the contributions from the fusion-evaporation reaction $^{12}C + {}^{12}C$ can be separated from the ^{12}C-*p* elastic scattering. Moreover, at low energies it would seem that only the elastic scattering channel is important, while at energies above 10.9 MeV the kinematics of the reaction ensures that no elastically scattered protons are to be found. In order to test the validity of these assertions, let us examine the central and lower panels from figure 5.3. In those graphs, experimental data are compared with predictions of production yields for decay products of the compound nucleus in the ^{12}C-^{12}C reaction at the two energies of interest. The calculations were performed using the code *EvapOR* [Bee 09] and the spectra were renormalized in such a way that the total number of counts measured for each alpha distribution matches the corresponding calculated value in the same energy range. Very different relative proton yields are predicted for the reactions at 24 MeV and 38 MeV. Since the scarce level density of light nuclei at low energies presents a challenge to statistical model predictions, *EvapOR* was used merely as a tool to provide information about the shape of the evaporated spectra. For example, Jewett *et al.* recently searched for excited states in ^{22}Mg using the reaction $^{12}C(^{12}C,2n)^{22}Mg$ at HRIBF [Jew 07]. They reported that *EvapOR* overestimates the yields for the emission of protons and neutrons by at least one order of magnitude in the ^{12}C-^{12}C system at 50 MeV. The similarity of that work with our case is one more argument in favor of neglecting the proton contributions from ^{12}C-^{12}C reactions to the spectra from the polystyrene targets in the low energy regime. By the same token, identification of alpha particles can be directly done by considering the high energy part of the spectra above the kinematical limit imposed by the inverse elastic scattering of protons by ^{12}C. Nevertheless, it should be pointed out that if the polarized target is to be used at higher energies, precise identification of fusion-evaporation events should be accounted for, as in general, for a given energy there could be a significant contribution from reactions with both the hydrogen and carbon nuclei from the target.

5.2.2 Proton Angular Distributions

Given the cleanliness of the spectra, the higher beam energy, and some constraints from our experimental facilities (e.g. parameters of operation of the cyclotron at PSI), we chose the reaction at 38 MeV to test our polarized target. Since the contribution from alpha particles from the reactions with the ^{12}C in the target can be readily isolated from the protons, we decided to study the proton spectra from unpolarized

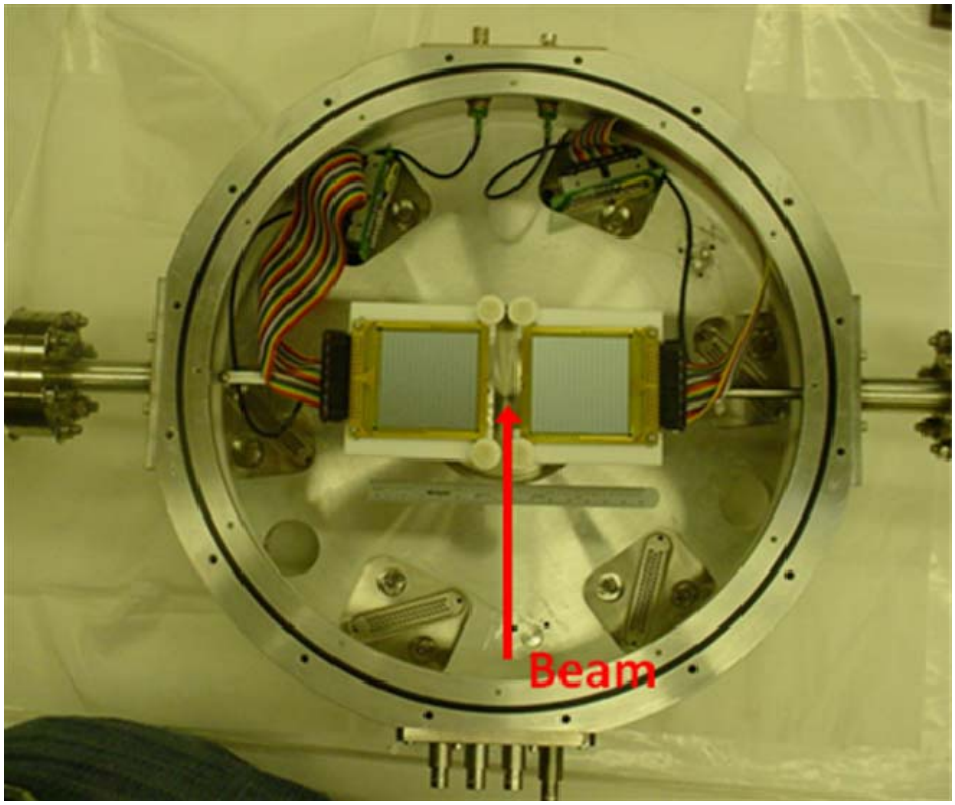

Figure 5.5. DSSDs used for the detection of protons from a polystyrene target at a bombarding energy of 38 MeV. Each 5 cm x 5 cm DSSD is mounted on a retractable feedthrough and consists of 16 + 16 independent strips, resulting in a large solid angular coverage and 256 pixels of detection per telescope.

polystyrene targets in more detail by using a dedicated setup with a much more restricted dynamic range for the detection of particles but with a large angular coverage and granularity. We used a 6.25 mg/cm^2 polystyrene foil doped with TEMPO and the simple Silicon telescope from figure 5.2 was replaced by a set of two telescopes. Each telescope consisted of a 5x5 cm^2 Double Sided Silicon Strip Detector (DSSD) with average thickness of 103 μm, backed by a 1 mm thick, single pad, 5x5 cm^2 Silicon detector. Each DSSD, in turn, has 16 horizontal strips and 16 vertical strips, which provided a total of 512 pixels of detection. The telescopes were carefully aligned with a theodolite. They were mounted 27 cm behind the target on either side of the beam axis and allowed us to measure the energy of protons emitted at laboratory angles between 2.5° and 13.9° in the horizontal plane. Figure 5.5 shows a photograph of the two telescopes employed as they were placed in the detection chamber, which was electrically insulated from the rest of the beam line.

The results from these measurements are contained in figures 5.6 to 5.9. The first figure shows the ΔE-E correlation plots obtained during the measurements, while the second shows the total energy spectra in the laboratory system. Most of the events that appear in the ΔE-E correlation plots correspond to protons hitting, although there might be a small amount of deuterium that could not be resolved[15].

The resonance around 6 MeV in the laboratory system is clearly observed in figure 5.7. The off-resonance cross section is essentially flat and the sharp drop in the yield at energies above 10 MeV is due to the kinematical end point of the binary scattering. Notice that the fusion-evaporation events from the ^{12}C in the target observed at even higher energies are more than one order of magnitude weaker than the elastic scattering channel, in agreement with our former assessment.

The same results viewed in the center of mass system are shown in figure 5.8. It is remarkable seeing in this graph how angular distributions of excitation functions have been measured in a single experiment, with a single bombarding energy and under equal conditions, which effectively reduce systematic errors that might be present in conventional thin target experiments. From this figure one is tempted to conclude that there is some angular dependence on the cross section at the energy resonance. However, our data are consistent with a flat cross section within the statistical error.
Complementary to our measurements, we recently realized that the Ion Beam Analysis (IBA) community has made available a very useful tool called *SigmaCalc* to predict excitation functions of cross sections of light ion reactions in the full angular range [Sig 08]. Based on a large data base from reaction observables and on Optical model, S-matrix, and R-matrix calculations, Gurbich developed an integrated scheme to evaluate low energy cross sections of relevance for IBA [Gur 08]. Although our experimental results agree well with those of *SigmaCalc*, the latter do not exhibit any significant angular variation in the range of interest. Apart from the obvious value for us, *SigmaCalc* might be relevant to find strong synergy between fundamental studies in nuclear structure and astrophysics and applied science.

The final remark is concerned with the quality of our spectra as compared with thin target spectra. Figure 5.9(*a*) shows two of the measured spectra in the center of mass system compared with a high quality spectra obtained with a thin, 20 μg/cm^2, ^{12}C target in normal kinematics by Eremin *et al.* [Ere 86]. Although the shapes of the curves are in agreement with each other, the dip in the low energy side of the

[15] The poor resolution of these silicon telescopes comes from the surprisingly large non-uniformity in the thickness of the DSSDs. However, we were able to study and correct for those effects by using the information available from the 3.50 and 3.55 MeV resonances in ^{13}N. See [Dav 01] for more information on non-uniformity effects in DSSD's.

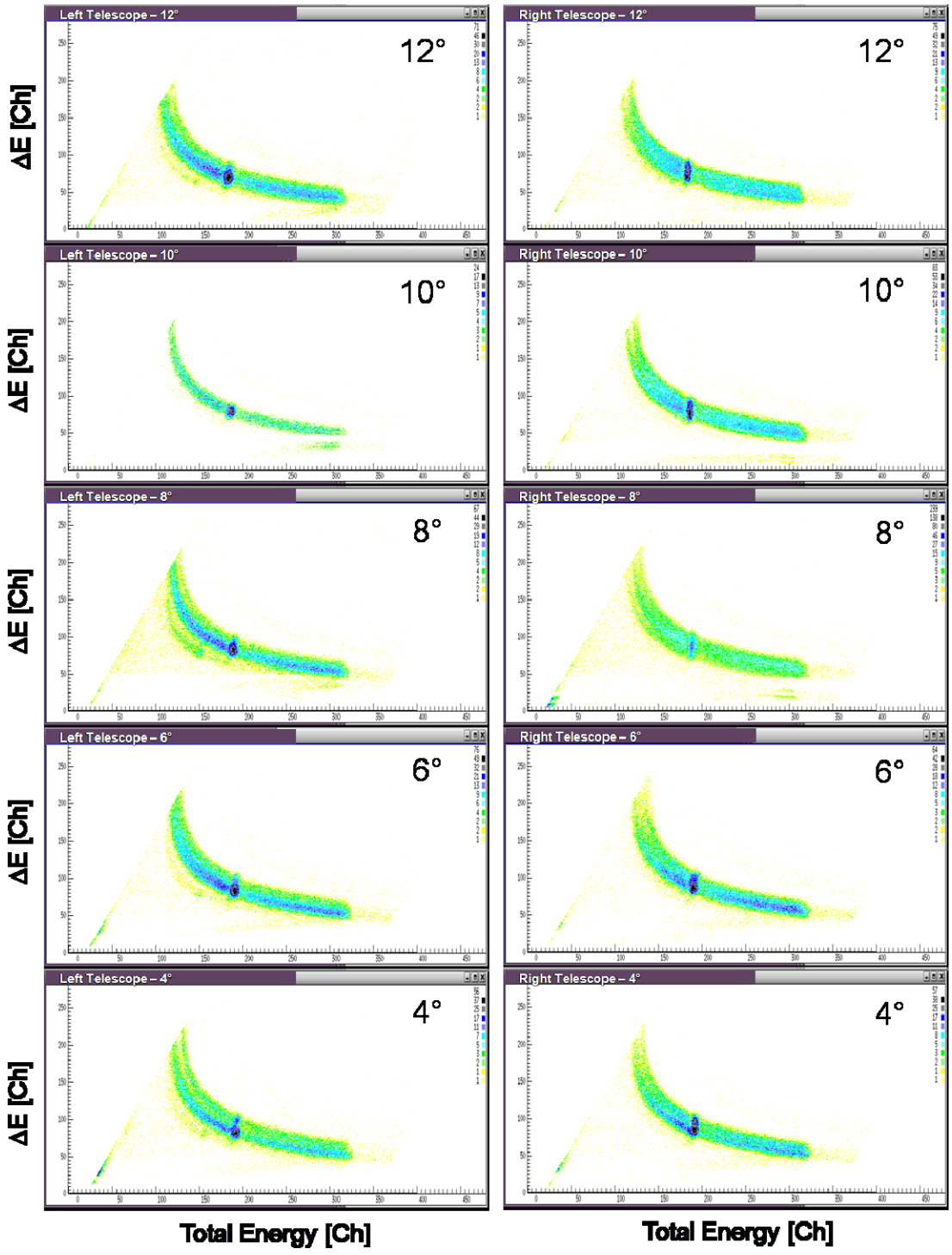

Fig.5.6. ΔE-E correlations measured for several angles in the laboratory system with large area and high granularity silicon telescopes in the $^{12}C+p$ reaction at 38 MeV. The dark area corresponds to the 3.50 and 3.55 MeV resonances.

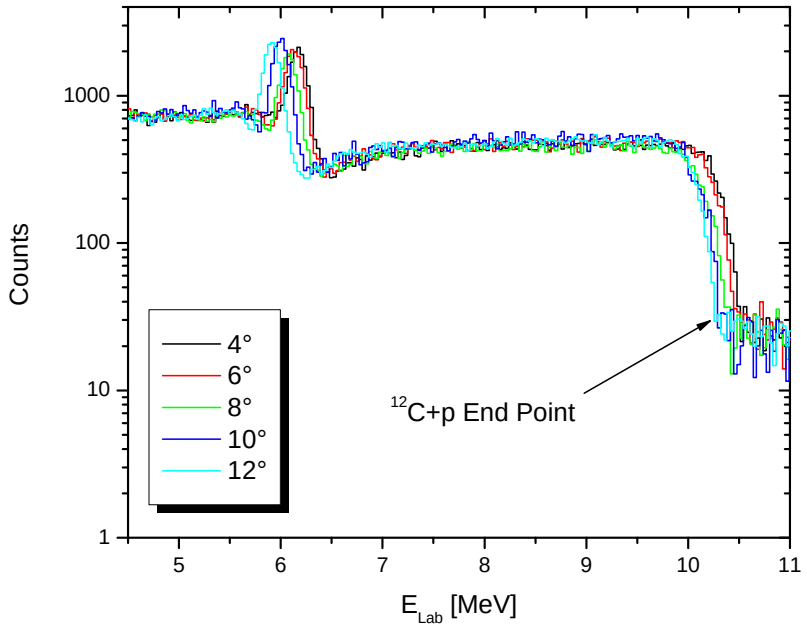

Figure 5.7. Elastically scattered protons from the reaction ^{12}C-*p*. Histograms correspond to different detection angles in the laboratory system.

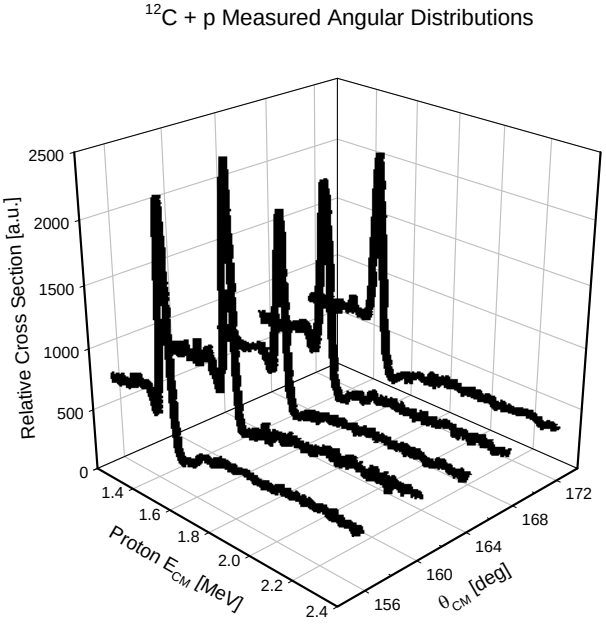

Figure 5.8. Angular distribution of excitation functions for the reaction ^{12}C-*p* taken in a thick target experiment with a single bombarding energy.

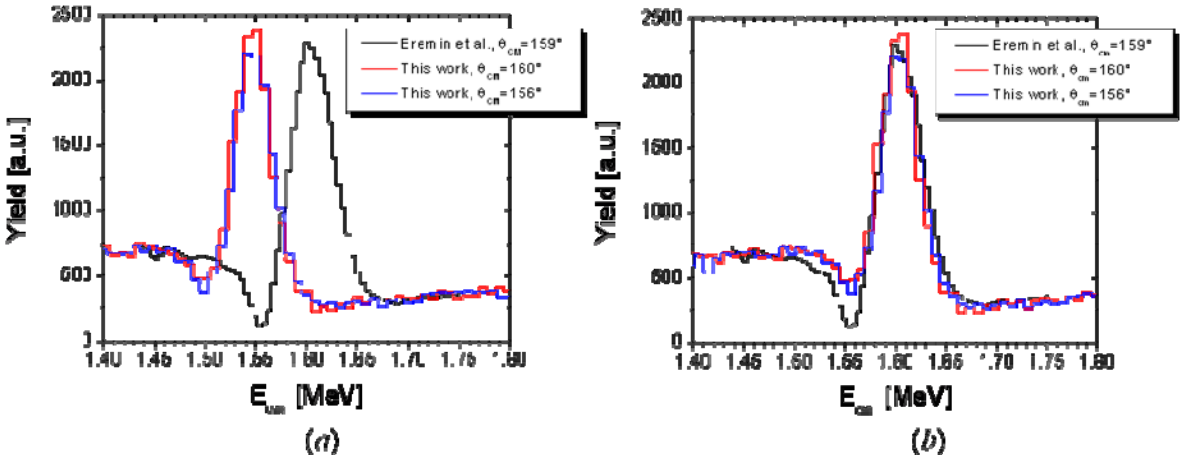

Figure 5.9. Comparison of the excitation functions of cross section obtained with a thin target [Ere 86] and using the thick target technique (this work). (*a*) No corrections for the energy loss of the recoils in the target were applied. (*b*) After correcting for an average 220 keV energy loss for protons in the target.

resonance is less pronounced in the thick target than in the thin target spectra, perhaps as a consequence of straggling in the target. The main difference between the spectra is that our measurements are shifted toward low energies by ~50 keV in the center of mass. The difference arises due the energy loss of protons as they leave the target. In this case, and for the energy range shown in the figure, *Stopx* calculations [Mil 01] show that protons travel an average of 27.3 μm in polystyrene before reaching the detectors, which corresponds to an average ~220 keV energy loss. In the spectra shown in figure 5.9(*b*) our measurements have been corrected for this energy loss and the agreement is outstanding.

This concludes the description of the preliminary tests for the proof of principle of the polarized target. Later on, in section 5.3.3 we will come back to these results to discuss the analysis of spectra obtained in the magnetic field of the polarized target. For the time being, we will focus on the description of the tests performed with the polarized target system fully assembled.

5.3 Characterization of the Polarized Target in In-Beam Tests at PSI

We decided to pursue the on-line tests of the polarized target using 38 MeV ^{12}C beams from the K=120 Phillips Cyclotron at PSI. We will provide first a complete description of the experimental setup and then we will explain in detail the different stages and the results obtained from the characterization process of the polarized target.

Figure 5.10 contains a diagram and a photograph of the setup, which was mounted in the NE-C Area at PSI. The three constitutive blocks of the setup are the target apparatus, the detection system, and the beam diagnosis station. The setup was optically aligned at room temperature by surveying through a viewport window with a telescope.

The target was mounted (top loaded) on a cylindrical stainless-steel chamber, which was placed on a rotating coordinate table. This permitted fine tuning og the target position in the horizontal plane. While no significant change in this plane occurs after cooling the cryostat, the vertical position of the target becomes greatly affected by the thermal contraction of the cryogenic components. We found that the position of the target shifts approximately 2 mm upwards when cold.

In order to minimize the risks of operation at low temperature, the detection systems were as simple as possible. We chose to work with surface barrier silicon detectors operating at 4 K[16]. In view of the clean proton spectra from elastic scattering reported in section 5.2, we used single stage detectors to measure the energy of the recoils. Two detectors with nominal thickness of 1500 μm were placed behind the target, at ±15° along the 'zero field circle' defined by the geometry of the magnet, and mounted on a sliding guide fixed to the lower magnet half as shown in figure 5.11.

The beam diagnosis station played a central role in guaranteeing RIB-like conditions throughout the tests: We were able to reduce and control the beam intensity between 10^3–10^7 pps[17]. The diagnosis station had three components: a set of beam defining apertures, a sensitive screen made of Al_2O_3:Cr for "high" intensities, and a beam flux monitor for low intensities as described by [Gal 91] operating in pulse mode. The beam defining apertures allowed us to have a 2 mm diameter beam spot from the cyclotron. The Al_20_3:Cr screen was mounted on a retractable linear feedthrough behind an optical window that allowed visual inspection of the beam spot (see section 5.1). The beam flux monitor consists of a fast plastic scintillator foil (BC 400), prepared using the spin coating technique [Wea 96] and with a thickness of ~100 μg/cm^2, centered on one of the focal points of an ellipsoidal mirror that focuses the light originated by the beam on the photocathode of a 2" diameter photomultiplier tube (PMT) situated at the other focus.

[16] There is very little experience reported on the use of this type of detectors at such low temperatures [Msr]. A silicon detector from Canberra designed for cryogenic temperatures was also tested.

[17] Preliminary runs at PSI allowed us to optimize the conditions at the cyclotron and beam transport to generate RIB-like intensities.

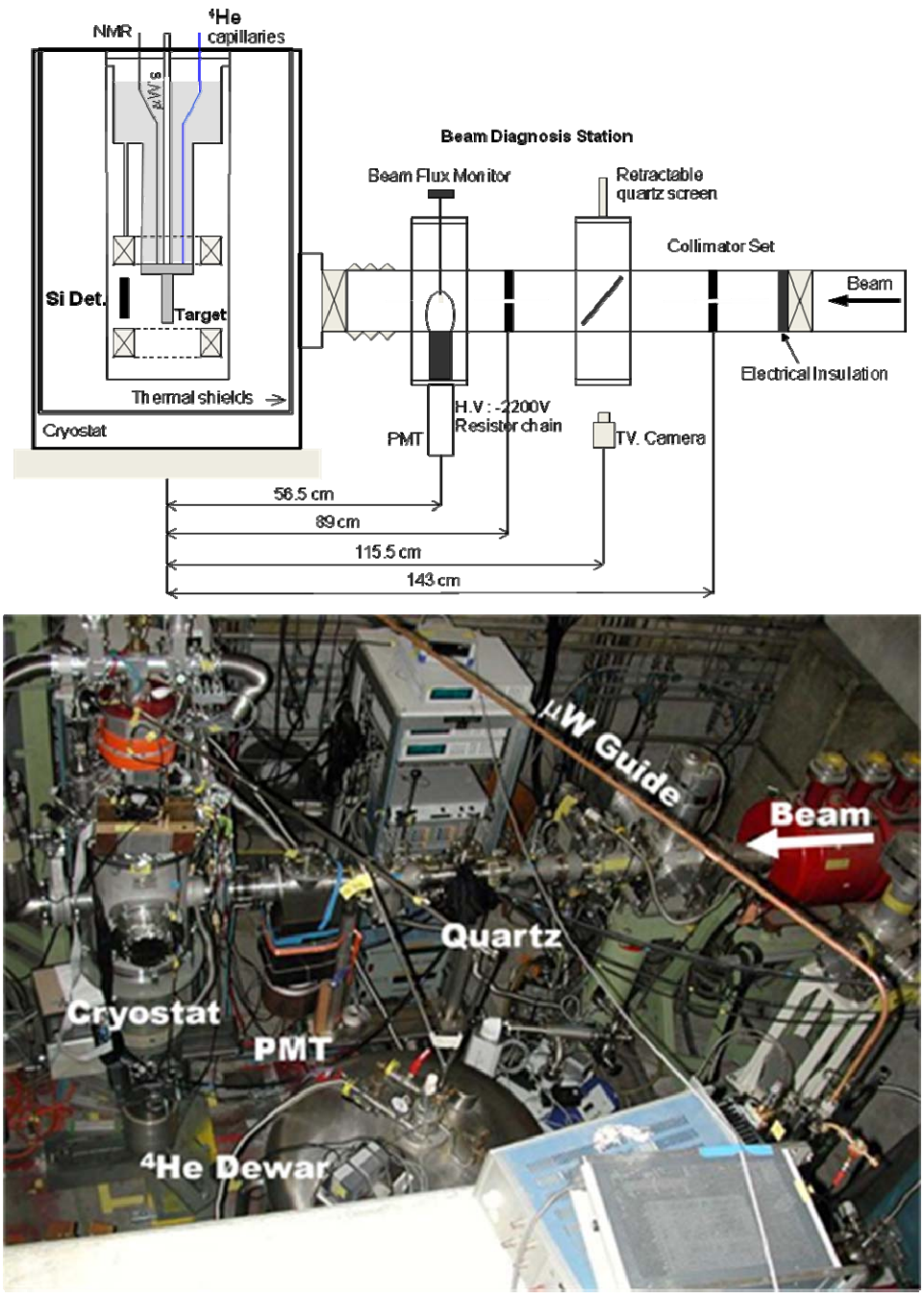

Figure 5.10. Experimental setup used to test the polarized target at PSI. ^{12}C ions were accelerated to 38 MeV by the Phillips Cyclotron at PSI. The beam was collimated by a system of two concentric apertures located at 115 cm and 143 cm from the target. The beam was first optically tuned on a Al_20_3:Cr screen, until its intensity was comparable to the intensity of a typical RIB. During measurements the beam intensity was monitored with the beam flux monitor indicated in the figure [Gal 91].

Figure 5.11. Target chamber and associated charged-particle detectors. Two silicon detectors were mounted on the lower coil of the superconducting magnet, 12 cm apart from the target.

The operation of the beam flux monitor presented challenges of its own. The high magnetic fields required for the polarized target operation precluded placing the beam flux monitor closer to the target. The stray magnetic field has an effect on the trajectories of the electrons across the dynodes, which affects the performance of the PMT (e.g. gain and timing). We reduced significantly the stray field at the PMT location by a three-layer shielding. The standard mu-shield tube [Gal 91] was surrounded by a thick soft-iron pipe which in turn was surrounded by a magnetic shielded case made with high permeability material. By measuring the values of the magnetic flux within the multi-layers with a Hall probe we were able to optimize the magnetic shielding and reduce the field to 50 G.

The counting efficiency of the beam flux monitor depends on several factors such as the energy deposited on the scintillator, the scintillator efficiency, PMT base characteristics, counting rate, and noise levels. We studied its performance under various conditions. Figure 5.12 shows a digitized pulse obtained with a 38 MeV ^{12}C beam. Under these conditions we were able to count up to $4*10^6$ pps, where the PMT saturates. We studied the counting efficiency and the transmission between the scintillator and the target location with the assistance of a small PMT coupled to a ϕ1 cm, 1.5 cm thick CsI(Tl) crystal placed on an identical chamber to the one containing the polarized target. Even with the gold foil from the thermal shields of the target in place we obtained a 100% transmission in the intensity range between 10^3 and $4*10^6$ pps at room temperature. Figure 5.13 shows the counting efficiency of the PMT as a function of the magnetic field of the target. Since for the tests we used a magnetic field of 0.8 T, we corrected the beam flux monitor efficiency accordingly.

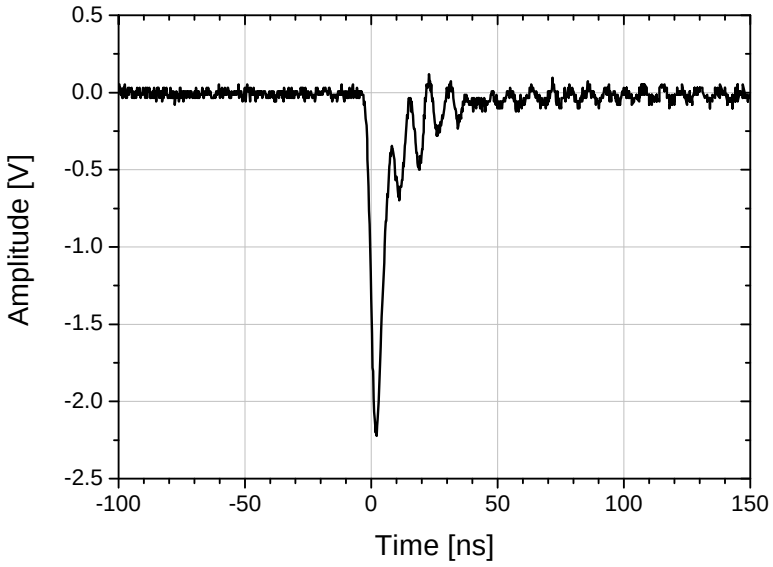

Figure 5.12. Typical pulse from the PMT as a ^{12}C ion is transmitted through the 100 μg/cm^2 thick plastic scintillator. The signal was digitized by a digital oscilloscope at a beam rate of ~10^4 pps.

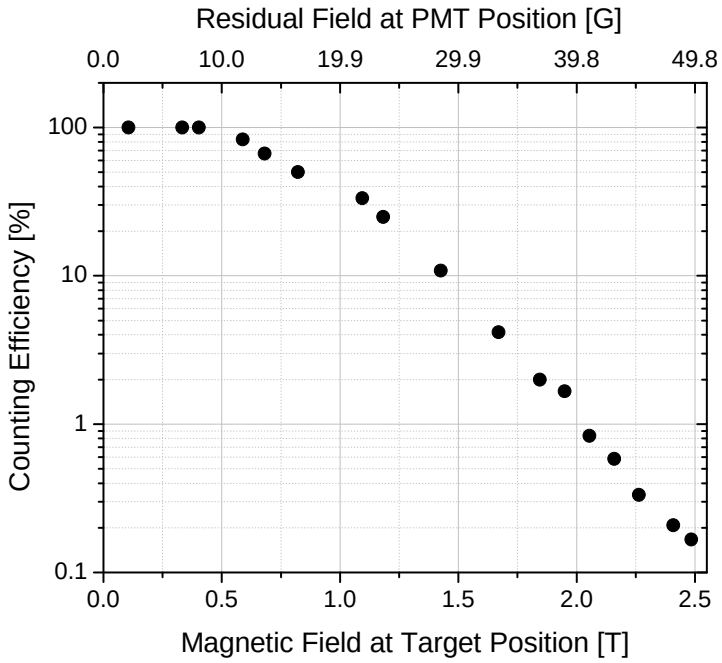

Figure 5.13. Counting efficiency of the PMT as a function of the magnetic field of the polarized target.

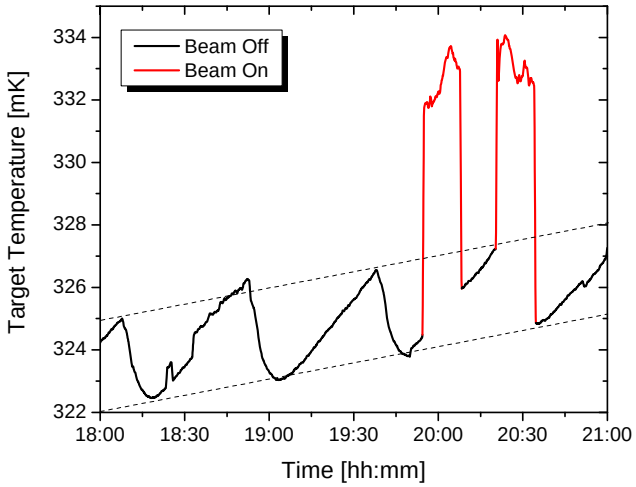

Figure 5.14. Temperature variation of the target cell induced by beam irradiation at 10^5pps. The characteristic oscillatory pattern associated to the filling cycle of the cryostat is observed. The dashed lines are visual guides that indicate that a monotonous increase in temperature is taking place, independently on the presence of beam. Only if the beam illuminates the target a sudden increase in temperature is observed.

5.3.1 Beam Intensity Effects

The irradiation of a polarized plastic target with a beam of heavy ions induces a variety of effects that have a potential impact not only on the level of polarization but also on the operational lifetime of the target. Such effects can be classified into two main categories: reversible and irreversible. Reversible effects are those physical manifestations that disappear more or less instantaneously after the beam is taken away from the target, whereas the irreversible category comprises permanent changes in the performance or in the structure of the polarizable foils.

We identified a single but most important reversible effect; namely, the increase in the temperature of the target cell. It results from the extra thermal load that the beam infringes upon the target. Figure 5.14 shows a portion of the temperature record of the target cell, corresponding to the operation of the target before, during and after beam irradiation. Once the beam hits the target, the temperature increases rapidly within 30 s, then it behaves in a smooth way, following the changes in the beam intensity, and finally, when the beam is taken away, the target cell reaches its original temperature in ~30 s. The reversibility of this process is confirmed by the two irradiation cycles displayed in the figure. Notice that the thermal response of the target is rather sensitive to variations in beam intensity and that it only has a relatively

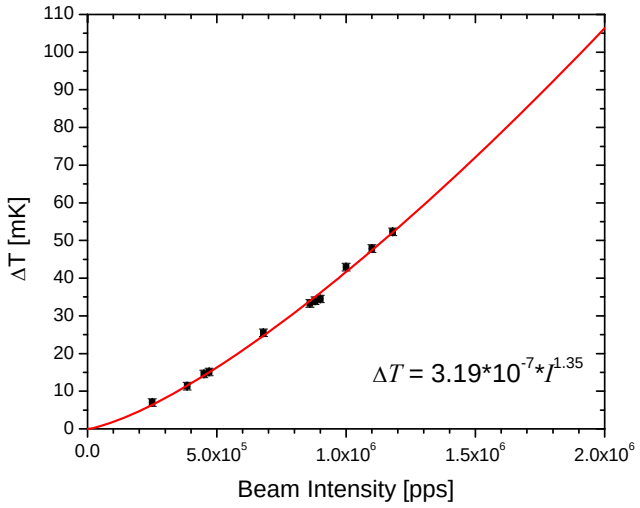

Figure 5.15. Bolometric behavior of the target cell. The red curve corresponds to the fit of the experimental data (black dots). The resulting expression for the beam intensity reaching the target as a function of the increase in temperature from a base temperaure of 225 mK is shown in the graph.

small associated delay. These features indicate that the target behaves as a bolometer, which makes it possible to directly measure sizable beam intensities reaching the target cell.

Figure 5.15 contains the measured equivalence between the increase of the target temperature and the beam intensity indicated by the flux monitor. The red line is a non-linear fit of the experimental data that provides a reasonable estimate of the number of particles hitting the target cell, provided the base temperature of the cryostat is ~230 mK. Although the behavior of the temperature clearly deviates from the linearity of an ideal bolometer, it is conceivable that as the temperature increases, the parameters governing the heat balance in the target cell might drastically change, resulting in the power law expressed by the fit in the figure. We will come back to this calibration when referring to polarization data.

Since the increase in the target temperature can be used for beam diagnostics purposes, it would seem that it is *per se* more of an operational advantage than a drawback. However, it also has a marked impact on the polarization of the target. Figure 5.16 shows the polarization of the target operated in frozen spin mode as a function of time, together with the associated temperature of the target cell. The effects of

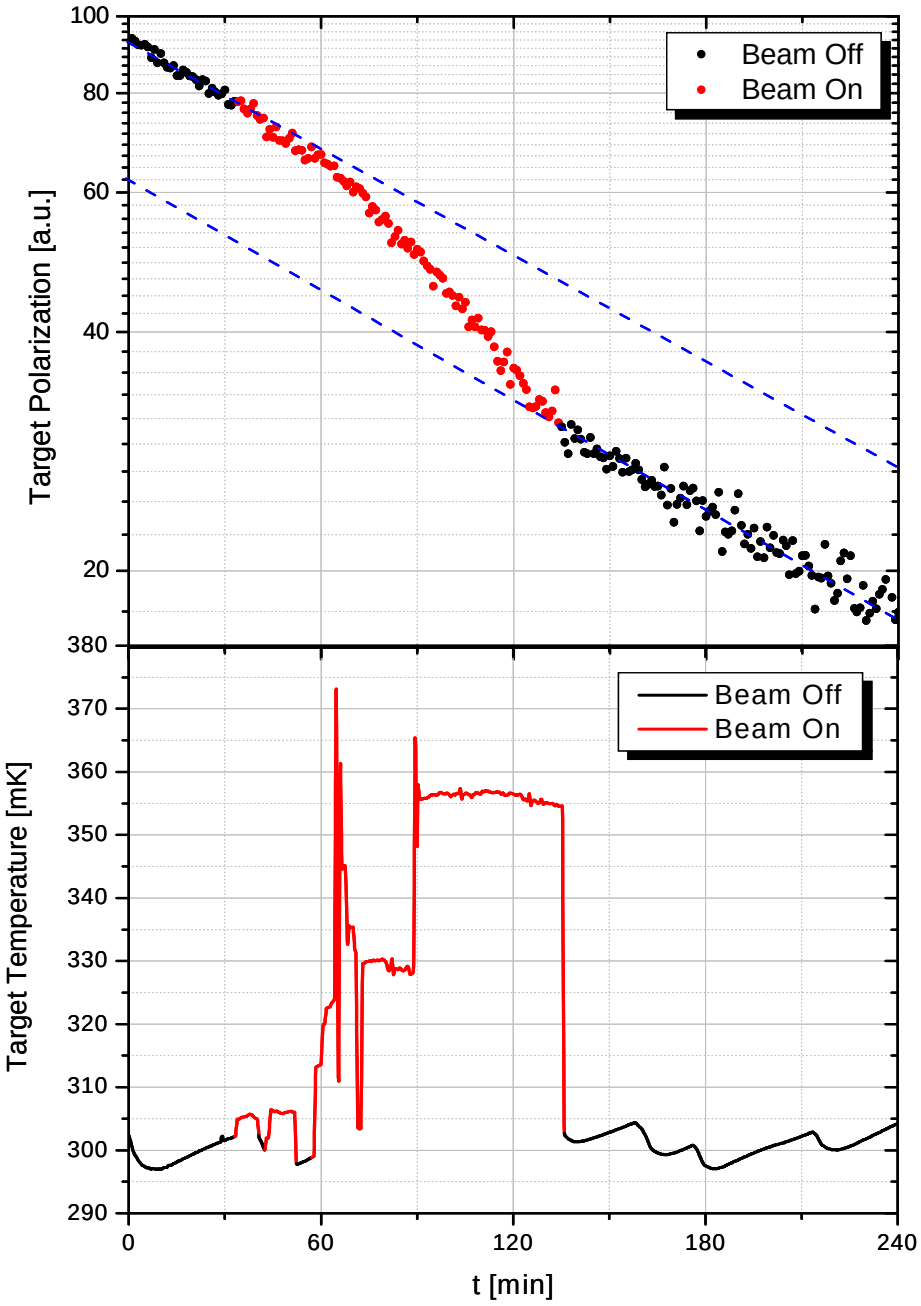

Figure 5.16. Instantaneous effect of the beam on the polarization of the target. The upper panel depicts the relative polarization record of the target before, during, and after beam irradiation. The blue lines are merely visual guides to indicate that the slope of the curve is identical before and after irradiation. The lower panel contains the temperature record of the target chamber for the same period of time.

switching the beam on and off are clear: The rate of depolarization increases with the beam intensity. For the case shown here, at the field of 1.2 T, the maximum beam intensity was ~$1.2*10^6$ pps, which increases the temperature by ~55 mK and reduces the relaxation time of the target from (114±5) min to (40±7) min. In spite of this difference, the thermal effect on the relaxation time of the target is not a fundamental issue for experiments with most RIBs available, as their intensities are seldom as high as 10^6 pps. As a matter of fact, by looking at the beginning of the red curve in the upper panel of figure 5.16, one can see the small effect of irradiation at the more customary rate of ~$3*10^5$ pps (ΔT~7 mK).

In contrast with the rapid time scale of the thermal effect we just described, irreversible effects occur during a longer period of time (in the range of typical RIB intensities) and their manifestations are cumulative in nature, in the sense that they are determined by the total dose absorbed by the target and not by the beam rate. The two main irreversible effects are the erosion of the target material by the beam and the creation of new paramagnetic centers. The strength of these effects establishes two key figures for the operation of the target; namely, the maximum amount of current it can withstand before it is burned and the practical beam intensity limits for which depolarization effects are low enough for long experiments to take place.

Burning of the plastic targets might occur due to thermal stress and structural damage infringed upon it by the beam. Figure 5.17 shows the photograph of a foil on which the beam has left visual marks. The intense marks were inflected after ~1½ h of continuous irradiation at room temperature and rate of ~10^7 pps (~$5.4*10^{10}$ ions), which according to our experience is the maximum practical dose to be delivered locally (by a well focused, tight beam) before burning the target. By using the ϕ2 mm beams from the Phillips cyclotron, we were able to deliver an estimated dose in excess of 10^{11} ions to the cryogenic target. This result ensures that the risk of burning the polarized target by irradiation at realistic RIB intensities can be overcome, either by defocusing the beam or by moving the target to a fresh spot every certain time. Moreover, for a thinner target, where the beam can pass through avoiding the Bragg peak, the energy delivered to the target will be smaller, which guarantees that the quoted beam intensities are lower limits for the safe operation of plastic targets.

No physical damages on the target were observed at low temperatures. In that case, cooling of the target is expected to reduce the beam effects.

Figure 5.17. Evidence of destructive effects of the beam on thick polystyrene targets at room temperature. The most intense markings correspond to a beam intensity of ~10^7 pps maintained on target during ~1½ h.

The second source of irreversible effects is much more subtle. Ionizing particles interacting with matter create free electrons and radicals that behave like paramagnetic centers. If recombination proceeds in a slow manner and the amount of electrons created is significant, the dipolar coupling between them and the original DNP centers in the target results in a faster relaxation time, thus impending the polarization capabilities. Although the heavy ion intensities considered are low, the ionizing power can be considerable and therefore it was not obvious how important this effect could be. Measurement of relaxation times before and after irradiation offers a simple way to quantify this effect. Figure 5.18 illustrates such relaxation curves before and after irradiating the target with more than 10^{11} ions. No change is observed in the extracted relaxation times, which ensures that depolarization effects due to the creation of free radicals in our targets are negligible in the range of intensities typical of RIBs and during the course of a typical RIB experiment.

5.3.2 Effects of ^{4}He in the Target Chamber

Another aspect of the proof of principle was to test the overall effect on a resonance spectrum of adding a superfluid ^{4}He film to cool the target. This information is required to optimize the target design in such a way that sufficient cooling is provided while minimizing the amount of material along the paths of beam and recoils. For this test, the chamber was evacuated before starting to cool down the cryostat, but once the temperature was low enough for ^{4}He to become superfluid, 0.26 cm^3 STP of ^{4}He gas were admitted into the chamber, taking ~4½ hours to fully condense this quantity. The recoil energy spectra measured before and after condensation appear in figure 5.19. Although the resonance peak clearly appears in both

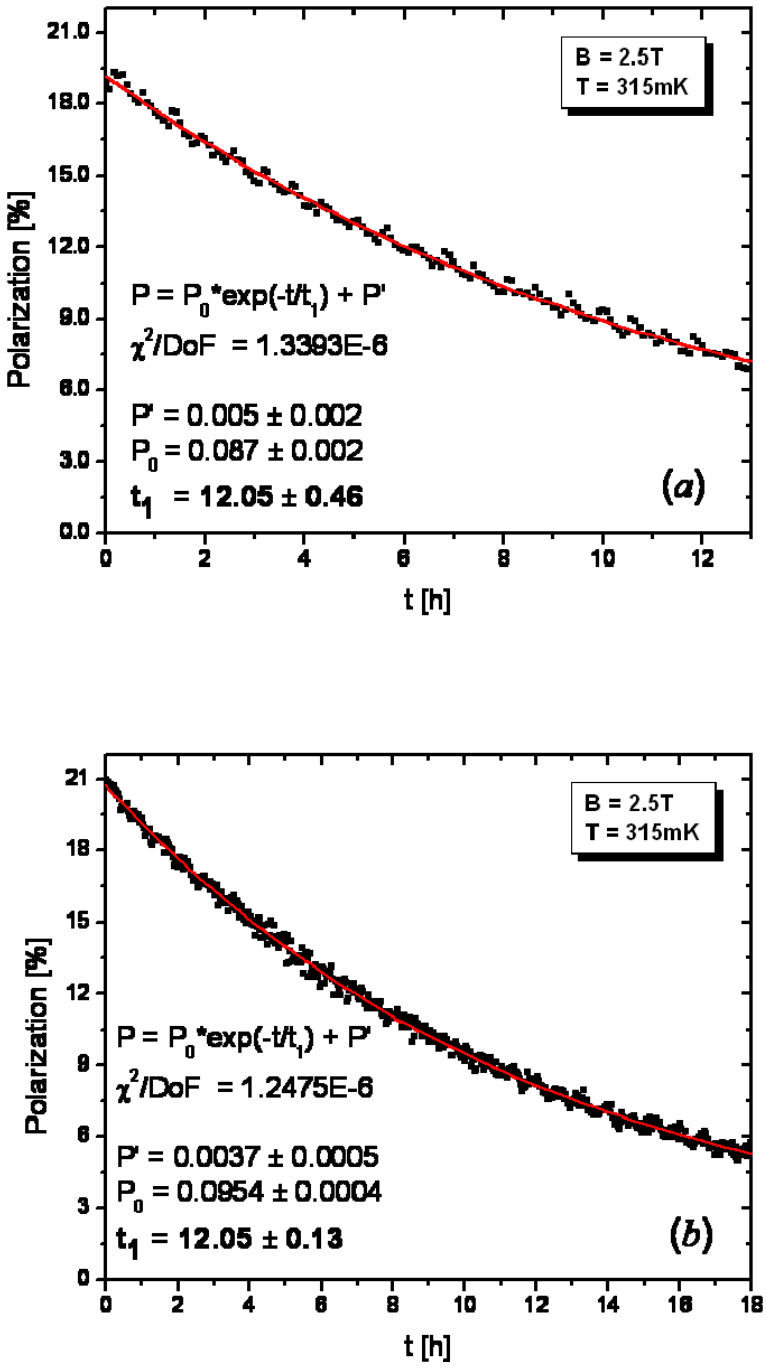

Figure 5.18. Polarization relaxation curves before (*a*) and after (*b*) beam irradiation. No appreciable change in the relaxation time t_1 is observed due to beam effects after irradiating the target with more than 10^{11} ions of ^{12}C.

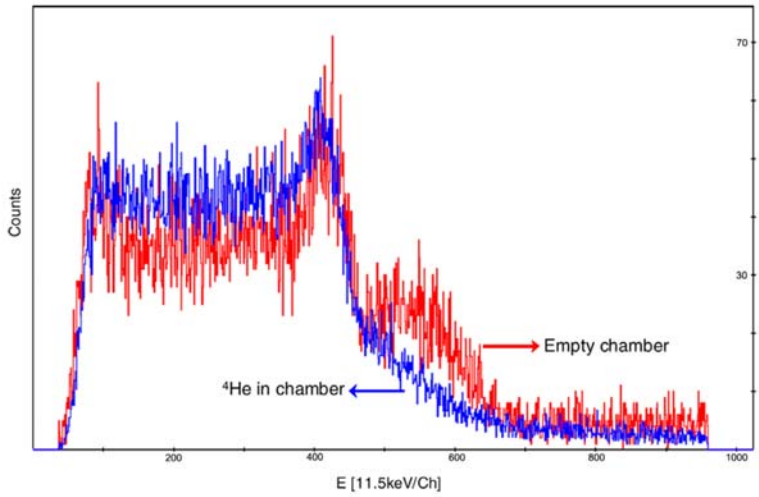

Figure 5.19. Effect of superfluid ^{4}He inside the target chamber. The spectra from the ^{12}C + $[CH]_8$ reaction were taken using a 14.4 mg/cm^2 polystyrene target in a magnetic field of 0.4 T. The nominal thickness of the superfluid film was 0.3 μm.

spectra, their shape is different, especially at high energies. Considering that the thickness of the target is ~14.4 mg/cm^2 and based on the information obtained in the HRIBF tests, it is clear that the high energy bump in the empty chamber spectrum corresponds to alpha particles, that now appear closer in energy to the protons due to severe energy losses in this very thick target. Once the chamber is filled with superfluid Helium, the energy distribution of alpha particles spreads towards lower energies and becomes more homogeneous due to elastic collisions with the He nuclei present in the chamber. More importantly, the proton distribution is not significantly affected: The centroid of the peak from the ^{4}He filled chamber is shifted towards lower energies only by 1.7% compared to that of the empty chamber spectrum. These results demonstrate that cooling through a superfluid film is a suitable mechanism as was proposed by van den Brandt *et al.* [Bra 96] and could be used for polarized targets for heavy ion reactions.

5.3.3 Polarization Observables

In this section we describe the first measurement of polarization observables performed with our polarized target. Figure 5.20 illustrates the variation in the shape of the spectra when the target is operated in frozen spin mode at different field values. The resonance peak in ^{13}N is clearly seen. One can also see a steady increase in the energy of the resonance peak with the field up to 0.8 T. Due to the inverse kinematics, the recoils emitted at angles closer to zero degrees are more energetic. As the magnetic field increases, the protons from the resonance that (at zero magnetic field) would reach the detector will move

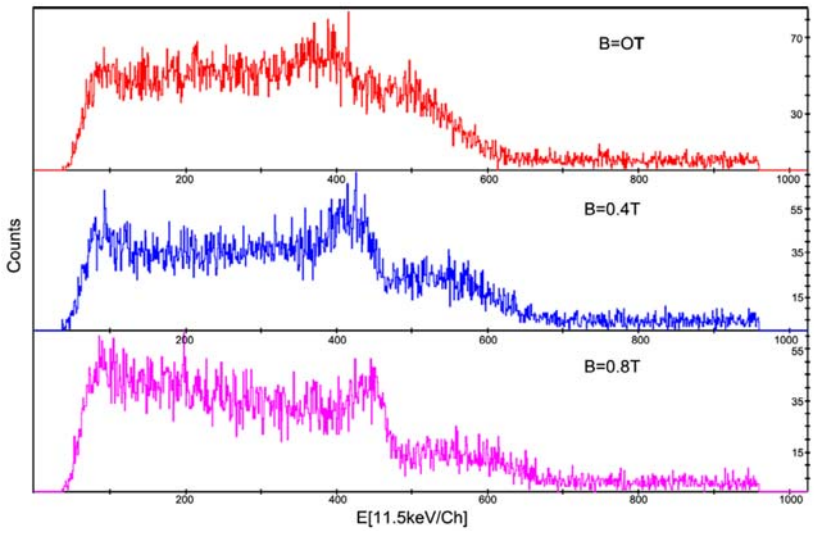

Figure 5.20. Effect of the magnetic field on spectra from a 14.4 mg/cm^2 polystyrene target. The peak around channel 400 corresponds to the resonances at 3.50 and 3.55 MeV in ^{13}N.

into curved trajectories to different angles. There will be a certain magnetic field value for which the energy of the resonance will reach a maximum, corresponding to the protons emitted at zero degrees hitting the detector.

Based on the spectra from figure 5.20 and on the relaxation times reported in chapter 4 we decided to operate the polarized target in frozen spin mode at 0.8 T. In addition, we used the same 6.25 mg/cm^2 polystyrene foil doped with TEMPO ($2*10^{19}$spins/cm^3) used for measuring the proton angular distributions from section 5.2.2. It ensures practically alpha-free recoil spectra in the dynamic range of the detectors (~4.5-11 MeV). The last test was performed at a base temperature of the target of 225 mK. Protons were dynamically polarized at 2.5 T in two cycles of positive and negative polarization, as shown in figure 5.21. The maximum polarization achieved was 23% and it was obtained at the beginning of the first cycle after ~8 h of microwave irradiation, while for the rest of the test we polarized up to 20%. Relaxation of the field took place within 30 min, after which the polarization started to be monitored with an NMR circuit tuned at 34.22 MHz and beam was put on target. Irradiation at $2*10^6$ pps proceeded for ~24 min, with polarization levels steadily decreasing from ~18% to ~8.5%.

Due to the asymmetry introduced by the field, only one of the Si detectors provides meaningful data during a single measurement (right detector for the first cycle, left for the second). Hence, in order to

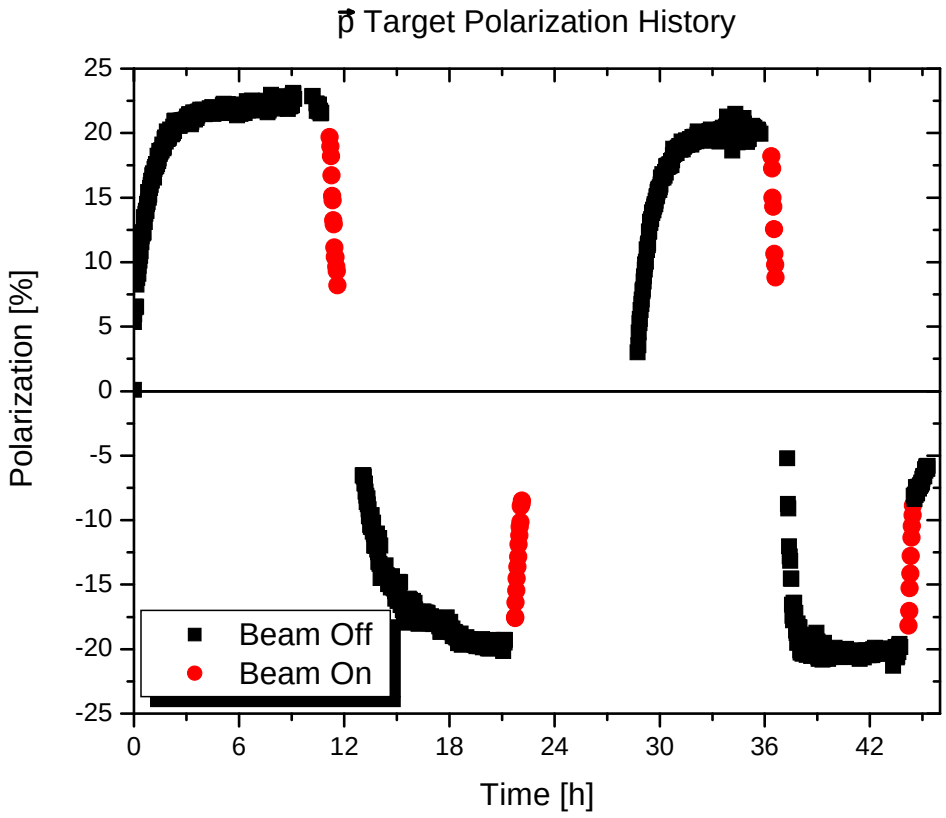

Figure 5.21. Polarization history of the polarized target. The size of the points represents the estimated polarization error. Spectra were taken while sampling the polarization in real time.

explore possible systematic errors due to the field, we inverted the polarity of the magnetic field after the first polarization cycle. The resulting spectra have been normalized according to the beam intensity and are shown in figure 5.22. Thanks to the NMR signal, the magnetic field was fixed to the nominal frozen spin value within ~0.05 MHz (~10 G) during each polarization cycle. As a result, the detection geometry remains practically invariant for each cycle, canceling all detection efficiency issues when comparing scattering from the spin up and spin down states. The two sets of measurements shown in the figure clearly indicate that scattering from the spin down state is preferential or, in other words, that the excitation function of analyzing power for the ^{12}C+p reaction is negative at large angles. This is in agreement with the data reported in figure 5.1 [Phi 59].

In spite of the features discussed above, there are differences between the spectra from the two cycles. One factor that might be partially responsible for this is that spectra from each cycle were measured with separate detection systems (including different data acquisition systems). However, the most significant difference in experimental conditions between the two sets of measurements is the polarity of the magnetic field. If small misalignments exist in the experimental setup, a change in polarity results in differences in the magnetic field felt by the charged particles as they travel to and from the target. In the next section we will show that the shape of the energy spectra of the recoils is sensitive to the alignment of the target.

5.3.4 Trajectories of Charged Particles in the Magnetic Field of the Target

The trajectory of charged particles can be calculated by integrating their equations of motion in the presence of the magnetic field from the magnet. This requires a precise knowledge of the field and the geometry of the experimental setup. The magnet is well characterized and a detailed field map is available [Kon 07]. With the exception of small alignment issues, the position and dimensions of the different components of the setup are known with precision of ~1 mm. The trajectories are calculated, for a single particle at a time, using an adapted set of GEANT4 routines originally developed for applications in μSR experiments [Sed 08, Shi 08]. The program propagates charged particles in a medium (including vacuum) using a Runge-Kutta solver. Interactions with the materials in the geometry leading to energy loss and straggling are also included in the routines. Since GEANT4 is not designed to simulate nuclear reactions, the problem of analyzing a polarized target experiment has been divided into two parts. First we simulate the beam trajectories, from which we extract the position and momentum information of the carbon ions that hit the target. Secondly, we use that information to set up the initial conditions of the recoiling

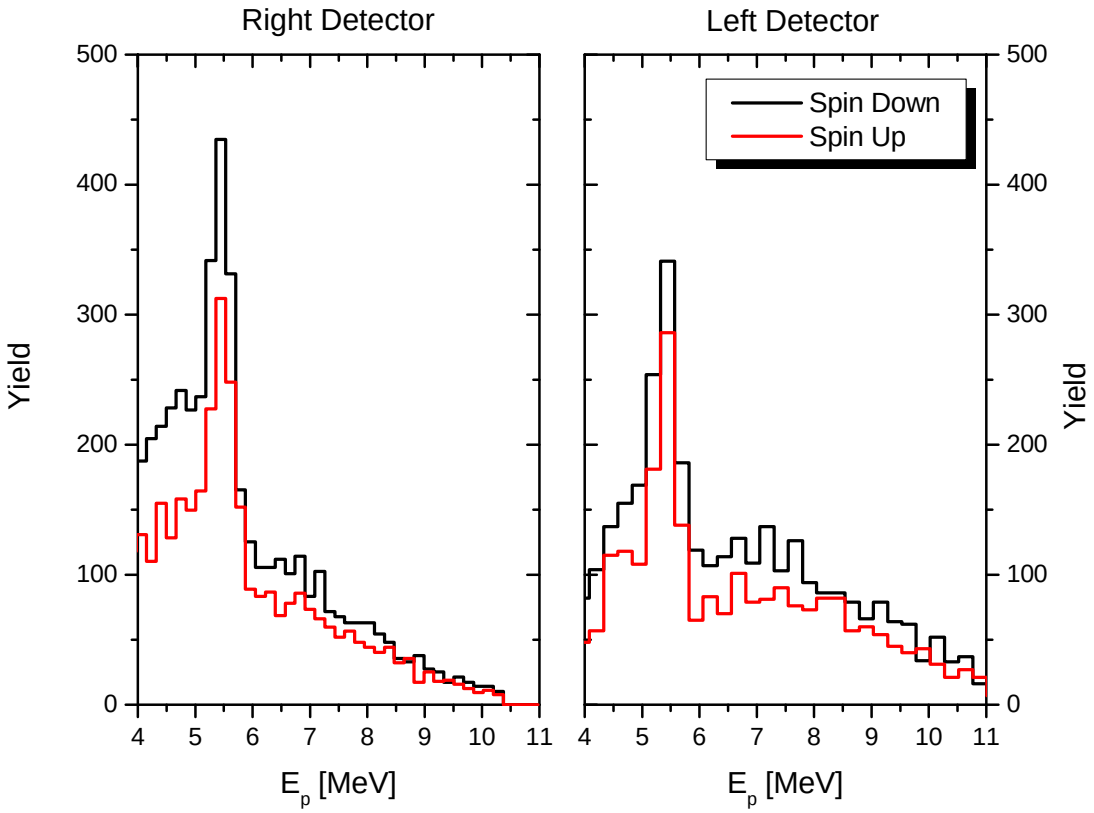

Figure 5.22. Spectra obtained with the polarized target. The spectra are normalized according to the integrated beam intensity delivered to the target, as extracted from the temperature record of the experimental run. The difference in shape between spin up and spin down is due to polarization effects. The difference between the two groups of spectra is likely due to small misalignments in the experimental setup.

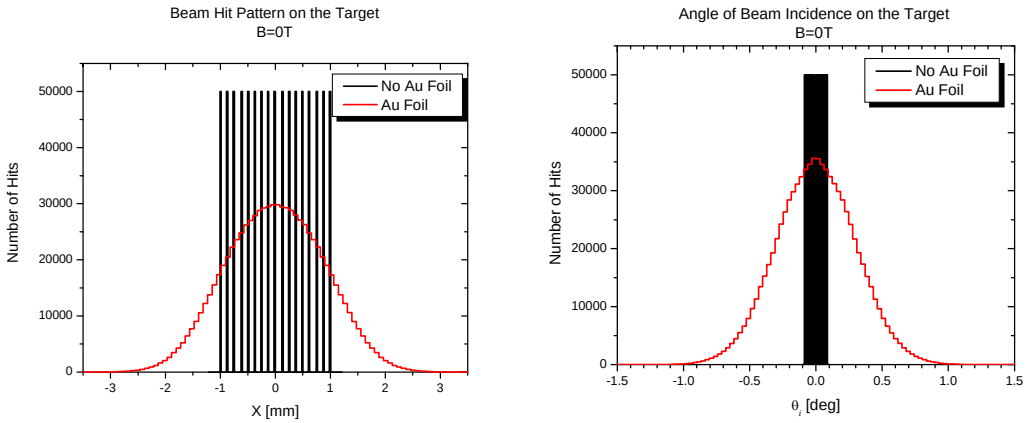

Figure 5.23. Simulation of the beam propagation along the beam line at zero magnetic field. The right hand side graph shows the physical profile of the beam on the target plane, while the graph on the left shows the distribution of angles of incidence on target.

protons. From there, we calculate their trajectories and eventually analyze those that reach the detectors. Examples of input files to the code and typical trajectories are shown in appendix C.

We start our discussion with the simulations of the beam trajectories. We assume an initial distribution of beam particles such as the one shown in figure 5.23. It consists of a uniform intensity distribution within the area defined by the collimators. At zero magnetic field, the angle of incidence with respect to the normal to the target, θ_i, is close to 0° as the collimators do a good job in controlling the divergence of the beam. Using this assumption and propagating the beam through the gold foil that closes the thermal radiation shields of the cryostat, results in the spatial and angular profiles also shown the figure.

Effects due to the gold foil are not only limited to energy loss and straggling. The foil also acts as a charge stripper for the beam. The distribution of charge states after reaching equilibrium can be calculated using the code *CHARGE* [Mil 00] for a 38 MeV ^{12}C beam, as indicated in table 5.1. Using this information, we simulated the trajectories of ions with charge states for similar geometrical assumptions for the beam, but in a magnetic field of 0.8 T. The results are shown in figure 5.24. The centroid of the beam spot is shifted ~5.5 mm to the right at the target position. Besides, the charge states are clearly separated in momentum, resulting in well resolved groups of angle of incidence on the target. The combination of these two effects determines the effective angle of emission of the recoils from the target.

Table 5.1. Equilibrium charge state distribution for a 38 MeV ^{12}C beam passing through a 2 μm thick gold foil.

$q=3^+$	$q=4^+$	$q=5^+$	$q=6^+$
0.1%	9.4%	62.7%	27.7%

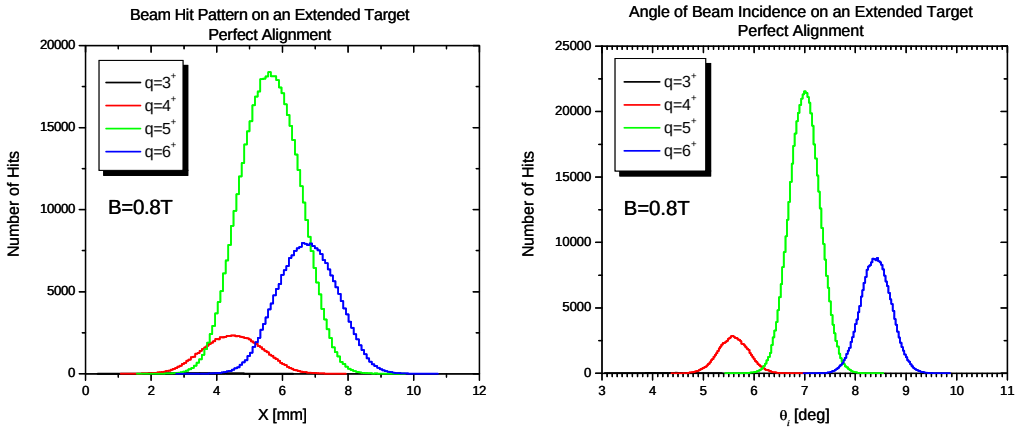

Figure 5.24. Separation of the different charge states of the beam in a 0.8 T magnetic field. The left hand side graph shows the beam profile of the different charge states of the beam as it reaches the target plane. The right hand side shows the correspondent angles of incidence on the target.

Figure 5.24 contains information from all beam particles reaching the plane of the target. However, if the exact dimensions of the target are considered (7*7 mm^2), the position and momentum distributions change significantly (x=0 defines the center of the target). Figure 5.25 exhibits those distributions on the actual target geometry for three different alignment scenarios, while maintaining the same number of incident particles in all cases (50000). Clearly, the hit pattern is very sensitive to alignment, which affects greatly the effective beam intensity reaching the target. As for the angle of incidence, it has a soft dependence on alignment for each charge state, but the relative weight of the states does change significantly. This has an impact on the measured recoil spectra.

Due to the geometry, the initial conditions, and the multiple energies involved, the discussion about the trajectories of the recoils is somewhat different than for the beam. In this case, the goal of the simulations is to determine the shape of the spectra recorded by the silicon detectors at 15°, while discriminating the effective angle of emission of the protons[18]. In figure 5.26 we consider first mono-energetic protons of 6 MeV reaching one of the detectors and emitted from the target according to three sets of initial conditions: Isotropic point source from the center of the target, uniform distribution of protons along the 'x' direction with isotropic emission, and protons emitted following the hit pattern and the profile of the angle of incidence for the perfect alignment beam simulations. From this figure we can conclude that the extended beam spot on the target is responsible for the large effective angular acceptance of the detectors (~6° for 6 MeV protons) and that initial conditions have a strong influence in the determination of the effective angle of emission of protons.

Results from complete simulations of the trajectories of recoils with initial position and direction taken from figure 5.25 are presented in figure 5.27. The initial energy distributions of the protons were taken directly from the data with the unpolarized target reported in section 5.2.2. Notice that different shapes of spectra result from different alignment conditions. Due to uncertainties in the initial beam distribution, we restrain from attempting a fit of the spectra measured at PSI. However, these simulations qualitatively show that if high precision results are needed in experiments at low energy, then a careful assessment of the beam profile should be made in order to analyze the measured spectra. Our results indicate that for a given proton energy, contributions from different angles of emission are to be taken into account. This imposes limits on the angular resolution one can achieve with a certain pixel of detection at a given energy. In the case discussed here, a circular detector with a diameter of 7 mm located at 12 cm from the target offers a resolution of ~6° for 6 MeV protons and ~3° for 10 MeV protons in the laboratory system.

[18] This is the angle at which a proton is emitted in the absence of magnetic field.

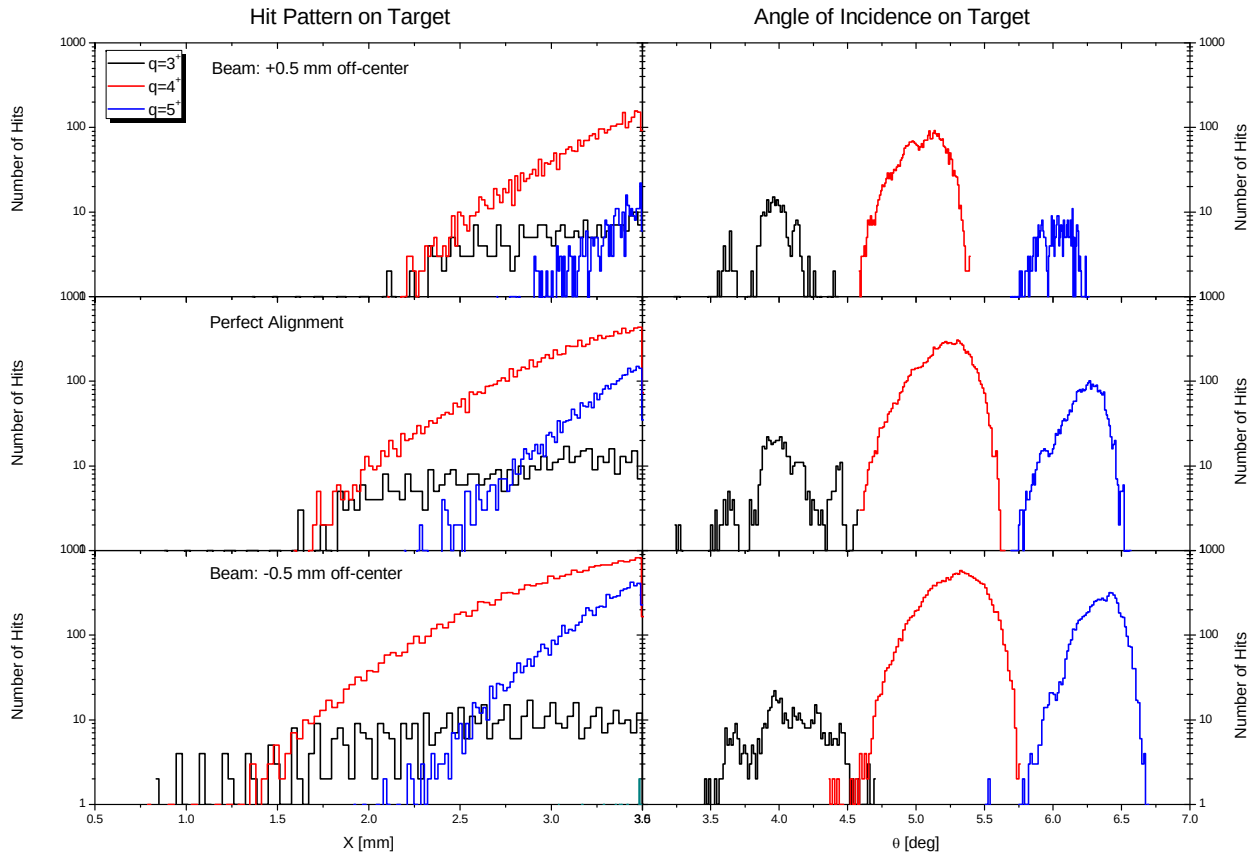

Figure 5.25. Effects of a 0.8 T magnetic field on the trajectory of the beam. Histograms represent the hit pattern and the angle of incidence on the target for three slightly different alignment cases. As can be seen, tuning of the beam is critical for the performance of the target.

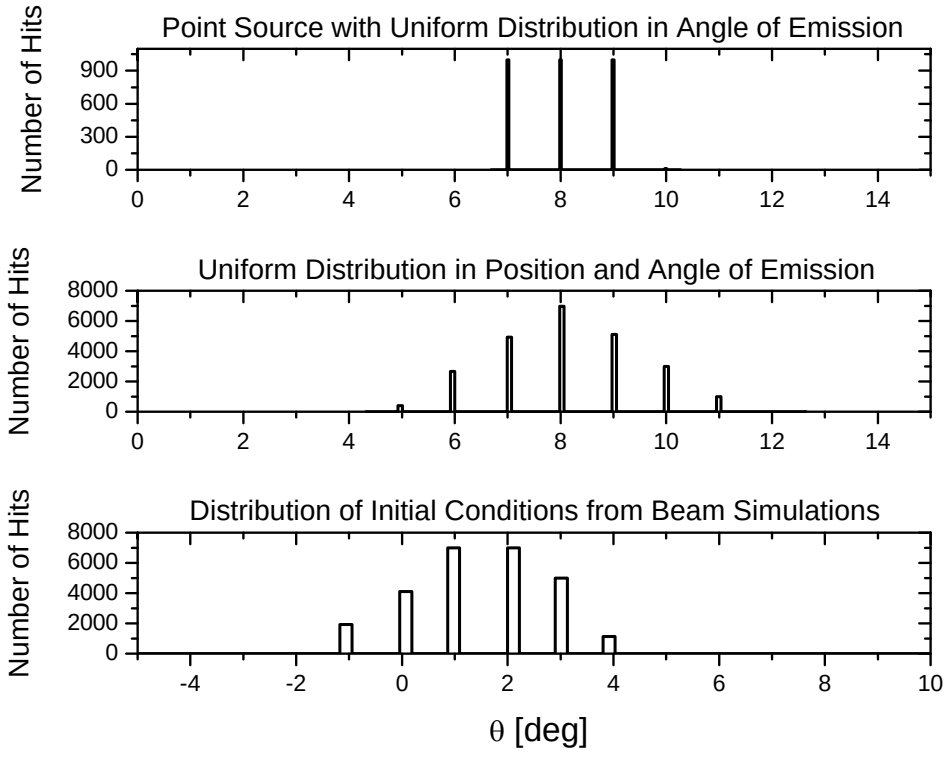

Figure 5.26. Effective angle of emission of mono-energetic protons for three different sets of initial conditions in a 0.8 T magnetic field (see text for more details).

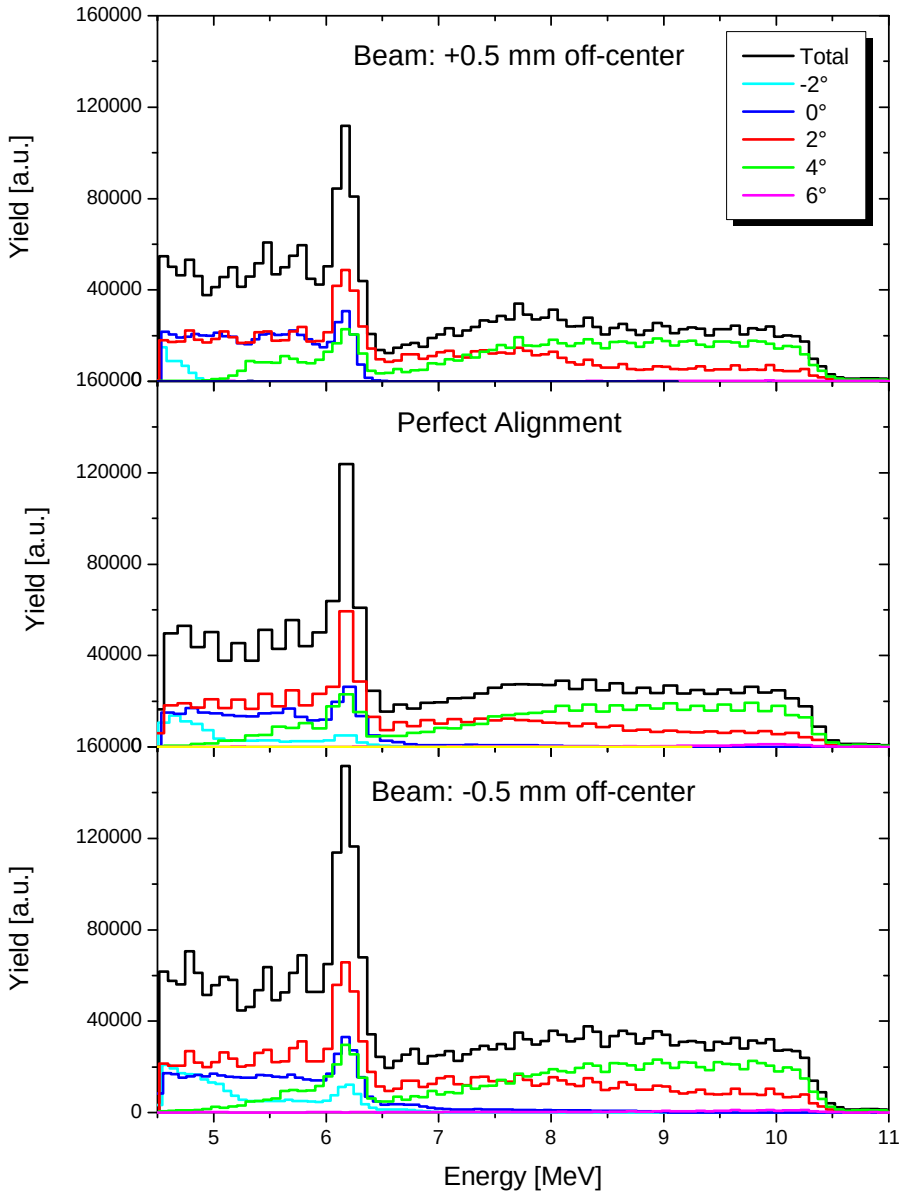

Figure 5.27. Simulated proton spectra recorded by a Silicon detector in a 0.8 T magnetic field. The black lines represent the total energy distributions, while the color lines indicate the contribution from a particular effective angle of emission of the protons.

In summary, we have demonstrated the feasibility of using the polarized target system for reactions with heavy ions at low energies in an elastic scattering experiment. Some implications of these findings will be discussed in the next chapter along with possible ways to deal with the issues associated with the operation of the target.

CHAPTER 6

Conclusions and Outlook

6.1 Summary and Conclusions

This dissertation has been written with the purpose to stimulate the exploration of polarization observables in reactions with RIBs. To accomplish this, we have identified specific areas were the use of a polarized target and RIBs in inverse kinematics is of importance, namely, elastic scattering, the study of weakly bound systems, transfer reactions, and the study of reaction mechanisms. Moreover, we developed the first prototype proton polarized target for low and intermediate energy heavy ions and demonstrated its operation under conditions similar to those encountered at an ISOL facility.

The first part of this work presented the mathematical formulation of polarization observables. The general formalism for scattering of particles with arbitrary spin was outlined, but the emphasis was done on elastic scattering of spin ½ particles by spin 0 nuclei. This corresponds to the simplest, non-trivial case of scattering of particles with spin and since the ground states of most even-even nuclei have spin 0, it will be also the most common case encountered in future experiments involving polarized proton targets.

Chapter three described general properties of RIBs, some of their experimental challenges, and some techniques to overcome them. In that context, the thick target technique was introduced as a tool that permits efficient measurements of excitation functions of cross sections in elastic scattering experiments performed with low beam intensities. The thicknesses of the polarized targets developed in this work allow those types of measurements to be extended to excitation functions of analyzing powers. In order to motivate further the use of polarized probes, some examples involving stable nuclei, where the power of polarization is evident, were shown. These include elastic scattering, the investigation of isolated resonances in light nuclei of interest in nuclear structure and astrophysics, one nucleon transfer reactions, and the study of reaction mechanisms.

Table 6.1. Parameters of operation of the polarized proton target.

Target thickness	0.1-20 mg/cm^2
Temperature of Operation	208 mK
Polarizing Magnetic Field	2.5 T
TEMPO concentration	2*10^{19} spins/cm^3
Microwave frequency	$f^{(u)}$=69990 MHz, $f^{(d)}$=70265 MHz
Maximum Polarization	31%
Proton relaxation time	90 h
Polarization build up time	3 h

The central part of this thesis consisted in the design, construction and proof of principle of a spin polarized proton target suitable for reactions with heavy ions at low and intermediate energies. The targets consist of polystyrene foils doped with the free radical TEMPO. Using the spin coating technique, minimum thicknesses of ~100 μg/cm^2 can be achieved. The operation of the targets is based on the well known DNP method, which requires low temperatures and strong magnetic fields [Abr 82]. DNP targets developed for experiments with minimum ionizing particles or for high energy experiments [Cra97] are impractical for reactions with RIBs due to their high ionization power. In order to overcome this issue, materials along the path of beam and recoils must be kept to a minimum. The problem was solved by placing the polystyrene foils in an isolated chamber closed by two thin silicon nitride windows. Although the chamber is thermally anchored to the mixing chamber of a dilution refrigerator, effective cooling of the foil proceeds upon condensation of a layer of superfluid helium on its exposed surface. The polarization of the target is monitored on-line by a CW NMR system, which consists of a coil in contact with the target foil, a $3\lambda/2$ resonant cable, a Liverpool box located in the exterior of the cryostat, and a computer controlled data acquisition module. This design allows continuous sampling of the polarization and provides flexibility to tune the system at several magnetic field strengths without the need to change the NMR coil.

The parameters of operation of the polarized target are summarized in table 6.1. The target is suitable to be used with heavy ion beams in a wide range of energies, starting at a few MeV per nucleon. However, due to the intense magnetic field of the target, different modes of operation should be considered for different beam energies. In some experiments at high and intermediate energies (E>~50 MeV/*A*), the

effect of the magnetic field on the trajectories of the charged particles might be neglected, which would allow the target to be operated at full field, while continuously polarizing it via DNP. In such a case, the microwave power delivered to the target should be optimized in order to balance the heat input from the beam. On the other hand, for reactions at low energies such as the ones typically performed at ISOL facilities, the effect of the field becomes critical and operation in dynamic mode is no longer possible. Instead, the target should be operated in frozen spin mode. In this mode, the DNP process is interrupted, the magnetic field is lowered to a holding value, and measurements are done while the spin of the protons follow their relaxation mechanism down to a reasonable polarization value. Once that value is reached, the field can be ramped up again and a new DNP cycle proceeds. Hence, the relaxation time becomes important because it determines the duration of a measurement cycle. This parameter depends exponentially on the inverse of temperature of the target but has only an approximate exponential behavior with the strength of the magnetic field. The data in figures 4.17, 4.18, and in [Bra 00] can be used as guidelines to estimate its value in polystyrene targets. Unfortunately, there is no general prescription as to which mode of operation should be used in a given experiment: The mode of operation should be ultimately chosen based on simulations of the trajectories of the particles.

The proof of principle of the target was performed with a stable beam of ^{12}C at ~3.2 MeV/*A*, avoiding the complexity of producing a RIB. The beam intensities delivered to the target ranged between 10^4 and 10^7 pps, ensuring that physical conditions associated with the beam were comparable to those encountered in an ISOL facility. The thickness of the target was 6.25 mg/cm^2, enough to stop the beam and to test the capabilities of the thick target technique in the measurement of polarization effects. We demonstrated that spin observables can be measured with the polarized target. Several observations could be made:

- Collisions with carbon nuclei from the target contribute in a significant manner to the measured spectra. In the case studied here, fusion-evaporation of the ^{12}C-^{12}C system generated protons and alpha particles in the same energy range as elastically scattered recoil protons. Using particle identification in experiments with unpolarized targets and statistical model calculations [Bee 09], we estimated the proton contributions to be below 10% of the total proton yield in the energy range of relevance for elastic scattering. Contributions from alpha particles are dominant at higher energies, but they are energetically separated from the proton distribution. Although this justified the use of a single silicon detector in our tests with the polarized target, future experiments will require particle identification capabilities in order to distinguish protons from other nuclear species. In addition, an independent determination of the proton yields from reactions with carbon nuclei should be used,

either in the form of statistical model calculations or, preferably, as a direct measurement with a pure carbon targets of similar thickness than the polarized target.

- It was demonstrated that the film of superfluid helium used to cool the target has a small effect on the recoiling protons: As a reference, 6 MeV protons lose ~100 keV in a 0.3 μm thick film. Since effects on heavier nuclei are evidently much more critical, the helium film actually behaves as an absorber of nuclei with high atomic number.

- After a delivered dose in excess of 10^{11} ions on the target, no effect on the polarization properties of the target material was observed. In other words, the number of free radicals in the plastic matrix of the target was not significantly modified by beam irradiation. This has consequences for long experimental runs with RIBs. If a beam intensity of 10^5 pps is assumed, one week of continuous irradiation would yield ~$6*10^{10}$ ions impinging on the target. In such a case, no problems are expected as far as polarization capabilities of the target are concerned.

- The effect of radiation damage on the target was only qualitatively studied. Irradiation of thick targets with well focused beams at ~10^6 pps results in local burning of the targets at room temperature after ~1½ h. This effect seems to be mitigated at low temperatures, perhaps due to a fast removal of heat in the cryogenic medium. At a temperature below 1 K and using beams distributed over the target area, only mild brown spots were infringed upon the target after a delivered dose of ~10^{12} ions, continuous irradiation periods no longer than 30 minutes at a time, and maximum beam intensities close to 10^7 pps.

- The effect of the magnetic field on the trajectories of charged particles is a major challenge for the operation of the target, especially at low energies. In order to account for this effect, we measured a detailed angular distribution of recoil protons from the same polystyrene foil at zero magnetic field. From this distribution we extracted the initial conditions required by a set of GEANT4 routines that propagate charged particles in the magnetic field generated by the superconductor magnet around the target. Those simulations reproduced qualitatively the spectra measured with the polarized target.

- Before reaching the target, the beam passes through a thin gold foil placed on one of the thermal radiation shields of the cryostat. This generates a charge equilibrium distribution of the ions in the beam. Since every charge state is associated with a different magnetic rigidity, the magnetic field produces a spatial broadening of the beam as well as different angles of incidence on the target. The

GEANT4 simulations showed that the spatial broadening leads to a decrease in the number of beam particles colliding with the target, while the distribution of angles of incidence should be known in order to infer the angle of emission of the recoils. In addition, the simulations demonstrated the high sensitivity of these effects to beam tuning conditions by considering small misalignments of the target setup.

- Due to the magnetic field, identical particles having the same energy but emitted at different angles from the target are able to reach the same detector. Since excitation functions depend on both the energy and the angle of emission of the particle, it is necessary to determine the latter based on its energy, angle of detection, and the preexisting knowledge of the magnetic field. The simulations indicate that, for the thick target used, the measured spectra exhibit contributions from different angles of emission. At a given energy, and within the acceptance of our detectors, we observe protons emitted in a certain range of angles. As a reference, if all the 6.2 MeV protons detected are grouped in angular bins of 2°, 48% are emitted at 2°, 21% at 0°, 19% at 4°, and 4% at -2°. In practical terms, this means that the angular information contained in spectra from the polarized target can be deconvoluted with the aid of our GEANT4 routines and associated input files (angular distribution of particles at zero magnetic field). Should more refined angular information be obtained, the use of a thinner target must be considered.

- We successfully operated surface barrier silicon detectors at 4 K and along the zero field circle of the superconductor magnet. However, after several thermal cycles of the cryogenic system, the likelihood of failure due to thermal stress increases. In future experiments it will be advisable to use detectors with mounts especially designed for low temperature applications.

6.2 Future Developments

Future work should focus primarily on improving the reliability of the silicon nitride windows of the target chamber. The probability for the frame of the windows to develop cracks upon cooling is close to 60%. Since repairs of any of the cryogenic components requires long periods of time (~1 week), this constitutes the major cause of concern for the operation of the target. At present, there is no certainty about the reasons for which cracks start to develop. Most likely, a non-uniform pressing of the windows creates an initial stress on the frame. As the temperature drops, the difference in expansion coefficients increases the stress until the material breaks. Dedicated experiments to tests this hypothesis and to investigate possible solutions include the use of new geometries for the windows, the use of materials

such as ceramics or glasses for the chamber, and elements of stress analysis that would require the use of cryostats with optical access to the sample holder.

A second point to consider in future investigations is how to increase the maximum polarization and the relaxation time of the target. In principle, this can be achieved by lowering the temperature inside the target chamber. Unfortunately, it is not clear whether the lowest operating temperature reached so far (208 mK) corresponds to the minimum temperature limit imposed by the Kapitza resistance [Pol 69], [Pob 96]. Dedicated measurements to establish the behavior of the temperature of the target as a function of the heat delivered to it are required to clarify this situation. In such studies, the temperature should be sampled directly in the plastic foil, not simply in its neighborhood as has been the case until now. If the measurements show a behavior markedly different of T^{-3}, then the target is not operating in the regime where Kapitza resistance effects are dominant [Pob 96]. In that case, one alternative to further lower the temperature is to increase the area of the inner sector of the chamber that is directly anchored to the mixing chamber of the dilution refrigerator. In practical terms this implies the use of a heat exchanger, perhaps in the form of a sintered flange. Such an exchanger would permit further cooling of the superfluid film that covers the target.

An additional source of improvement is to reduce the heat load on the dilution refrigerator. At present, the main sources of heat are the capillaries carrying helium into the target chamber and the NMR coaxial lines. The capillaries are long enough and offer a high flux impedance to ensure optimal thermal anchoring, while the reduced length of NMR coaxial lines ($3\lambda/2$ resonating cable) is insufficient to guarantee thermalization at every anchoring stage in the cryostat. The natural alternative is then to replace the resonating cable NMR scheme by a low temperature resonating circuit placed close to the target chamber. In such a case, it should be possible to use longer cables to transport the signals to and from the NMR coil, which will lead to better thermal anchoring. Similar schemes have been used in polarized targets built at PSI for experiments with neutrons [Bra 09], [Pie 09].

Minimizing the effect of the magnetic field on the trajectories of charged particles is another issue that requires further attention. In particular, the spatial broadening of the beam, introduced by the charge separation after passage through the radiation shield (gold foil), should be reduced. The ideal solution would be to simply eliminate the foil stripper, but the radiant heat deposited on the target would hamper the operation of the dilution refrigerator. Instead, a new shielding scheme could be devised to mount the gold foil closer to the target. A natural place to do it is the still shield, which lies only 6 cm apart from the

target and operates at a temperature close to 0.8 K. Evidently, if this works, new parameters for the proper operation of the still will have to be found in order to ensure the smooth operation of the cryostat. In addition, the overall consumption of ^{4}He will increase in this mode.

In future applications of the polarized target, the use of detection systems with high efficiency, large solid angle coverage, high granularity, and particle identification capabilities will be pivotal. For reactions at low energies or cases where very good energy resolution is required, detectors should be accommodated inside the thermal radiation shields of the cryostat, which sets their temperature of operation below 4 K. In such cases, the use of arrays of bolometers might be an alternative to the use of individual silicon detectors. On the other hand, for reactions at intermediate energies it might be appropriate to place the detectors outside the volume enclosed by the shields. If the energy of the recoils is such that straggling in the thin metallic foils of the shields is negligible, then it is conceivable to use state of the art detection systems specially designed for detection of light recoils in inverse kinematics, such as MUST2 [Pol 05] or HiRA [Wal 07]. With arrays like these, it is possible to measure position, energy, mass and charge of incident light ions ($Z<4$) with high resolution. They consist of several large area telescopes (10 cm x 10 cm in MUST2, 6.25 cm x 6.25 cm in HiRA), each composed of one thin silicon strip detector (300 μm DSSD in MUST2, 65 μm SSSD in HiRA), a thick silicon silicon detector (5 mm single pad in MUST2, 1.5 mm DSSD in HiRA), and CsI crystals read out by photodiodes (4 cm in MUST2, 4x4 cm in HiRA). The open geometry of the magnets of the polarized target will allow placing several of those telescopes along the reaction plane. Tests will be required to determine the optimal thickness of the thermal radiation shields that minimizes the energy loss and straggling. For the time being, SRIM calculations indicate that 10 MeV protons passing through three consecutive layers of aluminum, with a thickness of 10 μm each, will only lose 280 keV, which is an encouraging figure to think on future experiments using that kind of detection system.

One initial application of the polarized target might be to study the role of the core and valence neutrons in the elastic scattering observables of neutron-rich helium isotopes at intermediate energies. The exotic borromean nuclei ^{6}He and ^{8}He have been the subject of several recent studies both experimentally and theoretically. Theoretical models used to describe these nuclei include three-body models [Zhu 93], [Hiy 95], cluster-orbital shell models [Suz 91], [Fun 94], microscopic cluster models for various effective nucleon-nucleon interactions [Cso 93], [Wur 97], and no-core microscopic shell models (NCSM) [Nav 05]. Recently, the resonating group method (RGM) technique is being extended by P. Navratil using NSCM *ab initio* wavefunctions for the clusters involved with effective interactions derived from realistic

two- and three-nucleon forces [Nav 09]. Analyzing power computations are now possible with the development of the RGM/NCSM formalism and the implementation of new codes. On the experimental side, information on the scattering of ^{6}He+p exists at various energies. Proton elastic scattering angular distributions have been measured at bombarding energies for ^{6}He of 25.2A MeV [Gio 04]; 38.3A MeV [Lap 01]; 41.6A MeV [Lag 01]; 71A MeV [Kor 97] and 700A MeV [Neu 02]. Couplings to the continuum are expected to play a significant role in the scattering process with these nuclei. Phenomenological optical potentials such as CH89 [Var 91] and microscopic such as the JLM [Jeu 77] potential have been used to describe light nuclei albeit requiring renormalization factors attributed to the couplings necessary for the weakly bound nuclei [Cor 97]. Recently, the first experiment using a polarized target was performed at RIKEN. The analyzing power of ^{6}He at an energy of 71A MeV on a polarized proton target was reported in conference proceedings [Hat 05]. Striking differences were observed for the measured analyzing powers between the scattering of ^{6}He+p and ^{6}Li+p [Hen 94]. By contrast, the differential elastic-scattering angular distributions are almost identical. Clearly this peculiar behavior of A_y for ^{6}He+p, if confirmed, represents a theoretical challenge. Polarization data provide, after all, the ultimate knowledge of the scattering process.

REFERENCES

[Abr 55] A. Abragam, *Phys. Rev.* **98** (1955) 1729.

[Abr 58] A. Abragam and W. G, Proctor, *C .R. Acad. Sci.*, *Paris,* **255** (1958) 2253.

[Abr 62] A. Abragam et al., *Phys. Lett.* **2** (1962) 310.

[Abr 78] A. Abragam and M. Goldman, *Rep. Prog. Phys*. 41 (1978) 395.

[Abr 82] A. Abragam and M. Goldman, *Nuclear Magnetism: Order and Disorder*, Clarendon Press (1982) Oxford.

[Ade 98] E. Adelberger et al., *Rev. Mod. Phys.* **70** (1998) 1265.

[Aga 74] K. L. Agarwal and J. O. Betterton, *Cryogenics* **14** (1974) 520.

[Alk 04] J. Al-Khalili and E. Roeckl (Eds.), *The Euroschool Lectures on Physics with Exotic Beams, Vol. I*, Springer (2004) Heidelberg.

[Ang 03] C. Angulo et al., *Nucl. Phys.* ***A*716** (2003) 211.

[Asa 01] K. Asahi, *Prog. Part. Nucl. Phys.* **46** (2001) 321.

[Azj 91] F. Ajzenberg-Selove, *Nucl. Phys.* ***A*523** (1991) 1.

[Bal 61] A. M. Baldin et al., Kinematics of Nuclear Reactions, Pergamon Press (1961) New York.

[Bar 71] H. H. Barschall and W. Haeberli (Eds.), *Proceedings of the Third International Symposium on Polarization Phenomena in Nuclear Reactions,* Wisconsin University Press (1971) Madison.

[Bee 09] J.R. Beene, *EvapOR*, Computer Code, *Unpublished.*

[Ben 92] M. Benjelloun et al., *Nucl. Instr. and Meth. in Phys. Res.* ***A*321** (1992) 521.

[Bet 02] P. F. Bedaque and U. van Kolck, *Annu Rev. Nucl. Part. Sci*. **53** (2002) 339.

[Bor 66] M. Borghini, *Phys. Rev. Lett.* **16** (1966) 318.

[Bou 60] M. A. Bouchiat et al., *Phys. Rev. Lett.***5** (1960) 373.

[Bra 90] B. van den Brandt et al., *Nucl. Instr. and Meth. in Phys. Res.* ***A*289** (1990) 526.

[Bra 92] J. F. J. van den Brand, *Nucl. Phys*. ***A*546** (1992) 299c.

[Bra 95] B. van den Brandt et al., *Nucl. Instr. and Meth. in Phys. Res.* ***A*356** (1995) 36.

[Bra 96] B. van den Brandt et al., *Nucl. Instr. and Meth. in Phys. Res.* ***A*381** (1996) 219.

[Bra 00] B. van den Brandt et al., *Nucl. Instr. and Meth. in Phys. Res.* ***A*****446** (2000) 592.

[Bra 04] B. van den Brandt et al., *Nucl. Instr. and Meth. in Phys. Res.* ***A*****526** (2004) 53.

[Bra 09] B. van den Brandt et al., *J. Phys: Conf. Series* **150** (2009) 012024.

[Bro 51] A. B. Brown et al., *Phys. Rev*. **82** (1951) 159.

[Bun 04] E.I. Bunyatova, *Nucl. Instr. and Meth.* **A526** (2004) 22.

[Car 98] J. Carlson and R. Schiavilla, *Rev. Mod. Phys.* **70** (1998) 743.

[Cat 02] W. N. Catford, *Nucl. Phys.* ***A*****701** (2002) 1c.

[Cat 05] W. N. Catford, *J. Phys. G: Nucl. Part. Phys*. **31** (2005) S1655.

[Cha 54] O. Chamberlain et al., *Phys. Rev*. **96** (1954) 807

[Cha 06] K. Y. Chae et al., *Phys. Rev.* ***C*****74** (2006) 012801.

[Chu 94] T. E. Chupp et al., *Annu. Rev. Nucl. Part. Sci.* **44** (1994) 373.

[Coh 77] C. Cohen-Tannoudji et al., *Quantum Mechanics Vol. 1.,* John Wiley &Sons (1977) New York.

[Cor 97] M.D. Cortina-Gil *et al*., *Phys. Lett*. ***B*****401** (1997) 9.

[Cou 92] K. P. Coulter et al., *Phys Rev. Lett.* **68** (1992) 174.

[Cou 93] G. R. Court et al., *Nucl. Instr. and Meth. in Phys. Res.* ***A*****324** (1993) 433.

[Cou 94] K. P. Coulter et al., NIM (1994).

[Cou 04] G. R. Court, *Nucl. Instr. and Meth. in Phys. Res.* ***A*****526** (2004) 65.

[Cra 97] D. G. Crabb and W. Meyer, *Annu. Rev. Nucl. Part. Sci.* **47** (1997) 67.

[Cra 09] D. G. Crabb et al. (Eds), *Spin Physics: 18th International Spin Physics Symposium,* AIP Conference Proceedings (2009) **1149**.

[Cso 93] A. Csótó, *Phys. Rev*. ***C*****48** (1993) 165.

[Dab 55] J. W. T. Dabbs et al., *Phys. Rev*. **98** (1955) 1512

[Dan 65] J. M. Daniels, *Oriented Nuclei. Polarized Targets and Beams*, Academic Press (1965) New York.

[Dav 01] B. Davin et al., *Nucl. Instr. and Meth. in Phys. Res.* ***A*****473** (2001) 302.

[Duf 07] M. Dufor and P. Descouvemont, *Nucl. Phys.* ***A*****785** (2007) 381.

[Eng 74a] J. B. A. England, *Techniques in Nuclear Structure Physics. Part 1*, Macmillan (1974) London.

[Eng 74b] J. B. A. England, *Techniques in Nuclear Structure Physics. Part 2*, Macmillan (1974) London.

[Ere 86] N. V. Eremin et al., *Sov. J. Nucl. Phys.* **44** (1986) 11.

[Fer 54] E. Fermi, *Il Nuov. Cim*. **10** (1954) 407.

[Fun 94] S. Funada et al., *Nucl. Phys*. ***A*575** (1994) 93.

[Gal 91a] W. Galster et al., *Phys. Rev.* ***C*44** (1991) 2776.

[Gal 91] A. Galindo-Uribarri et al., *Nucl. Instr. and Meth. in Phys. Res*. ***A*301** (1991) 457.

[Gal 00a] A. Galindo-Uribarri, *Resonant Reactions with Radioactive Ion Beams*, RIA Workshop (2000) Raleigh-Durham.

[Gal 00] A. Galindo-Uribarri et al., *Nucl. Instr. and Meth. in Phys. Res*. ***B*172** (2000) 647.

[Gal 01] A. Galindo-Uribarri et al., *Nucl. Phys.* ***A682*** (2001) 363c.

[Gal 07] A. Galindo-Uribarri and J. P. Urrego-Blanco, *Rev. Mex. Fís.* ***S*53** (2007) 35.

[Gee 06] D. F. Geesaman et al., *Annu. Rev. Nucl. Part. Sci.* **56** (2006) 53.

[Gel 01] W. Gelletly, *Contemporary Physics*, **42** (2001) 285.

[Gio 04] L. Giot *et al*., *Nucl. Phys*. ***A*738**(2004)426.

[Goe 63] M. Goeppert-Mayer, *Autobiography*, The Nobel Foundation (1963), http://nobelprize.org/nobel_prizes/physics/laureates/1963/mayer-autobio.html

[Gol 75] M. Goldman, *J. Mag. Res.* 17 (1975) 393.

[Gom 01] J. Gómez del Campo et al., *Phys. Rev. Lett.* **86** (2001) 43.

[Gro 78] B. C. Grover, *Phys. Rev. Lett.* **40** (1978) 391.

[Gup 00] D. Gupta et al., *Nucl. Phys.* ***A*674** (2000) 77.

[Gur 08] A. Gurbich et al., *Nucl. Instr. and Meth. in Phys. Res.* ***B*266** (2008) 1198.

[Hag 92] E. Hagebø *et al.*, *Nucl. Instr. and Meth. in Phys. Res.* ***B*70** (1992) 165.

[Hal 04] D. Halderson, Phys. Rev. **C69** (2004) 014609.

[Hat 05] M. Hatano et al., *Eur. Phys. J.* ***A*25**, **s01** (2005) 255.

[Hau 04] P. Hautle, *Nucl. Instr. and Meth. in Phys. Res.* ***A*****526** (2004) 76.

[Hau 04] P. Hautle, *Private Communication*, (2005).

[Hau 08] P. Hautle, *Labview based NMR DAQ.*, Computer Code. *Unpublished.*

[Hen 90] A. Henstra et al., *Chem. Phys. Lett.* **165** (1990) 6.

[Hen 94] R. Henneck et al., *Nucl. Phys.* ***A*****571** (1994) 541.

[Heu 52] M. Heusinkveld and G. Freier, *Phys. Rev*. **85** (1952) 80.

[Hiy 95] E. Hiyama and M. Kamimura, *Nucl. Phys*. ***A*****588** (1995) 35C.

[Hub 61] P. Huber and K. P. Meyer (Eds.), *Proceedings of the International Symposium on Polarization Phenomena of Nucleons*, Helv. Phys. Act. S IV (1961) Basel.

[Hue 98] A. Huerta Hernández et al., *Nucl. Instr. and Meth. in Phys. Res.* ***B*****143** (1998) 569.

[Huy 02] M. Huyse, *Nucl. Phys.* ***A*****701** (2002) 265c.

[Jac 75] J. D. Jackson, *Electrodynamics*, John Wiley &Sons (1975) New York.

[Jef 64] C.D. Jeffries, *Annu Rev. Nucl. Sci.* **14** (1964) 101.

[Jeu 77] J.P. Jeukenne et al., *Phys. Rev*. ***C*****16** (1977) 80.

[Jew 07] C. Jewett et al., *Nucl. Instr. and Meth. in Phys. Res.* ***B*****261** (2007) 945.

[Jon 93] C. E. Jones et al., *AIP Conf. Proc*. **293** (1994) 3.

[Kaf 56] P. Kafalas and J. W. Irvine Jr., *Phys. Rev.* **104** (1956) 703.

[Kan 95] R. Kanungo et al., *Nucl. Phys.* ***A*****581** (1995) 294.

[Kat 05] T. Katabuchi et al., *Rev. Sci. Instrum.* **76** (2005) 033503.

[Kie 95] A. Kievsky et al., *Phys. Rev.* **C52** (1995) R15.

[Kno 79] G. F. Knoll, *Radiation Detection and Measurement*, John Wiley & Sons (1979) New York.

[Koi 87] Y. Koike and J. Haidenbauer, *Nucl Phys* ***A*****463** (1987) 365.

[Kon 68] J. A. Konter. *Indium Seals for Low Temperature Applications* (1968) *Unpublished*.

[Kon 07] J. A. Konter. *Private Communication*, (2007).

[Kor 97] A.A. Korsheninnikov *et al*., *Nucl. Phys*. ***A*****617** (1997) 45.

[Koz 05] R. L. Kozub et al., *Phys. Rev.* ***C*****71** (2005) 032801R.

[Kun 00] P. Kunz, *DWUCK4*, Distorted Wave Born Approximation Code.
http://spot.colorado.edu/~kunz/DWBA.html

[Lag 01] A. Lagoyannis *et al*., *Phys. Lett*. ***B*****518** (2001) 27.

[Lap 01] V. Lapoux *et al*., *Phys. Lett*. ***B*****517** (2001) 18.

[Lee 07] D. Lee, *Study of Nuclear Reactions with 11C and 15O Radioactive Ion Beams*, PhD. Thesis, University of California (2007) Berkeley.

[Liv 06] R. J. Livesay, *Inelastic and Elastic Scattering of Protons from Radioactive Beryllium-7*, PhD. Thesis, Colorado School of Mines (2006) Golden.

[Lou 74] O. V. Lounasmaa, *Experimental Principles and Methods Below 1K*, Academic Press (1974) London.

[Lyn 88] W. B. Lynch et al., Rev. Sci. Instr. 59 (1988) 1345.

[Lyo 77] K. G. Lyon et al., *J. Appl. Phys.* **48** (1977) 865.

[Men 93] A. J. Mendez II., *An Optically Pumped Polarized Lithium Ion Source and an Investigation of* $^{12}(^{6}Li,\alpha)^{14}N$, PhD Thesis, Florida State University (1993) Tallahassee.

[Mer 98] E. Merzbacher, *Quantum Mechanics*, John Wiley & Sons (1998) New York.

[Mic 67] A. Michalowicz, *Kinematics of Nuclear Reactions*, Iliffe Books Ltd (1967) London.

[Mac 60] M. H. MacGregor et al., *Annu. Rev. Nucl. Sci.* **10** (1960) 291.

[Mcc 63] J. A. McCray, *Phys. Rev.* **130** (1963) 2034.

[Mil 00] W. Milner, *CHARGE,* Computer Code, *Unpublished*.
ftp://ftp.phy.ornl.gov/pub/upak/

[Mil 01] W. Milner, *Stopx,* Computer Code, *Unpublished*.
ftp://ftp.phy.ornl.gov/pub/upak/

[Nan 87] S. K. Nanda et al., *Phys. Lett.* ***B*****188** (1987) 177.

[Nav 05] P. Navratil, *Private Communication*, (2005).

[Nav 06] P. Navratil et al., *Phys. Rev.* ***C*****73** (2006) 065801.

[Nav 09] P. Navratil, *Private Communication*, (2009).

[Neu 02] S.R. Neumaier, *et al*., *Nucl. Phys*. ***A*****712** (2002) 247.

[Nsa 07] NSA, *The Frontiers of Nuclear Science, A long Range Plan*, 2007, http://www.sc.doe.gov/henp/np/nsac/docs/LRP_5547_FINAL.pdf

[Nup 04] NuPECC, *Long Range Plan 2004: Perspectives for Nuclear Physics Research in Europe in the Coming Decade and Beyond*, 2004, http://www.nupecc.org/lrp02/long_range_plan_2004.pdf

[Ohl 72] G. G. Ohlsen, *Rep. Prog. Phys*. **35** (1972) 717.

[Ohl 72a] G. G. Ohlsen et al., *Phys. Rev. C***5** (1972) 1205.

[Pad 04] E. Padilla-Rodal, *Study of Germanium and Selenium Isotopes using COULEX and RIBS*, PhD. Thesis, Universidad Nacional Autonoma de Mexico (2004) Mexico, D.F.

[Phi 59] G. C. Phillips and P. D. Miller, *Phys. Rev.* **115** (1959) 1268.

[Pie 09] F. Piegsa, *Neutron Spin Precession in Samples of Polarised Nuclei and Neutron Spin Phase Imaging*, PhD Thesis, Technische Universität München (2009) München.

[Pol 66] *Proceedings of the Second International Symposium on Polarization Phenomena in Nuclear Reactions, Experentia,* Birkhäuser Verlag (1966) Basel.

[Pol 69] G. Pollack, *Rev. Mod. Phys*. **41** (1969) 48.

[Pol 03] Exploratory Workshop on Polarized Radioactive Beams and Polarized Targets, http://wwwires.in2p3.fr/ires/workshops/polar03/Bulletin.htm, (2003) Strasbourg.

[Pob 96] F. Pobell, *Matter and Methods at Low Temperatures*, Springer (1996) Berlin.

[Rat 93] F. Rathman et al., *Phys. Rev. Lett.* **71** (1993) 1379.

[Red 55] A. Redfield, *Phys. Rev.* **98** (1955) 1787.

[Reh 98] K. E. Rehm et al., *Phys. Rev. Lett*. **80** (1998) 676.

[Rog 01] G. V. Rogachev et al., *Phys. Rev.* ***C*64** (2001) 061601.

[Rou 66] P. Roubeau, *Cryogenics* (1966) 207.

[Roz 70] E. G. Rozantsev, *Free Nitroxyl Radicals*, Plenum Press (1970) New York.

[Sak 85] J. J. Sakurai, Modern Quantum Mechanics, Addison-Wesley (1985) Reading.

[San 74] F. D. Santos, *Nucl. Phys.* ***A*236** (1974) 90.

[Sat 64] G. R. Satchler, *Nucl. Phys.* ***A*55** (1964) 1.

[Sat 83] G. R. Satchler, *Direct Nuclear Reactions,* Clarendon Press (1983) New York.

[Saw 88] R. Sawafta et al., *Phys. Lett.* ***B*201** (1988) 219.

[Sed 08] K. Sedlak, *Private Communication*, (2008).

[Shi 08] T. Shiroka et al., *GEANT4 as a Simulation Framework in μSR*, Unpublished, (2008).

[Sig 08] http://www-nds.iaea.org/sigmacalc/

[Sil 76] B. L. Silver, *Irreducible Tensor Methods,* Academic Press (1976) New York.

[Sim 53] A. Simon, *Phys. Rev.* **92** (1953) 1050.

[Sim 67] M. Simonius, *Phys. Rev. Lett*. **19** (1967) 279.

[Sim 74] M. Simonius, *Lecture Notes on Physics, Vol. 30*. (ed. D. Fick), Springer (1974) Heidelberg.

[Sit 91] A. G. Sitenko, *Scattering Theory*, Springer-Verlag (1991) Berlin.

[Ski 95] M. Skill et al., *Nucl. Phys.* ***A*581** (1995) 93.

[Str 03] D.W. Stracener, *Nucl. Instr. and Meth. in Phys. Res.* ***B*204** (2003), 42.

[Str 04] D. W. Stracener et al., *Nucl. Instr. and Meth. in Phys. Res.* ***A*521** (2004) 126.

[Str 09] D.W. Stracener, *Private Communication* (2009).

[Suz 91] Y. Suzuki, *Nucl. Phys*. ***A*528** (1991) 395.

[Til 04] D. R. Tilley et al., *Nucl. Phys.* ***A*745** (2004) 155.

[Tom 97] S. Tomonaga, *The Story of Spin*, University of Chicago Press (1997) Chicago.

[Tor 82] W. Tornow et al., *Phys. Rev. Lett*. **49** (1982) 312.

[Tor 07] W. Tornow et al., *Nucl. Phys.* ***A*790** (2007) 64c.

[Tor 08] W. Tornow, *Few Body Syst.* **43** (2008) 213.

[Ues 07a] T. Uesaka et al. (Eds.), *Polarized Sources and Targets: Proceedings of the 11th International Workshop*, World Scientific (2007) Singapore.

[Ues 07] T. Uesaka et al., *Eur. Phys. J.Special Topics* **150** (2007) 71.

[Urr 05] J. P. Urrego-Blanco et al., *Nucl. Instr. and Meth. in Phys. Res.* ***B*241** (2005) 1001.

[Urr 07] J. P. Urrego-Blanco et al., *Nucl. Instr. and Meth. in Phys. Res.* ***B*261** (2007) 1112.

[Var 91] R.L. Varner et al., *Phys. Rep*. **201** (1991)57.

[Vig 75] S. E. Vigdor and W. Haeberli, *Nucl. Phys.* ***A*253** (1975) 55.

[Viv 01] M. Viviani et al., *Phys. Rev. Lett.* **86** (2001) 3739.

[Wak 05] T. Wakui et al., *Nucl. Instr. and Meth. in Phys. Res.* ***A*550** (2005) 521.

[Wea 96] L. W. Weathers and M. B. Tsang, *Nucl. Instr. and Meth.* ***A*381** (1996) 567.

[Wep 00] S. P. Weppner et al., *Phys Rev* ***C*61** (2000) 044601.

[Wil 67] J. Wilks, *The Properties of Liquid and Solid Helium*, Clarendon Press (1967) Oxford.

[Win 97] J. S. Winfield et al., *Nucl. Instr. and Meth.* ***A*396** (1997) 147.

[Wit 94] H. Witala et al., *Phys Rev* ***C*49** (1994) R14.

[Wol 49] L. Wolfenstein, *Phys. Rev.* **75** (1949) 1664.

[Wol 52] L. Wolfenstein and J. Ashkin, *Phys. Rev.* **85** (1952) 947.

[Wol 53] L. Wolfenstein, *Phys. Rev.* **92** (1953) 123.

[Wol 56] L. Wolfenstein, *Annu. Rev. Nucl. Sci*. **6** (1956) 43.

[Wur 97] J. Wurzer and H.M. Hofmann, *Phys. Rev*. ***C*55** (1997) 688.

[Yag 78] K. Yagi et al., *Phys. Rev. Lett.* **40** (1978) 161.

[Zhu 85] X. Zhu et al., *Nucl. Phys.* ***A*439** (1985) 619.

[Zie 06] J. F. Ziegler, *The Stopping and Range of Ions in Matter, SRIM*-2006.
http://www.srim.org/SRIM/SRIMLEGL.htm

[Zhu 93] M.V. Zhukov et al., *Phys. Rep*. 231 (1993) 151.

APPENDICES

APPENDIX A

Elastic Scattering in Inverse Kinematics

Inverse kinematics has a profound impact on the detection geometry of each experiment. In general, particles emitted in the reactions tend to be strongly forward focused, which makes the use of large area detection arrays with high granularity desirable. In order to visualize more clearly the general results, I will outline here the procedure to deduce the kinematic observables of a binary reaction using classical rather than relativistic mechanics (see the kinematical diagram shown in figure A.1. Detailed derivations can be found in [Mic 67] or [Bal 61].

Consider two particles in the entrance channel with masses M_1 and M_2. It will be assumed that the incident particle M_1 strikes the target M_2, which is initially at rest in the laboratory system. If the energy of the collision in the laboratory system is denoted by T_1 and the masses of the reaction products are M_3 and M_4, then the relations between kinematical quantities in the laboratory system and the center of mass (CM) system follow from the Galilean addition of velocities and the conservation laws of energy and momentum. In particular, the velocity of the CM system V is given by:

$$V = \frac{M_1}{M_1 + M_2} v_1, \tag{A.1}$$

where v_1 is the velocity of the projectile in the laboratory system. From this relation it follows that the velocity of the entrance channel particles in the center of mass is:

$$\bar{v}_1 = \frac{M_2}{M_1 + M_2} v_1 \tag{A.2}$$

and

$$\bar{v}_2 = V\,. \tag{A.3}$$

Combining these relationships with the conservation laws in the CM system, one can derive the general expressions that appear in table A.1. From those expressions and from the geometry shown in figure A.1 it is possible to extract relationships between the angles at which particles are emitted and their energies. Thus, for the case of elastic scattering (M_1=M_3 and M_2=M_4) one has:

$$\tan\theta_3 = \frac{\sin\bar{\theta}_3}{\cos\bar{\theta}_3 + M_1/M_2}, \quad \theta_4 = \bar{\theta}_4/2 \tag{A.4}$$

and

$$T_3 = \frac{M_2^2}{(M_1+M_2)^2} T_1 \left\{ 1 + \frac{M_1^2}{M_2^2} - 2\frac{M_1}{M_2}\left[\frac{M_1}{M_2}\sin^2\theta_3 \pm \cos\theta_3 \sqrt{1 - \frac{M_1}{M_2}\sin^2\theta_3} \right] \right\}$$

$$T_4 = \frac{4M_1M_2}{(M_1+M_2)^2} T_1 \cos^2\theta_4 . \tag{A.5}$$

In contrast with normal kinematics, notice that in inverse kinematics there are two real solutions for T_A. For the sake of completeness, the relativistic expressions for the constants of motion in elastic scattering are also given in table A.2 (see [Mic 77] for details). Analogous behavior occurs for other reactions of interest. In particular, the kinematical implications of transfer reactions on experiments with heavy ions are well described in the literature [Win 97], [Cat 02].

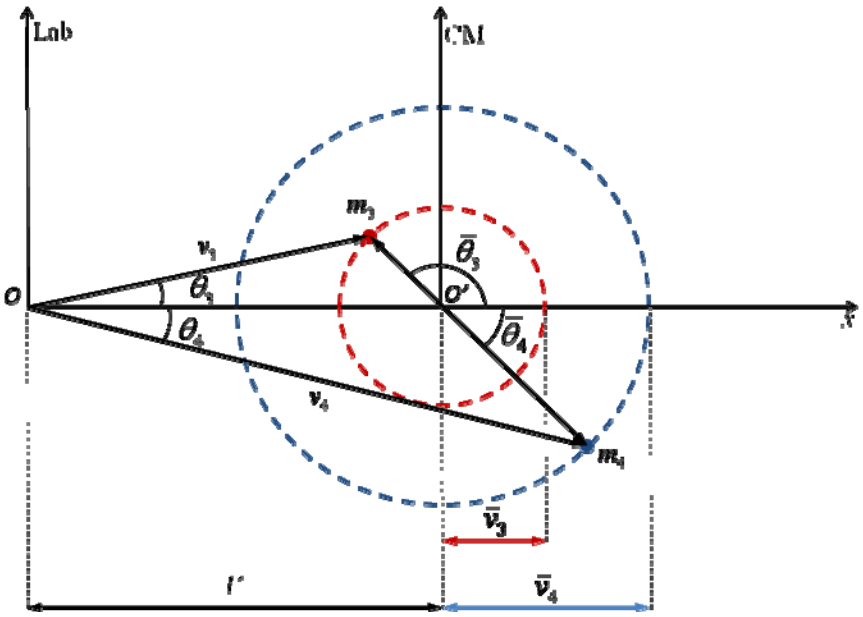

Figure A.1. Kinematical diagram of a binary reaction. Notice that in this diagram, the Galilean addition of velocities is used. The quantities q, v, T, etc are defined in the laboratory system, while the bar denotes the corresponding quantities in the CM system.

Table A.1. Kinematic variables in a binary collision. Quantities are deduced by assuming initial masses M_1 and M_2 and using classical kinematics.

$$M_1 + M_2 = M_3 + M_4 + Q$$

V	$\frac{M_1}{M_1 + M_2} v_1$
$\bar{v}_3$	$c\sqrt{\frac{2M_4\left(\bar{T}_t + Q\right)}{M_3\left(M_3 + M_4\right)}}$
$\bar{v}_4$	$c\sqrt{\frac{2M_3\left(\bar{T}_t + Q\right)}{M_4\left(M_3 + M_4\right)}}$
$\bar{P}_3 = \bar{P}_4$	$c\sqrt{\frac{2M_3M_4\left(\bar{T}_t + Q\right)}{\left(M_3 + M_4\right)}}$
$\bar{T}_t$	$\frac{M_2}{\left(M_1 + M_2\right)} T_1$
$\bar{T}_3$	$\frac{M_4\left(\bar{T}_t + Q\right)}{\left(M_3 + M_4\right)}$
$\bar{T}_4$	$\frac{M_3\left(\bar{T}_t + Q\right)}{\left(M_3 + M_4\right)}$

Table A.2. Kinematic variables in elastic scattering of two particles. Quantities are deduced by using classical and relativistic kinematics [Mic 67].

$$M_1 = M_3,\ M_2 = M_4$$

	Classical Kinematics	**Relativistic Kinematics**
V	$\frac{M_1}{M_1 + M_2} v_1$	$\frac{cP_1}{T_1 + M_1 + M_2}$
$\overline{v}_3$	$\frac{M_2}{M_1 + M_2} v_1$	$\frac{M_2}{M_1} \frac{V}{\sqrt{1 + \left(\frac{V}{c}\right)^2 \left(\frac{M_2^2}{M_1^2} - 1\right)}}$
$\overline{v}_4$	$\frac{M_1}{M_1 + M_2} v_1$	V
$\overline{P}_3 = \overline{P}_4$	$\frac{M_2}{M_1 + M_2} P_1$	$\frac{M_2 V}{\sqrt{1 - \left(\frac{V}{c}\right)^2}}$
$\overline{T}_3$	$\frac{M_2^2}{(M_1 + M_2)} T_1$	$\frac{M_2 V c^2}{\overline{v}_3 \sqrt{1 - \left(\frac{V}{c}\right)^2}} - M_1 c^2$
$\overline{T}_4$	$\frac{M_1 M_2}{(M_1 + M_2)} T_1$	$\frac{M_2 V c^2}{\overline{v}_3 \sqrt{1 - \left(\frac{V}{c}\right)^2}} - M_1 c^2$

APPENDIX B

Calibration of NMR Signals

It was shown in chapter 4 that the target polarization P can be expressed as:

$$P = C\int_0^\infty \chi'' d\omega\,, \tag{B.1}$$

where C is a constant that depends on the measurement instruments and the filling factor of the NMR coil, χ'' is the absorptive part of the magnetic susceptibility of the target, and ω is the angular frequency of the RF signal. In practice, the line shape of the NMR signal can be easily integrated, resulting in a numerical value for the integral in the equation (B.1). The calibration of the signals can be carried out once the spins in the target reach thermal equilibrium in a magnetic field B and at a temperature T. Under such conditions, the proton spins follow a Maxwell-Boltzmann distribution, which results in a net polarization given by:

$$P = \tanh\left(\frac{\mu B}{2kT}\right), \tag{B.2}$$

where μ is the magnetic moment of the proton and k is the Boltzmann constant. Based on this expression, the constant C can be simply determined as:

$$C = \tanh\left(\mu B \big/ 2kT\right) \Big/ \text{Signal Integral}\,. \tag{B.3}$$

Typically, calibration of the NMR setup is performed at temperatures around 1 K and B = 2.5 T, the reason being that under these conditions, the spins of the protons reach equilibrium within a few minutes[19]. Since the thermal equilibrium proton polarization in such cases is low (~0.25%), it is often difficult to see a resonance signal during a single frequency scan. Instead, it is necessary to scan several times and add the corresponding signals. Figure B.1 shows the summed Q-curves corresponding to one hundred frequency scans on a polystyrene target. One of the curves was measured at a field of 2.5 T

[19] Calibration at lower temperatures (e.g. 300 mK) are in general avoided because the time to reach equilibrium increases exponentially with the inverse of the temperature.

(resonance signal), while the contributions to the background curve were obtained at a slightly different field (corresponding to a Larmor frequency just below the

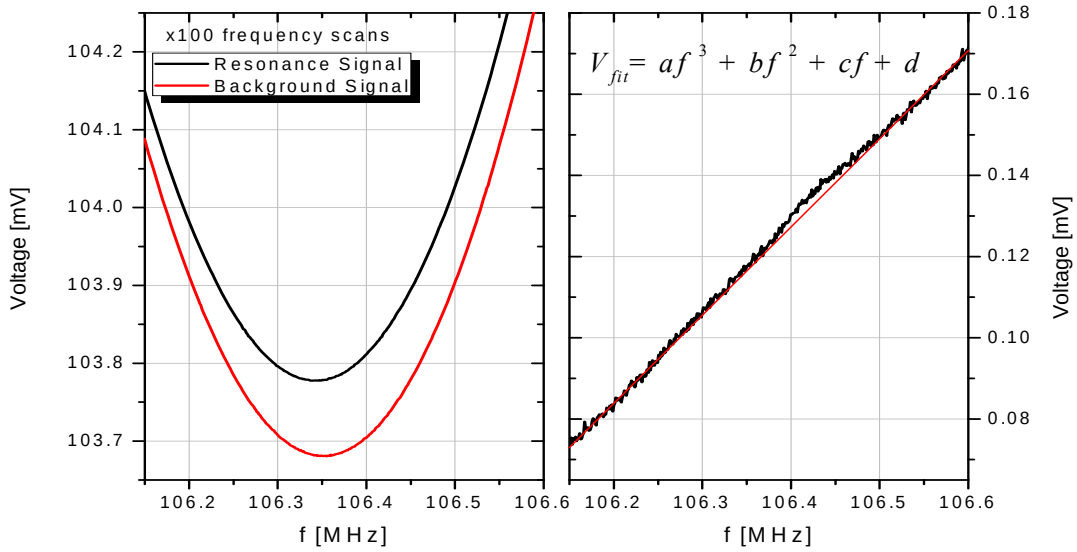

Figure B.1. Q-curves acquired during thermal equilibrium measurements of polarization. Each curve on the right hand side graph was obtained after 100 frequency scans. The graph on the left shows the resulting NMR signal after background subtraction, together with a cubic fit for the baseline of the signal.

Range of scanned frequencies). The difference between the two curves corresponds to the thermal equilibrium NMR signal augmented a hundred times. The baseline of such a signal follows a trend that is accounted for by a polynomial fit. The integral of the NMR signal appearing in equation (B.3) can then be calculated as the area enclosed between the curves in the left hand side graph of figure B.1.

APPENDIX C

Examples of Proton Trajectories in the Magnetic Field of the Target

The GEANT4 routines developed to simulate the trajectories of charged particles in the magnetic field of the target are controlled by a macro-file defining the geometry of the experimental setup. In turn, the macro-file uses two files provided by the user, one of which contains the field map of the magnet and the other the initial conditions for the particles propagating in the field.

Here we present a simplified macro-file containing all the essential components of the target, together with an input file with the initial conditions for a run of five protons, and the simulated trajectories.

MACRO FILE:

```
# Specify the geometry parameters in this file.
# All dimensions are in mm
# Lines starting with star "#" are comments.
#-----------------------------------------
# syntax:
# construct solid_type volume_name parameters_defining_solid
# material  position mothers_name
#(mothers_name starts
# with log_ )
#========================================================================
# ROTATION MATRIXES:
/musr/ignore rotation matrix1 0 90 0 0
/musr/ignore rotation matrix2 0 1 0 -15
/musr/ignore rotation matrix3 0 1 0 15
# WORLD
/musr/ignore construct box  World  1000 1000 2000 G4_Galactic 0 0
0 no_logical_volume norot dead -1
# COLLIMATORS
#/musr/ignore construct tubs col_1         2.0 20 1 0 360 G4_Al   0 0 -1430 log_World  norot dead
204
#/musr/ignore construct tubs col_2         1.5 20 1 0 360 G4_Al   0 0 -890 log_World norot dead
205
# GOLD FOIL
/musr/ignore construct box  gold_foil  2 3 0.001  G4_Au 0 0 -125  log_World norot dead 99
# TARGET
/musr/ignore construct box  polyst_target  3.5 3.5 0.029481  G4_POLYSTYRENE 0 0 0  log_World
norot dead 100
#/musr/ignore construct box detector_3       3.5 3.5 1      G4_Si 0 0 1 log_World norot
musr/ScintSD 11
```

```
# TARGET CHAMBER
/musr/ignore construct box  substrate_1  8.75 2.625 0.2625  G4_Si 0 6.125 -2.2625  log_World
norot dead 111
/musr/ignore construct box  substrate_2  8.75 2.625 0.2625  G4_Si 0 -6.125 -2.2625  log_World
norot dead 112
/musr/ignore construct box  substrate_3  2.625 8.75 0.2625  G4_Si 6.125 0 -2.2625  log_World
norot dead 113
/musr/ignore construct box  substrate_4  2.625 8.75 0.2625  G4_Si -6.125 0 -2.2625  log_World
norot dead 114
/musr/ignore construct box  frame_1  9.75 3.625 2  G4_Al 0 10.125 -4.2625  log_World norot dead
115
/musr/ignore construct box  frame_2  9.75 3.625 2  G4_Al 0 -10.125 -4.2625  log_World norot dead
116
/musr/ignore construct box  frame_3  3.625 9.75 2  G4_Al 10.125 0 -4.2625  log_World norot dead
117
/musr/ignore construct box  frame_4  3.625 9.75 2  G4_Al -10.125 0 -4.2625  log_World norot dead
118
/musr/ignore construct box  substrate_5  8.75 2.625 0.2625  G4_Si 0 6.125 2.2625  log_World norot
dead 119
/musr/ignore construct box  substrate_6  8.75 2.625 0.2625  G4_Si 0 -6.125 2.2625  log_World
norot dead 120
/musr/ignore construct box  substrate_7  2.625 8.75 0.2625  G4_Si 6.125 0 2.2625  log_World norot
dead 121
/musr/ignore construct box  substrate_8  2.625 8.75 0.2625  G4_Si -6.125 0 2.2625  log_World
norot dead 122
/musr/ignore construct box  frame_5  9.75 3.625 2  G4_Al 0 10.125 4.2625  log_World norot dead
123
/musr/ignore construct box  frame_6  9.75 3.625 2  G4_Al 0 -10.125 4.2625  log_World norot dead
124
/musr/ignore construct box  frame_7  3.625 9.75 2  G4_Al 10.125 0 4.2625  log_World norot dead
125
/musr/ignore construct box  frame_8  3.625 9.75 2  G4_Al -10.125 0 4.2625  log_World norot dead
126
/musr/ignore construct box  tframe_1  8.75 2.625 1  G4_TEFLON 0 6.125 1  log_World norot dead 127
/musr/ignore construct box  tframe_2  8.75 2.625 1  G4_TEFLON 0 -6.125 1  log_World norot dead
128
/musr/ignore construct box  tframe_3  2.625 8.75 1  G4_TEFLON 6.125 0 1  log_World norot dead 129
/musr/ignore construct box  tframe_4  2.625 8.75 1  G4_TEFLON -6.125 0 1  log_World norot dead
130
# WINDOWS
/musr/ignore construct box  entrance_window  3.5 3.5 0.00062  G4_POLYSTYRENE 0 0 -2  log_World
norot dead 101
/musr/ignore construct box  exit_window  3.5 3.5 0.00062    G4_POLYSTYRENE 0 0 2  log_World norot
dead 102
# DETECTORS
/musr/ignore construct tubs  detector_1      0 7.5 0.75 0 360 G4_Si   31.0583 0 115.9111
log_World matrix2 musr/ScintSD 1
/musr/ignore construct tubs  detector_2      0 7.5 0.75 0 360 G4_Si  -31.0583 0 115.9111
log_World matrix3 musr/ScintSD 2
# DETECTION APERTURE
/musr/ignore construct tubs  col_det1      3.5 15 1 0 360 G4_Al    30.023 0 112.0474 log_World
matrix2 dead 3
/musr/ignore construct tubs  col_det2      3.5 15 1 0 360 G4_Al   -30.023 0 112.0474 log_World
matrix3 dead 4
/musr/ignore construct tubs  col_det1a     5.0 15 1.5 0 360 G4_Al  30.670 0 114.4622 log_World
matrix2 dead 5
/musr/ignore construct tubs  col_det2a     5.0 15 1.5 0 360 G4_Al  -30.670 0 114.4622 log_World
matrix3 dead 6
# COILS
/musr/ignore construct tubs coil_2         70 125 35 0 360 G4_Cu   0 -60 0 log_World  matrix1
dead 202
/musr/ignore construct tubs pillar_1       70 125 25 35 15 G4_Cu   0  0 0 log_World  matrix1 dead
203
/musr/ignore construct tubs pillar_2       70 125 25 155 15 G4_Cu   0  0 0 log_World  matrix1
dead 203
/musr/ignore construct tubs pillar_3       70 125 25 275 15 G4_Cu   0  0 0 log_World  matrix1
dead 203
# HEAT SHILEDS
```

```
/musr/ignore construct tubs  shield_1    125 125.3 52 270.8 358.4 G4_Al  0 -47 0 log_World
matrix1   dead 51
/musr/ignore construct tubs  shield_2    127 127.3 52 270.8 358.4 G4_Al  0 -47 0 log_World
matrix1   dead 52
/musr/ignore construct tubs  shield_3    129 129.3 52 270.8 358.4 G4_Al  0 -47 0 log_World
matrix1   dead 52
# DUMMY VOLUME JUST FOR FIELD
/musr/ignore construct tubs dummy         0. 0.01 0.01 0 360 G4_Galactic   0 0 0.05 log_World
matrix1 dead 1001
#============================================================
# Set magnetic field  (set field intensity in T and sigma in mm)
# syntax for magneticfield:  fromfile filename fieldValue
#                            uniform  fieldValue
#                            gaussian fieldValue sigma
#
# A value of 100000 at the end of the next line corresponds to a #field of 2.5T
/musr/ignore globalfield centralSolenoidField 0. 0. 0.05 fromfile 2D RIB_B-map_half.table
log_dummy 32000.
#/musr/ignore magneticfield fromfile 2D OI_10T_grid_xz.table 10
/musr/ignore globalfield setparameter SetLargestAcceptableStep 0.4
/musr/ignore globalfield setparameter SetMinimumEpsilonStep 5e-5
/musr/ignore globalfield setparameter SetMaximumEpsilonStep 0.001
/musr/ignore globalfield setparameter SetDeltaOneStep 0.1
/musr/ignore globalfield setparameter SetDeltaIntersection 0.01
/musr/ignore globalfield printparameters
/musr/ignore globalfield printFieldValueAtPoint 0 0 0
/musr/ignore globalfield printFieldValueAtPoint 0 0 10
/musr/ignore globalfield printFieldValueAtPoint 0 0 20
/musr/ignore globalfield printFieldValueAtPoint 20 0 20
/musr/ignore globalfield printFieldValueAtPoint 20 20 20
#============================================================
# Set some other parameters
# Set the overall range cut
#/run/setCut 1 mm
# Set the range cut on a particular volumes (in mm)
##/musr/ignore SetUserLimits log_polyst_target 0.01
# Store all events into the ROOT tree or just the interesting ones ? (true is default)
/musr/ignore storeOnlyEventsWithHits false
# Set the minimum time separation between two subsequent signals in the same detector (in ns)
/musr/ignore signalSeparationTime 0.1
#============================================================
/musr/run/howOftenToPrintEvent 10000
/musr/run/randomOption 2
#
# for drawing the tracks
#/vis/disable
# (if too many tracks cause core dump => storeTrajectory 0)
/tracking/storeTrajectory 1
/vis/viewer/reset
/vis/scene/create
/vis/open VRML2FILE
###/vis/open DAWNFILE
/vis/drawVolume
/vis/viewer/set/viewpointThetaPhi 0 90 deg
/vis/viewer/flush
/vis/scene/add/trajectories
/vis/scene/endOfEventAction accumulate
#/hits/verbose 2
######################### P A R T I C L E   G U N
/gun/vertex 0 0 0.029481 mm
# TURTLE
/gun/turtlefilename Example.txt
#
########################  B E A M    O N  ######################################
#
/run/beamOn 5
```

INPUT FILE

Each row in this file is read as:

x [cm]	θ_x [mrad]	y [cm]	θ_y[mrad]	z [cm]	p[GeV]	0.0	0.0	Z	A

```
#Example.txt
0.200    20.450   0.000   0.000   0.000  0.926037025   0.0  0.0   1   1
0.200    83.450   0.000   0.000   0.000  0.0926037025  0.0  0.0   1   1
0.200   120.450   0.000   0.000   0.000  0.0926037025  0.0  0.0   1   1
0.200   120.450   0.000   0.000   0.000  0.76037025    0.0  0.0   1   1
0.200   120.450   0.000   0.000   0.000  0.026037025   0.0  0.0   1   1
```

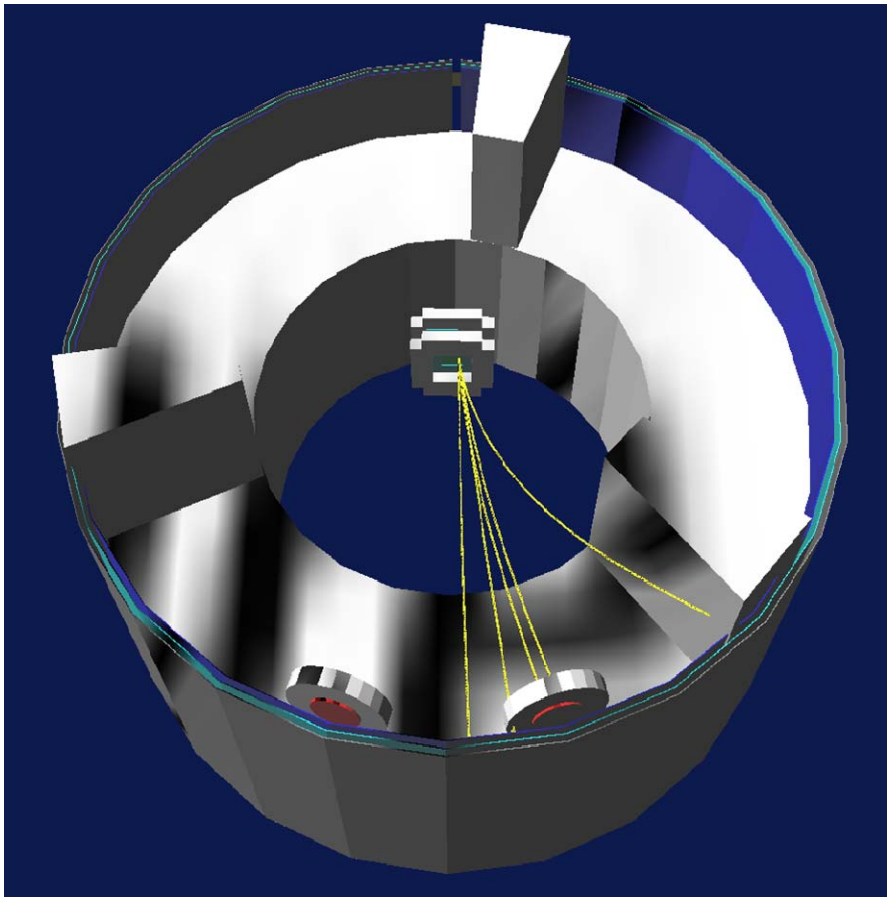

Figure C.1. Proton trajectories in a 0.8 T magnetic field. The detection geometry of the test at PSI is accounted for in these simulations.

Vita

Juan Pablo Urrego Blanco was born in 1979 in Simijaca, Colombia. After graduating from high school from the Liceo Nacional “José Joaquín Casas”, he attended the Universidad Nacional de Colombia in Bogotá. There he obtained a degree in Physics with a thesis on the use of energy ordered spectra to analyze properties of the nuclear continuum. After graduation he worked as a Physics instructor at several universities in Bogota, including Universidad Militar Nueva Granada. In 2002, after meeting Dr. A. Galindo’Uribarri he joined the University of Tennessee as a graduate student. There he had the opportunity to develop his research at the Paul Scherrer Intitute, in Switzerland and in the Holifield RadioactiveIon Beam Facilitiy at Oak Ridge National Laboratory, while complementing his education with courses taken at ETH and the University of Zurich. After graduation he will work in industry, in the field of oil exploration and production.